BACHELORARBEIT

Zum Erlangen des akademischen Grades Bachelor of Science

Density-Based Mixing Method for Hybrid Functionals in an All-Electron Framework

Eingereicht von: Jessica Richter

Gutachter/innen: Prof. Dr. Claudia Draxl
Prof. Dr. Silvana Botti

Eingereicht am Institut für Physik
der Humboldt-Universität zu Berlin im: September 2021

Reviewer:

Prof. Dr. Claudia Draxl
Solid-State Theory Group
Department of Physics and IRIS Adlershof
Humboldt Universität zu Berlin
Germany

Prof. Dr. Silvana Botti
Solid-State Theory Group
Institute of Condensed Matter Theory and Optics
Friedrich-Schiller-Universität Jena
Germany

Advisor:

Cecilia Vona
Solid-State Theory Group
Department of Physics
Humboldt Universität zu Berlin
Germany

Abstract

In this thesis, we investigate hybrid exchange-correlation functionals in the framework of density functional theory. Due to their high accuracy for band gap calculations, hybrid functionals are a common choice. Though, they lack precision for very large or very small gaps. To make hybrid functionals universally applicable, Marques *et al.* [1] suggested a density-based parametrization of the mixing in hybrid functionals. The so-called density-based mixing method relies only on the ground state electron density, and hence, can be implemented in DFT calculations without cumbersome calculations. Marques *et al.* constructed the method with the pseudo-potential code VASP. However, the gold standard of DFT are all-electron full-potential codes like **exciting**. Our research ascertains whether the density-based mixing method by Marques *et al.* can also be applied to an all-electron framework and how it needs to be adapted. The results show systematic discrepancies due to the conceptional differences in the codes. Therefore, also the best parametrization of the mixing parameter is different. We could optimize the density-based mixing method for **exciting** by varying the material set and the parametrization. The implementation of the adapted density-based mixing method in hybrid functionals leads to a noteworthy improvement of the band gap calculations. All DFT results performed for the thesis are accessible at [2].

Acknowledgements

I would like to gratefully acknowledge the supervision of Prof. Claudia Draxl and her advice during the bachelor's project. Moreover, I want to thank Prof. Silvana Botti and Pedro Borlido for providing the geometry of the crystalline systems and additional data, to which we could compare our results to. Furthermore, I would like to appreciate the help with the Wannier functions in **exciting** by Sebastian Tillack and thank Sven Lubeck for providing advanced species files for the materials we investigated. Finally, I would like to express my gratitude to Cecilia Vona, who implemented the calculation of the density-based quantity in **exciting** and supported me with steady guidance.

Contents

Appendix

List of Abbreviations

DFT	density functional theory
VASP	Vienna Ab initio Simulation Package
xc	exchange-correlation
HK	Hohenberg-Kohn
KS	Kohn-Sham
HF	Hartree-Fock
BZ	Brillouin zone
HEG	homogeneous electron gas
LDA	local density approximation
GGA	generalized gradient approximation
PBE	GGA functional developed by Perdew, Burke and Ernhof
PBE0	hybrid functional based on PBE
HSE06	hybrid functional developed by Heyd, Scuseria and Ernzhof
(L)APW	(linearized) augmented plane waves
lo	local orbitals
MT	muffin-tin sphere
IT	interstitial region
SCF	self-consistent field cycle
CBM	conduction band minimum
VBM	valence band maximum
MLWF	maximally localized Wannier functions
SOC	spin-orbit coupling
ZORA	zero-order regular approximation
RMSE	root-mean-squared error
PTE	periodic table of elements

List of Figures

List of Tables

1. Motivation

The most used method in physics for the *ab initio* description of solid-states is density functional theory (DFT). It provides a very accurate approach to obtain the physical properties of many-body systems such as lattice constants, phonon frequencies and elastic properties. In this thesis, we will concentrate on band gap calculations, i.e. the computation of the energy differences between the ground state and the lowest excited state of a solid. In particular, we aim at implementing a method using DFT to improve band gap calculations.

DFT allows the computation of solid-state properties with different levels of approximation, determined by the accuracy of the exchange-correlation (xc) functional. We will employ semi-local and hybrid xc functionals. Semi-local xc functionals estimates xc effects based on the local electron density and its generalized gradient. Therefore, they describe ground-state properties quite well. However, they highly underestimate band gaps, which is partly caused by incorrectly included self-interaction effects. This deficit can be cured in some extend by a linear combination of semi-local and many-body exact exchange in (so-called) hybrid functionals. With them, non-local effects are covered and reliable results for band gaps can be yield.

The amount of exact exchange included in hybrid functionals is determined by different parameters, which have a constant value in standard approaches. Several publications [1, 3, 4], however, suggest parametrizing the mixing of semi-local and non-local effects in order to capture the specifics of different materials. Thus, the amount of required exact exchange adapts inherently to the characteristics of the materials, and the accuracy of the results becomes less material dependent. Hence, the hybrid functionals evolve into universally applicable approaches. Marques *et al.* [1], in particular, advocate a parametrization of the mixing in hybrid functionals based on the ground-state electron density. To design the so-called density-based mixing method, Marques *et al.* computed ground state densities and band gaps of 21 materials. Their calculations were performed with the solid-state code VASP (Vienna Ab initio Simulation Package) [1], which uses a pseudo-potential and thus considers only the valence density [5]. The gold standard of DFT, however, are all-electron full-potential code calculations, which lead to the best numerical precision. In this thesis, we want to implement the method presented by Marques *et al.* to such a framework. As the underlying approaches are conceptually different, it is worth studying whether and to which extent the differences in the codes affect the density-based mixing method. In the case of significant discrepancies, a reformulation of the suggested parametrization would be necessary.

The thesis is structured as follows. In Chapter 2, we will introduce DFT, hybrid functionals, and the suggested method in detail. Chapter 3 provides a comprehensive look at the numerical parameters of the all-electron full-potential code **`exciting`** to explain how its parameters affect the calculations. Moreover, the quantities used for the density-based mixing methods are introduced. In the following discussion of the results (Chapter 4), we will focus on two aspects. First, a comparison between the results of the two codes codes, **`exciting`** and VASP, is given. Second, it is evaluated if an adjustment of the used material set and a variation of the parametrization can optimize the density-based mixing method.

2. Theory Background

As solids consist of many electrons and nuclei, many interactions need to be included when one wants to describe their properties from first principles. Whereas the standard Schrödinger approach treats solids as a many-body system and creates a highly complex problem to solve, DFT has the goal to provide an exact description of correlated many-body systems based on the particle density [6]. This change of perspective leads to an immense reduction of the degrees of freedom that need to be considered. The chapter starts with a short description of many-body problems (Chapter 2.1) to explain this advance. The focus, nevertheless, will lie on the theoretical foundation of DFT (Chapter 2.2) as well as the approach to describe interacting particles with the means of single-particle equations (Chapter 2.3).

A primary goal of DFT is to find a functional[i] of the ground state electron density that uniquely determines the ground state energy. The most intricate part is to describe the exchange and correlation effects between the electrons. Therefore, in Chapter 2.4 we will have a closer look at approximations that have been found for the xc functional, with a special emphasis on hybrid functionals (Chapter 2.5). Hybrid xc functionals perform well in terms of band gap reproduction for a majority of materials. Their accuracy, however, depends strongly on the material type. To make them equally applicable for all kinds of materials, one can make the parameters of hybrid functionals material dependent. In the last part of this chapter (Chapter 2.6), we will introduce one possible parametrization – the density-based mixing method, which adjusts the parameters of hybrid functionals based on the electron density. For the derivations in Chapter 2, we follow closely references [6] and [7], and use Hartree atomic units, for all the equations, i.e. $\hbar = e = a_0 = m_e = 1$.

2.1 Solids

Solids can be seen as a collection of atoms consisting of periodically arranged nuclei and the electrons distributed around them. In order to investigate their energy states and how they change for different arrangements, we have to treat the system quantum mechanically.The periodicity allows to divide solids a large but finite number of unit cells. Hence, we are treating them by explicitly investigating one unit cell under the application of periodic boundary conditions [8].

Born-Oppenheimer approximation. Since the electrons are much lighter than the atomic nuclei, they respond more rapidly to changes in their surrounding. Hence, we can separate the total energy calculation for the nuclei and electrons of a solid. This approach is called the Born-Oppenheimer approximation. It splits the physical question into two parts: i) at fixed positions of the nuclei, we determine the electron interaction and motion, and ii) for a given

[i]The term functional describes a function, which argument is a function itself. This characteristic is often indicated through brackets instead of parenthesis. In the specific case of the total energy functional, DFT wants to define, E depends on the electron density n, which is a function itself of the electron position $\mathbf{r}$: $E[n(\mathbf{r})]$.

nuclei dependence of the electrons, we find the lowest energy configuration [7]. Consequently, the ground state energy E_0, which is the lowest energy configuration of the system, becomes an eigenvalue of the (time-independent, non-relativistic) Schrödinger equation

$$H_{\mathbf{k}}\Psi_{n\mathbf{k}} = E_{n\mathbf{k}}\Psi_{n\mathbf{k}}. \tag{2.1}$$

The wave function $\Psi_{n\mathbf{k}}$, where n labels the state in which the collection of particles is, depends only on the electronic degrees of freedom $\Psi_{n\mathbf{k}} = \Psi_{n\mathbf{k}}(\mathbf{r}_1, \mathbf{r}_2, ..., \mathbf{r}_N)$. Due to the periodicity of the solid, also the Schrödiger equation leads to periodic solutions, which are characterized by the wave vector $\mathbf{k}$. Moreover, $H_{\mathbf{k}}$ labels the Hamiltonian and has the following form

$$H_{\mathbf{k}} = H_{\text{kin}} + H_{\text{ne}} + H_{\text{ee}}. \tag{2.2}$$

Here H_{kin} is the kinetic energy of all electrons, H_{ne} describes the nucleus-electron interaction, i.e. the influence the external potential $V_{\text{ext}}(\mathbf{r})$, which is generated by all atomic nuclei, has on the electrons, and H_{ee} is the term for the electron-electron interaction. By explicitly writing all the terms, the Hamiltonian is given by

$$H_{\mathbf{k}} = -\frac{1}{2}\sum_{i}^{\text{occ.}} \nabla_{i\mathbf{k}}^2 + \sum_{i}^{\text{occ.}} V_{\text{ext}}(\mathbf{r}_{i\mathbf{k}}) + \sum_{i}^{\text{occ.}} \sum_{j<i} \frac{1}{|\mathbf{r}_{i\mathbf{k}} - \mathbf{r}_{j\mathbf{k}}|}. \tag{2.3}$$

The sum is over all occupied states i in a solid, leading to N electrons that need to be considered. Because the electron-electron interaction term includes pairs of electrons i and j, the Schrödinger equation is not separable into single-particle equations and stays a many-body problem. This dependence makes computing the ground state energy with means of the Schrödinger equation very difficult.

Many-body wave function. The many-body wave function $\Psi_{n\mathbf{k}}$ can be expressed in terms of the single electron wave functions $\psi_{i\mathbf{k}}$. The simplest construction is a product of all single-particle wave functions

$$\Psi_{n\mathbf{k}}(\mathbf{r}_1, ..., \mathbf{r}_N) = \psi_{1\mathbf{k}}(\mathbf{r}_1) \cdot ... \cdot \psi_{N\mathbf{k}}(\mathbf{r}_N), \tag{2.4}$$

which is called Hartree product [7]. It can sufficiently be used for non-interacting particles, for which the energy eigenvalue becomes a sum of the single-particle energies.

However, the Hartree product does not satisfy the anti-symmetric principle of fermions [7]. This is considered by the Slater determinant, which combines the one-electron wave functions in an anti-symmetric way through a determinant [7] as

$$\Psi_{n\mathbf{k}}(\mathbf{r}_1, ..., \mathbf{r}_N) = \frac{1}{\sqrt{N!}} \det \begin{bmatrix} \psi_{1\mathbf{k}}(\mathbf{r}_1) & \psi_{1\mathbf{k}}(\mathbf{r}_2) & \dots & \psi_{1\mathbf{k}}(\mathbf{r}_N) \\ \psi_{2\mathbf{k}}(\mathbf{r}_1) & \psi_{2\mathbf{k}}(\mathbf{r}_2) & \dots & \psi_{2\mathbf{k}}(\mathbf{r}_N) \\ \vdots & \vdots & \ddots & \vdots \\ \psi_{N\mathbf{k}}(\mathbf{r}_1) & \psi_{N\mathbf{k}}(\mathbf{r}_2) & \dots & \psi_{N\mathbf{k}}(\mathbf{r}_N) \end{bmatrix}. \tag{2.5}$$

This notation meets the Pauli-principle, and thus, shows the characteristics of shell structure [9].

Electron density. Alternatively, one can focus on the electron density $n(\mathbf{r})$, which describes the probability to find an electron at a particular coordinate $\mathbf{r}$ with $N-1$ other electrons distributed in space [10]

$$n(\mathbf{r}) = N \int \mathrm{d}^3 r_2 ... \int \mathrm{d}^3 r_N \, \Psi^*(\mathbf{r}, \mathbf{r}_2, ..., \mathbf{r}_N)\Psi(\mathbf{r}, \mathbf{r}_2, ..., \mathbf{r}_N). \tag{2.6}$$

Using the electron density instead of the many-body wave function results in an obvious reduction of the number of coordinates [7]. Whereas for $\Psi(\mathbf{r}_1, ..., \mathbf{r}_N)$, $3N$ coordinates have to be considered, for $n(\mathbf{r})$ only three are necessary, which makes the computation more feasible. For the separation into single-particle wave functions, n simplifies to [11]

$$n(\mathbf{r}) = 2\sum_{i}^{\text{occ.}} |\psi_{i\mathbf{k}}(\mathbf{r})|^2, \tag{2.7}$$

where the 2 captures the two possible spin configurations of the electrons.

In an experiment, the wavefunctions of the electrons cannot be measured. Instead, just the probability distribution is observable. Therefore, all properties of a solid need to be describable by the electron density [7]. Based on this understanding, the concept of DFT arose – to describe a many-body system purely throughout the particle density.

2.2 Hohenberg-Kohn Theorems

The mathematical basis for DFT is built upon two theorems, which were initially formulated and proven by Hohenberg and Kohn (HK) [12]. Their goal was to develop an exact theory of many-body systems as general as possible [6].

> **First Theorem:** For any system of interacting particles in an external potential $V_{\text{ext}}(\mathbf{r}_i)$, the potential is determined uniquely, except for a constant, by the ground state particle density $n_0(\mathbf{r})$. *Adapted from reference [6]*

In solids, the external potential V_{ext} is composed by the atomic nuclei and the electron distribution n is directly affected by it, since the electrons and nuclei interact electromagnetically. The first HK theorem states that the there is a unique one-to-one mapping between the potential and the density. In other words, there is only one functional leading to a certain electron distribution, and hence, the opposite relation is true as well. So, in theory, the external potential could be directly determined by the lowest energy configuration of the electrons n_0. This argumentation clarifies the second step of the total energy computation mentioned above. Through this relationship between the external potential on the ground state density, the Hamiltonian (2.3) becomes fully determined [6]. Thus, in principle, the Schrödinger equation can be fully solved, and all ground state properties can be assigned based on the knowledge of the ground state density. This line of reasoning for DFT calculations is shown in figure 2.1.

> **Second Theorem:** A universal functional for the total energy $E[n]$ in terms of the density $n(\mathbf{r})$ can be defined, valid for any external potential $V_{\text{ext}}(\mathbf{r}_i)$. For any particular $V_{\text{ext}}(\mathbf{r}_i)$, the exact ground state energy of the system is the global minimum of this functional, and the density $n(\mathbf{r})$ that minimizes the functional is the exact ground state density $n_0(\mathbf{r})$. *Adapted from reference [6]*

This second theorem states that an energy functional $E[n]$ exists that determines the exact ground state total energy and ground state density [6]. One does not need to solve the Schrödinger equation to get the total energy eigenvalues. Based on the interactions that are present in a solid-state system (compare eq. 2.2), one can separate the total energy in several parts and suggest an energy functional of the following form [6]

$$E_{\text{HK}}[n] = T[n] + \int \mathrm{d}^3 r \, V_{\text{ext}}(\mathbf{r}) n(\mathbf{r}) + E_{\text{int}}[n]. \tag{2.8}$$

The functional includes the kinetic energy of the interacting particles T, the influence of the external potential V_{ext}, and the internal energy E_{int}, which describes the full interactions of the electrons with each other [6]. However, it stays unclear how these parts can be formulated as explicit functionals of the electron density since the influence the electrons have, e.g. on each others kinetic energies, is hard to separate [6]. Nevertheless, the HK theorems provide a meaningful foundation for an exact theory of many-body interaction as they assign a direct relation between the ground state electron density and all physical properties of the system [ii].

[ii] The HK theorems can be extended to be applicable for finite temperatures (which was developed by Mermin [13]) or generalized to time-dependent problems (provided by Runge and Gross [14]). With these extensions, not only the ground state energy but also properties like the entropy or specific heat become functionals of the equilibrium electron density [6]. For finite temperatures, however, finding the suitable energy functional is even more complex than for ground state calculations since excited states need to be included.

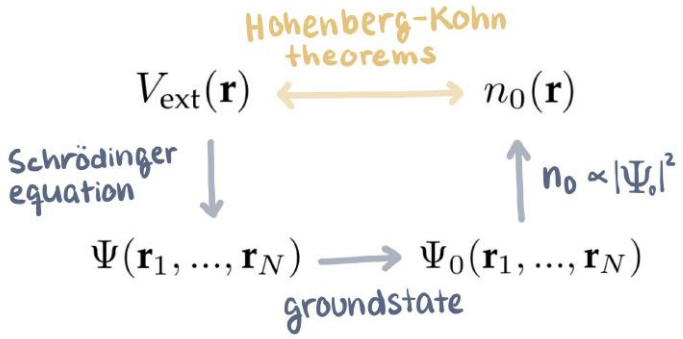

Figure 2.1: Schematic representation of the HK theorems. With the Schrödinger equation, one can derive the many-body wave functions Ψ once the external potential V_{ext} of the system is known. Based on that, the computation of the ground state wave function Ψ_0 and ground state density n_0 (2.7) is possible. The HK theorems connect this to the first step by adding the conceptual relation between the external potential and the ground state electron density. Therefore, the cycle is closed, which gives a clear line of argumentation for iterative calculations. The sketch was created based on reference [6, fig. 6.1].

2.3 Kohn-Sham Ansatz

For an arbitrary many-body system, it can become rather unfeasible to find an analytical formulation of the energy functional, although the HK theorems prove its existence. The only case where the exact solution for the energy functional is found is a system of N non-interacting particles without an external potential [7]. This example is known as the homogeneous electron gas (HEG). For the HEG, the energy HK functional (2.8) is nothing other than the kinetic energy [6]. Moreover, the electron density becomes constant $n(\mathbf{r}) = \text{const.}$, i.e. the probability is distributed homogeneously in space [7]. This particular case can be used for local approximations (which we will discuss later in chapter 2.4) and helps to find the solution for more complex systems. In order to give a prescription on how to construct a general energy functional, Kohn and Sham (KS) [11] suggest creating an auxiliary system based on the non-interacting particles of an HEG and add an interacting electron density.

Kohn-Sham auxiliary system. The KS ansatz assumes that for every system of interacting particles, there can be found an arrangement of non-interacting particles with the same ground state electron density n_0 [iii]. Since the electron density is the same, the systems can be exchanged, but the physical properties can still be reproduced exactly [6]. This change of perspective is illustrated in figure 2.2.

This approach provides a better manageable suggestion for the energy functional than the HK functional (2.8). Instead of considering the interaction between each pair of electrons, just the influence of the whole electron distribution on one electron is considered. Rather than calculating all electrons at once, the system is reduced to several one-particle problems. Therefore, one can also understand the KS approach as the task to rewrite equation (2.8) into an energy functional where all parts are explicitly modelled as functionals of the density [6]

$$E_{\text{KS}}[n] = T_{\text{s}}[n] + \int \mathrm{d}^3 r \, V_{\text{ext}}(\mathbf{r}) n(\mathbf{r}) + E_{\text{Hartree}}[n] + E_{\text{xc}}[n]. \tag{2.9}$$

The first advantage of the auxiliary ansatz is the kinetic energy of independent particles T_{s}, which can be written down explicitly in terms of the indepentend particle wave functions

[iii] In principle, different wave functions can construct the same electron density $n(\mathbf{r})$. However, there is no general proof that for every interacting electron system, a non-interacting particle system with the same electron density can be found. For simple cases like the HEG and one- or two-electron problems, it can be shown directly. Also, for more complex systems, the results are good enough to validate the assumption [6].

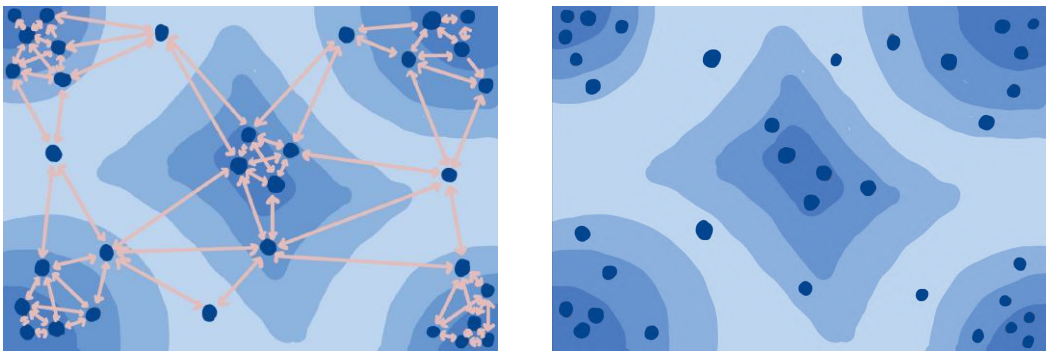

(a) System of interacting particles. **(b)** System of independent particles.

Figure 2.2: Schematic representation of the KS approach: (a) The electrons (blue dots) are interacting with each other (as shown by the pink arrows). Their wave functions build the electron density $n_0(\mathbf{r})$ (blue areas in the background – the darker they are, the more likely for the electron to be there). (b) A non-interacting particle system generates the same ground state density $n_0(\mathbf{r})$ based on independent particle wave functions. The KS ansatz aims at describing the system in (a) with means of the system in (b).

(which are implicitly functionals of n). T_s is simply the sum of all single-particle kinetic energies

$$T_\mathrm{s} = -\sum_i^{\text{occ.}} \langle \psi_{i\mathbf{k}} | \nabla^2 | \psi_{i\mathbf{k}} \rangle = -\sum_i^{\text{occ.}} \int \mathrm{d}^3 r \, |\nabla \psi_{i\mathbf{k}}(\mathbf{r})|^2. \tag{2.10}$$

Other than that, the influence of the external potential V_ext is considered here as in the previous HK functional (2.8) since in this term n is written explicitly already. Moreover, the Coulomb interaction between a single electron and the electron density, as one part of the electron-electron interaction (E_int of eq. 2.8), becomes an explicit functional of n. It is called Hartree energy and can be expressed as

$$E_\mathrm{Hartree}[n] = \frac{1}{2} \iint \mathrm{d}^3 r \, \mathrm{d}^3 r' \, \frac{n(\mathbf{r}) n(\mathbf{r'})}{|\mathbf{r} - \mathbf{r'}|}. \tag{2.11}$$

All additional parts of the interaction that are not covered by the indepentent particle kinetic energy and the Hartree energy are considered by the xc functional E_xc. It describes the difference between the true interacting particle many-body system and the auxiliary independent-particle system, where the kinetic energy is replaced by the independent-particle kinetic energy and the internal energy is replaced by the Hartree energy. Hence, the xc functional can be written as [6]

$$E_\mathrm{xc}[n] = \left\langle \hat{T} \right\rangle - T_s[n] + \left\langle \hat{V}_\mathrm{int} \right\rangle - E_\mathrm{Hartree}[n]. \tag{2.12}$$

Its exact form is not known so far, but several approximations have been found, which we will further discuss in Chapter 2.4.

Kohn-Sham equations. The only physical restriction for the electron density $n(\mathbf{r})$ is the number of particles, which needs to be preserved [6]

$$\int \mathrm{d}^3 r \, n(\mathbf{r}) = N. \tag{2.13}$$

With this constraint, one uses Lagrange multipliers to minimize the KS functional E_KS (2.9) with respect to the wave function. As stated in the second HK theorem, this minimization leads to the ground state electron density. Similarly to the derivation of the Schrödinger equation, one extracts the so-called KS equations [6]

$$H_\mathrm{KS} \psi_{i\mathbf{k}} = \varepsilon_{i\mathbf{k}} \psi_{i\mathbf{k}}. \tag{2.14}$$

The important difference is that one finds N one-particle equations instead of one equation with $3N$ dimensions (since $3N$ degrees of freedom are included in the total wave function Ψ). The KS Hamiltonian H_{KS} can be written explicitly as

$$H_{\text{KS}} = -\frac{1}{2}\nabla^2 + V_{\text{KS}}[n(\mathbf{r})], \tag{2.15}$$

where V_{KS} is the KS potential [6]

$$V_{\text{KS}}[n(\mathbf{r})] = V_{\text{ext}}(\mathbf{r}) + V_{\text{Hartree}}[n(\mathbf{r})] + V_{\text{xc}}[n(\mathbf{r})]. \tag{2.16}$$

Here, V_{ext} is the external potential introduced above and V_{Hartree} the Hartree potential. The latter describes the Coulomb repulsion between the considered electron and the total electron density [7] and reads as

$$V_{\text{Hartree}}[n(\mathbf{r})] = \int \mathrm{d}^3 r' \, \frac{n(\mathbf{r})}{|\mathbf{r} - \mathbf{r'}|}. \tag{2.17}$$

The xc potential V_{xc} is defined as the functional derivative of the xc energy E_{xc} [6]

$$V_{\text{xc}}[n(\mathbf{r})] = \frac{\delta E_{\text{xc}}[n(\mathbf{r})]}{\delta n(\mathbf{r})}. \tag{2.18}$$

Since V_{KS} is an explicit functional of the electron density, the Hamiltonian becomes a functional of the electron density as well. Therefore, to solve the KS equations, i.e. to compute the wave functions, the knowledge of the electron density n is needed. However, n can only be computed based on the electron wave functions (see eq. 2.7). Hence, the solution has to be found iteratively. Starting from a trial electron density or an appropriate starting point for the KS potential, the wave functions are computed. Thus, the electron density can be derived, and again, a new potential is gained as [7]

$$V_{\text{KS}}^{\text{old}} \longrightarrow \psi_{\text{i}} \longrightarrow n \longrightarrow V_{\text{KS}}^{\text{new}}.$$

This self-consistent solution is the logic algorithm used to solve DFT problems. How is is numerically implemented in **`exciting`** is further explained in Chapter 3.1.2.

Generalized Kohn-Sham approach. In principle, also other auxiliary systems than the non-interacting particles could be used, e.g. certain interactions could be included. By choosing non-interacting particles, it is defined that only the correct ground state density and energy are reproduced [6]. However, excited states, and in particular band gaps, cannot be determined accurately with the standard KS approach. For excited states, the minimization of the energy functional (which leads to the KS equations) no longer gives the correct total energy as excitations are associated with saddle points at higher energies [6]. Moreover, the energy eigenvalues ε_i of the KS equations (2.14) do not resemble the atomization energies with which the electrons are bound in the many-body systems [6]. Therefore, to reproduce band gaps correctly, the so-called generalized KS approach is typically used.

The generalized KS approach includes a non-local potential [15]. It is based on the orbital-dependent many-body theory developed by Hartree and Fock (HF). HF theory considers the interaction of a single electron with a mean-field created by the other electrons. This approach makes it possible to describe the exchange interaction exactly, in form of the so-called HF potential [15]

$$V_{\text{x}}^{\text{HF}}(\mathbf{r}, \mathbf{r'}) = -\sum_{i}^{\text{occ}} \sum_{\mathbf{q}}^{\text{BZ}} \frac{\psi_{i\mathbf{q}}(\mathbf{r}) \psi_{i\mathbf{q}}^*(\mathbf{r'})}{|\mathbf{r} - \mathbf{r'}|}. \tag{2.19}$$

The summation of the reciprocal vectors $\mathbf{q}$ should be understood as a discrete integration over the Brillouin zone (BZ). Note that, in the generalized KS approach, the HF exchange functional is evaluated with KS orbitals, not Slater determinants as in the original HF theory. Therefore,

in the framework of generalized KS, this term is often referred to as non-local exact exchange instead of as HF functional. With it, the KS equation (2.14) needs to be adjusted to [15]

$$H_{\mathrm{KS}}(\mathbf{r})\psi_{i\mathbf{k}}(\mathbf{r}) + \alpha \int \mathrm{d}^3 r'\, V_{\mathrm{x}}^{\mathrm{HF}}(\mathbf{r}, \mathbf{r'})\psi_{i\mathbf{k}}(\mathbf{r'}) = \varepsilon_{i\mathbf{k}}\psi_{i\mathbf{k}}(\mathbf{r}). \tag{2.20}$$

The inclusion of the non-local exact exchange is also needed for hybrid xc functionals[iv]. Consequently, the generalized KS equation is solved for hybrid functionals (see Chaper 2.5).

2.4 Exchange-Correlation Functionals

The exact form of the xc functional E_{xc} is not known, but several approximations for it have been found. As it is the only term, which cannot be described explicitly, the accuracy of the ground state density is only limited by the approximations made for the xc functions [6].

Perdew and Schmidt [16] introduced the term "Jacob's ladder [v] of density functional approximations for the exchange-correlation energy", where each rung of the ladder represents an increase of accuracy. The ladder is illustrated in figure 2.3. The metaphorical 'heaven' above the highest rung symbolizes an exact formulation of all exchange and correlation effects. The ladder starts with a local approximation of the electron density n and continues by including the gradient of n and higher-order derivatives of n. Moreover, hybrid functionals and non-local approximations are listed to give the most accurate results. The latter include orbital dependent formulations to satisfy non-local effects. Hybrid functionals combine the two worlds as they mix (semi-)local and non-local approximations. Since hybrid functionals are the focus of our work, we will discuss them separately in Chapter 2.5.

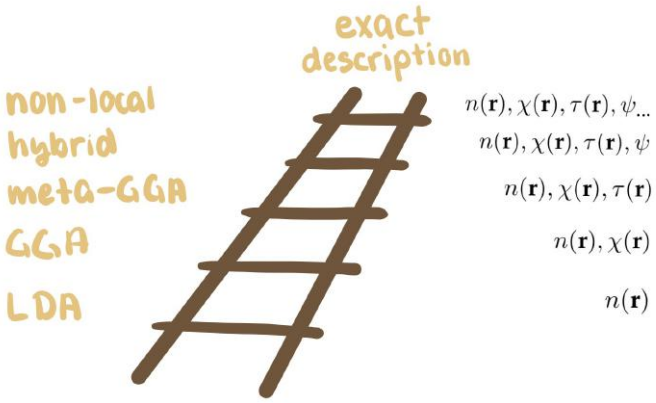

Figure 2.3: Jacob's ladder of DFT symbolises the hierarchy in which all xc functionals can be ranked. Each rung represents an increase of accuracy. Starting with the local density approximation (LDA), one improves the functionals in the generalized gradient approximations (GGA) and meta-GGA. Further approximations are hybrid and non-local functionals. On the right the properties included in the approximations are listed: the electron density $n(\mathbf{r})$ (2.7), the reduced density gradient $\chi(\mathbf{r})$ (2.22), the kinetic energy density $\tau(\mathbf{r})$ (2.23) as well as occupied and unoccupied electron states ψ.

The formulation of E_{xc} in equation (2.12) does not necessarily help to find an analytical expression. Instead, it gives an understanding of the interactions that are included. Most importantly,

[iv] The α already included in the generalized KS is the mixing parameter which defines the fraction of HF exchange that is included via the hybrid functionals.

[v] The term is based on a biblical reference of a ladder from earth to heaven in Jacobs dream. Here, it describes the desire to find the most accurate approximation, a way to quantum chemical heaven.

it becomes apparent that the long-term influences (namely kinetic energy and Coulomb interaction) are explicitly subtracted [6]. Therefore, a local approximation is a reasonable first step.

Local density approximation. As mentioned above, the HEG is the simplest case of many-body systems. Therefore, it is easier to construct the xc potential for it. The results of the HEG build the basis for the local density approximation (LDA), in which we take the same potential but apply it to the actual electron density of the investigated system [7]

$$V_{\mathrm{xc}}^{\mathrm{LDA}}\left[n(\mathbf{r})\right] = V_{\mathrm{xc}}^{\mathrm{HEG}}\left[n(\mathbf{r})\right]. \tag{2.21}$$

The underlying assumption is that the effects of exchange and correlation depend only on the local magnitude of the electron density. Indeed, they are generally found to have a local character and a rather short range [6]. Consequently, the LDA achieves its best results for systems that are very similar to the HEG. For example, for nearly-free-electron metals, LDA reaches high accuracy. Also, for many solids, the (valence) electrons are free enough to be sufficiently approximated as a HEG [6].

Generalized gradient approximation. The LDA can be extended by including the magnitude of the electron density gradient $|\nabla n|$. Referring to the combination of the local magnitude of n and the local change of n, this is called a semi-local approximation.

A simple expansion of the electron density by its gradient, however, often leads to complications and even worse results than the LDA [6]. Due to large magnitudes of the gradient in real materials, the expansion often breaks down and is not able to satisfy relevant physical conditions [6]. Hence, different methods have been found to modify the behaviour of large gradients in a way that the desired properties are preserved. These methods are summarised as generalized gradient approximations (GGAs).

The most common GGA functionals were developed by Becke (B88) [17], Perdew and Wang (PW91) [18] and Perdew, Burke and Enzhof (PBE) [19]. PBE is used in our calculations. These functionals were developed with a focus on different physical properties. Whereas B88 was chosen to give the correct exchange energy density ϵ_{x} and PW91 satisfies the non-uniform scaling conditions to be accurate for thin layers, PBE was constructed to simplify the parameters of the functional [6]. They all manage to reproduce a specific aspect better than the others. Therefore, it depends on the application which functional achieves the best accuracy. So, no clear hierarchy of GGA functionals can be defined. In all of them, the exchange part is expressed in terms of the dimensionless reduced density gradient[vi] [6]

$$\chi(\mathbf{r}) = \frac{|\nabla n(\mathbf{r})|}{2k_F n(\mathbf{r})} \tag{2.22}$$

In comparison to the LDA, all the GGAs lead to lower exchange energies, which corrects the LDA overbinding [6]. Moreover, the GGAs give better results for the total energies, atomization energies, energy barriers, and structural energy differences [19].

Beyond LDA and GGA. The next step on Jacob's ladder after GGAs are meta-GGAs (see figure 2.3), which include, in addition to the local electron density $n(\mathbf{r})$ and its generalised gradient $\chi(\mathbf{r})$, also the kinetic energy density [20]

$$\tau(\mathbf{r}) = \sum_{i}^{\mathrm{occ.}} \frac{1}{2}|\nabla\psi_{i\mathbf{k}}(\mathbf{r})|^2 = \sum_{i}^{\mathrm{occ.}} \psi_{i\mathbf{k}}^{*}(\mathbf{r})\nabla^2\psi_{i\mathbf{k}}(\mathbf{r}). \tag{2.23}$$

τ is an explicit functional of the occupied orbitals and includes second derivatives of them.

[vi] This generalized gradient is also later used to determine the density-based quantity $\bar{g}$ on which the density-based mixing method is based.

The following rungs include hybrid functionals (which we will introduce in Chapter 2.5) and non-local approximations. Moreover, methods to optimize the potential (so-called optimized effective potential OEP), such that the total energy of the systems remains stationary for small variations [6], are developed as an ansatz for orbital-dependent functionals.

In general, no systematic way has been found to improve the xc functionals [6]. It is not enough to use higher powers of the local electron density to advance the functionals further. Hence, there is no clear path towards the exact description of solid states and developing it is part of current research.

2.5 Hybrid Functionals

Hybrid functionals combine the computational feasibility of (semi-)local functionals and the accuracy of non-local approximations. They are made by a fraction α of non-local (NL) exchange and (semi-)local (L) xc energy, such that the correlation part stays purely (semi-)local,

$$E_{\mathrm{xc}}^{\mathrm{hyb}} = \alpha E_{\mathrm{x}}^{\mathrm{NL}} + (1-\alpha) E_{\mathrm{x}}^{\mathrm{L}} + E_{\mathrm{c}}^{\mathrm{L}}. \tag{2.24}$$

This fraction α is called the mixing parameter. For the non-local exchange energy, HF theory is often used, which was introduced for the generalized KS approach in Chapter 2.3. In its framework, the electron correlation is neglected, which causes pure HF calculations to overestimate band gaps of solids (see, e.g., the HF + $\mathrm{PBE_c}$ band gap results in reference [1]). However, HF theory provides an explicit description of the exchange energy [15]

$$E_{\mathrm{x}}^{\mathrm{HF}} = -\frac{1}{2} \sum_{i,j}^{\mathrm{occ.}} \sum_{\mathbf{k},\mathbf{q}}^{\mathrm{BZ}} \iint \mathrm{d}^3 r \, \mathrm{d}^3 r' \, \frac{\psi_{i\mathbf{k}}^*(\mathbf{r}) \psi_{j\mathbf{q}}(\mathbf{r'}) \psi_{j\mathbf{q}}^*(\mathbf{r}) \psi_{i\mathbf{k}}(\mathbf{r'})}{|\mathbf{r} - \mathbf{r'}|}, \tag{2.25}$$

which is why it is used for hybrid functionals. This orbital-dependent formulation of the HF functional $E_{\mathrm{x}}^{\mathrm{HF}}$ has the advantage to show discontinuities at electron densities corresponding to filled shells [6]. Hence, it is well suited for excitation energies, and band gaps [6]. Consequently, hybrid functionals with HF exchange provide better accuracy than LDA or GGA functionals in terms of band gap calculations. The advance follows a clear intuition: the pure exchange potential of HF overestimates the band gap, and (semi-)local calculations underestimate it [1]. Hence, the linear mixing improves the results. Based on that, many types of hybrid functionals have been developed over the years. In solid-state physics, the most used are PBE0 and HSE06, which are also employed in this work.

PBE0. The PBE0 functional uses the PBE functional (discussed in Chapter 2.4) for the semi-local xc energy. The hybrid functional is based on research by the same authors Perdew, Burke, and Ernzerhof [21], but was formulated in its current form by Adamo and Barone [22]. For the non-local exchange, the HF energy (2.25) is used, which results in

$$E_{\mathrm{xc}}^{\mathrm{PBE0}} = \alpha E_{\mathrm{x}}^{\mathrm{HF}} + (1-\alpha) \, E_{\mathrm{x}}^{\mathrm{PBE}} + E_{\mathrm{c}}^{\mathrm{PBE}}. \tag{2.26}$$

With a mixing parameter of $\alpha = 0$, this would become a pure PBE functional and with $\alpha = 1$, the exchange would be fully non-local. However, the full non-local exact exchange would have to be combined with a non-local correlation functional to reproduce the physics correctly [9]. The latter, however, has not been fully developed yet. Therefore, α should be smaller than one. In the PBE0 functional, the mixing parameter is defined to have the value $\alpha = 0.25$ [21]. PBE0 does not consist of any empirical parameter, and therefore, is an *ab initio* functional [15].

HSE06. The HSE06 hybrid functional was developed by Heyd, Scuseria, and Ernzhof [23, 24]. It uses, similarly to PBE0, PBE as the semi-local foundation and HF as the non-local exchange. Additionally, HSE06 takes the screening of electron-electron interaction into account. This

means it considers the fact that the Coulomb interaction between the electrons does not have an infinite range, which is important to notice in periodic systems such as solids. Therefore, it includes the HF exchange only within a short range (SR) and leaves the long-range (LR) interaction semi-local

$$E_{\mathrm{xc}}^{\mathrm{HSE06}} = \alpha E_{\mathrm{x}}^{\mathrm{HF_{SR}}}(\omega) + (1-\alpha)\, E_{\mathrm{x}}^{\mathrm{PBE_{SR}}}(\omega) + E_{\mathrm{x}}^{\mathrm{PBE_{LR}}}(\omega) + E_{\mathrm{c}}^{\mathrm{PBE}} \,. \tag{2.27}$$

The mixing parameter α is set to 0.25, too. The screening parameter ω defines the separation of space into short- and long-range by constructing

$$\frac{1}{r} = \underbrace{\frac{1-\mathrm{erf}(\omega r)}{r}}_{\mathrm{SR}} + \underbrace{\frac{\mathrm{erf}(\omega r)}{r}}_{\mathrm{LR}} \,. \tag{2.28}$$

This uses the error function erf for analytical reasons [23]. For $\omega = 0$ the long-range term becomes zero and the energy functional considers the complete non-local exchange (i.e. becomes equal to the PBE0 functional). Oppositely, for $\omega = \infty$ no short range is considered, no HF term is included, and therefore, PBE is recovered [23]. In HSE06, the screening parameter is set to $\omega = 0.11\ a_0^{-1}$ [24].

2.6 Parametrization of the Mixing Parameter

The standard hybrid functionals, PBE0 and HSE06 with constant parameters, as introduced above, lead to good results in band gap calculations. However, the accuracy of their performance differs for different materials. For very large or very small band gaps [1], PBE0 and HSE06 typically give worse results than for medium-sized band gap materials. This suggests that the parameters of the functionals should not be universal but rather be material-dependent in order to make the results equally good for all band gap sizes[vii]. In this thesis, we will concentrate on the parametrization of the mixing parameter α and continue with a constant screening parameter $\omega = 0.11\ a_0^{-1}$ [24].

It has been suggested that the mixing parameter is connected to the inverse of the static dielectric constant $\epsilon_\infty \propto 1/\alpha$, which is derived from the perspective of the self-energy Σ [1]. However, a parametrization based on ϵ_∞ is not practical, as the computation of the dielectric constant is very cumbersome [1]. This is why Marques *et al.* propose an alternative approach, that does not require calculations in addition to the ground state computation.

Density-based mixing method. The work by Marques and coworkers [1] suggests a mixing parameter based on the ground state electron density of the material. They searched for an estimator of the "local gap" in terms of the quotient $|\nabla n(\mathbf{r})|/n(\mathbf{r})$ [1]. This term is similar to the reduced gradient used in GGA and meta-GGA functionals (see Chapter 2.4). Testing different quantities related to the reduced gradient, they found the square root of the quotient $\sqrt{\frac{|\nabla n(\mathbf{r})|}{n(\mathbf{r})}}$ to work best [1]. The density-based quantity to parametrize α then is the average over one unit cell of the local gap estimator [1]

$$\bar{g} = \frac{1}{V_{\mathrm{cell}}} \int_{\mathrm{cell}} \mathrm{d}^3 r \sqrt{\frac{|\nabla n(\mathbf{r})|}{n(\mathbf{r})}} \,. \tag{2.29}$$

Similar research proposes variations of this parameter. For example, Koller *et al.* [3] use the local band gap estimator without the square root to parametrize the mixing parameter. However, they do not find a satisfying relationship between their $\bar{g}$ and α. Alternatively, Aull [4] tested

[vii] On the other hand, non-universal parameters which are determined empirically contradict the *ab initio* approach of DFT. So whether the parametrization of the mixing parameter is an advancement of the hybrid functional or not should be decided by the reader.

several modifications, finding a power of two instead of the square root to be the best adaption of $\bar{g}$. For this thesis, however, we stay with the parameter given in equation (2.29), leaving variations of $\bar{g}$ to further analysis.

Based on that quantity, Marques *et al.* propose a parametrization of the mixing parameter α as a single polynomial function

$$\alpha_{\text{mix}} = \mathrm{a} \cdot \bar{g}^n + \mathrm{b}, \tag{2.30}$$

which we will refer to as the density-based mixing method in the following. The specific values for a and b are found with the means of a regression between an optimal mixing parameter α_{opt} and the quantity $\bar{g}$ for a specified material set. Thereby, α_{opt} is the fraction of non-local exact exchange within a hybrid functional that reproduces the experimental gap of a material [1]. Both quantities, α_{opt} and $\bar{g}$, will be further analysed and discussed in Chapter 3.3.

In addition to the advantage that $\bar{g}$ depends only on ground state properties, Marques *et al.*, furthermore, found that its magnitude is invariant under the choice of xc functional for the density calculation. This means the parameter can be calculated with a (semi-)local functional, which is computationally cheap to compute. However, the application of the method is limited to bulk materials and fails for finite systems, slabs, interfaces, supercells with defects and similar cases [1]. This boundary can be overcome by a local form of the quantity $\bar{g}$, which is discussed in reference [25]. Since the thesis will focus on crystalline solids, this local form will not be taken into account in this work.

Results in the pseudo-potential framework. Marques *et al.* designed the density-based mixing method with pseudo-potential code VASP, i.e. calculated the parameters for the regression with this code. For the hybrid functionals PBE0 and HSE06, they propose a linear dependence ($n = 1$) between the mixing parameter and the quantity $\bar{g}$ for PBE0_{mix} and a power of four ($n = 4$) for $\text{HSE06}_{\text{mix}}$ [1]. They argue that the higher power for $\text{HSE06}_{\text{mix}}$ is needed, as the screening is already included in the potential itself, weakening the influence of the HF exchange, and therefore, making the relation between the mixing parameter and the screening more complex [1]. For these functions, they find the relations

$$\begin{aligned} \alpha_{\text{PBE0}} &= 1.10507\ a_0^{-1/2} \cdot \bar{g} - 1.00778 \quad \text{and} \\ \alpha_{\text{HSE06}} &= 0.130711\ a_0^{-2} \cdot \bar{g}^4 + 0.121983\,. \end{aligned} \tag{2.31}$$

In the following chapter, we will investigate whether similar fit parameters are found for the all-electron framework or fundamental changes have to made to adapt the method.

The improvement of band gaps with these fits is noteworthy. With the mixing method for PBE0, the gaps can be calculated with an average error of 14% instead of 30% and for HSE06 with 10% instead of 17% [1] (estimated for the material set Marques *et al.* used). This achieves even better results than the parametrization with $\alpha = 1/\epsilon_\infty$ [1].

To sum up, the density-based mixing method convinces with good results and its simplicity. Once the mixing parametrizations (2.31) are found, it is enough to calculate the quantity $\bar{g}$, which is a property of the ground state density and can be calculated with a (semi-)local functional, to improve hybrid functionals significantly.

3. Computational Methods

There are two distinct components that control the accuracy of DFT calculations: the level of theory (which was described in the previous chapter) and the numerical methods [7]. Therefore, in this chapter, we will present the approaches which are implemented in the DFT package **exciting** to ensure the required accuracy and precision. To start, we will introduce the standard methods of DFT algorithms, i.e. basis functions and self-consistent-field cycles (Chapter 3.1). This is proceeded by the description of advanced methods (Chapter 3.2), which were used to obtain ground state properties and band gaps for materials with indirect band gaps and significant SOC corrections. In the last part (Chapter 3.3), the computation of the density-based mixing method and its adaption to **exciting** are explained in detail.

3.1 Fundamentals of exciting

All calculations presented in this thesis are executed with the full-potential all-electron code **exciting**, which is developed by the solid-state theory group of the Physics Department of the Humboldt-University Berlin. The package implements DFT as well as its time-dependent expansion and many-body perturbation theory. As the thesis concentrates on band gap calculations, we will limit this introduction to ground state calculations on an generalized DFT level, i.e. to solve the (generalized) KS equations. Further details on the code can be found at the **exciting** web page [26], and in the respective publication [27], on which this chapter is mainly based.

3.1.1 Basis Functions

To solve the KS equation

$$H_{\mathrm{KS}}\,\psi_{i\mathbf{k}}(\mathbf{r}) = \varepsilon_{i\mathbf{k}}\psi_{i\mathbf{k}}(\mathbf{r}), \tag{2.14}$$

numerically, it is beneficial to choose an appropriate basis set $\{\phi_{\mathbf{G}}(\mathbf{r})\}$ and formulate the single-particle wave function $\psi_{i\mathbf{k}}$ as a linear combination of this basis [27]

$$\psi_{i\mathbf{k}}(\mathbf{r}) = \sum_{\mathbf{G}} C^{\mathbf{k}}_{i\mathbf{G}}\;\phi_{\mathbf{G}+\mathbf{k}}(\mathbf{r}). \tag{3.1}$$

Here, the summation is over all reciprocal lattice vectors $\mathbf{G}$, and $C^{\mathbf{k}}_{i\mathbf{G}}$ are the expansion coefficients, which give the best representation of the wave function. Both, the one-particle wave functions $\psi_{i\mathbf{k}}$ and the basis functions $\phi_{\mathbf{G}+\mathbf{k}}$, depend on the wave vector $\mathbf{k}$. Numerically, the reciprocal space cannot be sampled infinitesimally dense. Therefore, only a finite number of $\mathbf{k}$-vectors can be taken into account for the solution of the KS equation. In **exciting**, the grid, in which the reciprocal space is divided into, can be chosen with the input variable `ngridk`. It contains the number of points in one BZ in x-, y- and z-direction $n_x \times n_y \times n_z$. This grid is

important for all physical variables that require integration over the reciprocal space, such as the total energy, since the numerical integration is implemented as a summation over the **k**-point grid. Consequently, the denser the grid is, the more precise is the computation. However, the calculation time scales linearly with the number of **k**-points [26]. Therefore, a good compromise between precision and computational effort must be found.

The use of a discrete number of basis functions allows transforming the KS equation into a matrix equation

$$H^{\mathbf{k}}C^{\mathbf{k}} = \varepsilon^{\mathbf{k}}S^{\mathbf{k}}C^{\mathbf{k}}. \tag{3.2}$$

Here, $C^{\mathbf{k}}$ are the matrices containing the coefficients defined in equation (3.1). The matrix elements of the Hamiltonian $H^{\mathbf{k}}$ are calculated as

$$H^{\mathbf{k}}_{\mathbf{G}\,\mathbf{G}'} = \langle \phi_{\mathbf{G}+\mathbf{k}}| -\frac{1}{2}\nabla^2 + V_{\mathrm{KS}}(\mathbf{r})\,|\phi_{\mathbf{G}'+\mathbf{k}}\rangle\,. \tag{3.3}$$

Analogous the elements of the overlap matrices $S^{\mathbf{k}}$ read

$$S^{\mathbf{k}}_{\mathbf{G}\,\mathbf{G}'} = \langle \phi_{\mathbf{G}+\mathbf{k}}|\phi_{\mathbf{G}'+\mathbf{k}}\rangle\,. \tag{3.4}$$

Whether this eigenvalue problem (3.2) is properly solvable or not depends crucially on the chosen basis functions. Therefore, we will have a closer look at the basis function methods used in **exciting**.

Augmented plane wave method. As the wave functions behave differently in the space between the atoms and the vicinity of the nuclei, the idea on which the augmented plane wave (APW) method is based is to treat the two regions separately.

Near the nuclei, the wave functions underlie strong variations and especially the core states are mainly localized around the atomic sites. Therefore, spheres around the nuclei positions, named muffin-tin (MT) spheres, with radii R_{MT} can be defined. These radii may be chosen differently for every element and can be manually adapted in the **exciting** input (in the so-called species files). Within the MT regions, the KS potential is dominated by the atomic Coulomb term and is therefore mostly radial symmetric. Hence, the APW method substitutes the potential with a spherical-averaged effective potential $V_0(r)$ as a crude approximation. In reality, this is only valid for deep lying core states. Nevertheless, this approach yield as a good starting point for the construction of basis functions and more accurate calculations (like the linearized methods we discuss below) that consider the full potential. In accordance to the atomic-like radial-symmetric potential, spherical harmonics Y_{lm} and radial functions u_{la} are used to expand the wave function. The radial functions u_{la} need to satisfy the radial Schrödinger equation

$$\left[-\frac{1}{2}\frac{d^2}{dr^2} + \frac{l(l+1)}{2r^2} + V_0(r) - \varepsilon_{i\mathbf{k}}\right](r u_{la}(r)) = 0. \tag{3.5}$$

Here, l and m denote the angular and the magnetic quantum number of the electron state, respectively. a is the label of the associated atom. In **exciting**, a radial solver is used to evaluate equation (3.5), which is further explained in reference [27]. Even without solving the equation, one can see, that the u_{la} depend directly on the energy eigenvalues $\varepsilon_{i\mathbf{k}}$ of equation (2.14).

The space between the MT spheres is called interstitial (IT) region. Here, the wave functions vary more slowly, and hence, in the APW method, plane waves are used as basis functions. By taking this space partitioning into account, the whole basis set can be defined as

$$\phi_{\mathbf{G}+\mathbf{k}}(\mathbf{r}) = \begin{cases} \sum_{lm} A^{\mathbf{G}+\mathbf{k}}_{lma}\, u_{la}(r_a;\varepsilon_{i\mathbf{k}})\, Y_{lm}(\hat{\mathbf{r}}_a) & r_a \le R_{\mathrm{MT}} \\ \frac{1}{\sqrt{\Omega}}\exp\{i(\mathbf{G}+\mathbf{k})\mathbf{r}\} & \mathbf{r}\in \mathrm{IT} \end{cases}. \tag{3.6}$$

The sum in the first line goes over all possible quantum numbers l and m. $A^{\mathbf{G}+\mathbf{k}}_{lma}$ denotes the expansion coefficients for the wave functions in the MT spheres, and $\mathbf{r}_a = \mathbf{r} - \mathbf{R}_a$ refers to the

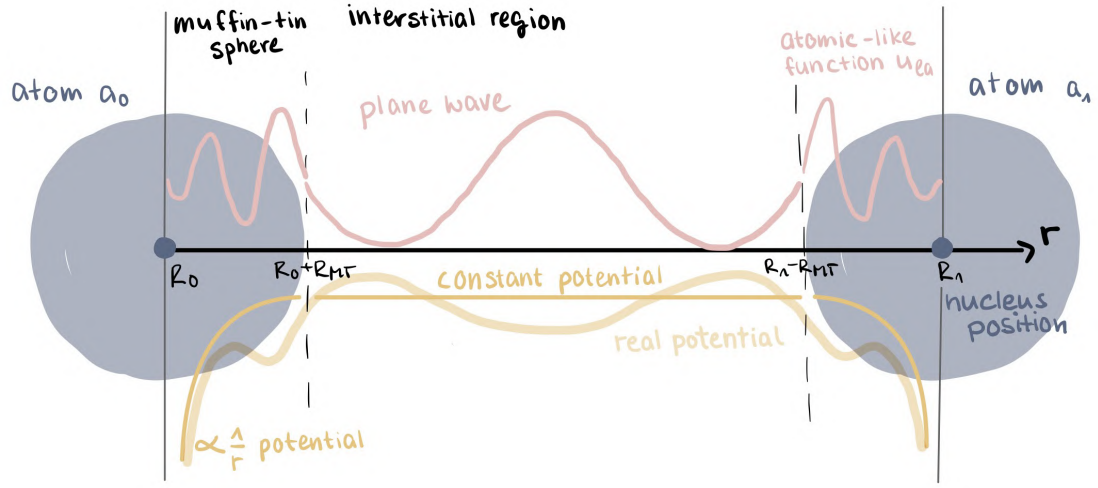

Figure 3.1: Schematic illustration of the APW method. The radial representation of two atoms at the coordinates R_0 and R_1 and the space division between them is shown. The blue areas represent the MT spheres, whereas the remaining space is the IT region. In the MT region, the potential and wave functions are approximated as atomic-like, whereas, in the IT region, the potential is assumed to be constant, and plane waves are used. Note that in the linearized versions of the APW method (LAPW), the full potential (indicated in light yellow) is considered instead of the approximation shown here.

space vector concerning the atomic position $\mathbf{R}_a$. Both regions are schematically shown in figure 3.1 with the respective potentials and basis functions of the APW method. At the border of the sections, the transition from atomic wave functions to plane waves has to be continuous. In other words, every plane wave in the IT region is augmented in the MT spheres, which gives the method its name.

Without further constraints, the sum in equation (3.1) and equally the dimension of the matrices in equation (3.2) would include an infinite amount of terms. To make the calculation feasible, the number of considered basis functions is made finite through the condition $|\mathbf{G}+\mathbf{k}| < G_{\max}$, which can be understood as a plane wave cutoff. However, the number of plane waves that are needed for an accurate calculation of the actual wave function also depends on the MT radius R_{MT}. If the latter is reduced, the wave functions vary more rapidly in the IT region and more plane waves are needed to approximate them. In **exciting**, the dimensionless product of the MT radius and the maximal reciprocal vector $R_{\mathrm{MT}} \cdot G_{\max}$ is used as a parameter, called `rgkmax`, to modify the basis size. If the solid consists of more than one element, the smallest R_{MT} value is used for the `rgkmax` definition. Again, a balance between the desired accuracy and the computational expense needs to be found. The calculation time scales with `rgkmax` to the power of nine [26], so especially for large systems, a change in `rgkmax` makes a huge difference.

Linearization and local orbitals. With the APW basis, the matrix equation (3.2) becomes highly non-linear as $\phi_{\mathbf{G+k}}(\mathbf{r})$ inherits the $\varepsilon_{i\mathbf{k}}$ dependence of u_{la}. To solve the problem of the eigenvalue $\varepsilon_{i\mathbf{k}}$ dependence, one can linearize the radial functions. An intuitive approach would be to evaluate the radial functions for a fixed energy parameter ε_{la} [27]

$$u_{la}(r_a;\varepsilon_{i\mathbf{k}}) \approx u_{la}(r_a;\varepsilon_{la}). \tag{3.7}$$

These fixed energy parameters are globally given for a certain angular quantum number l and a specific atom a. In other words, they do not depend on the band index i and the **k**-point, as the energy eigenvalues $\varepsilon_{i\mathbf{k}}$ do. This makes a one-to-one mapping complex. The corresponding mechanisms used in **exciting** are further explained in reference [27].

The resulting mismatch between the linearization energy ε_{la} and the actual energy eigenvalues $\varepsilon_{i\mathbf{k}}$ leads to an error of order $\mathcal{O}(\varepsilon_{la} - \varepsilon_{i\mathbf{k}})$ for the wave functions and $\mathcal{O}\left((\varepsilon_{la} - \varepsilon_{i\mathbf{k}})^2\right)$ for the total energy. To reduce the magnitude of the error and to increase the precision, it makes sense to consider the radial function expansion up to the second order

$$u_{la}(r_a; \varepsilon_{i\mathbf{k}}) \approx u_{la}(r_a; \varepsilon_{la}) + (\varepsilon_{la} - \varepsilon_{i\mathbf{k}}) \frac{\partial u_{la}(r_a; \varepsilon)}{\partial \varepsilon}\bigg|_{\varepsilon_{la}}. \tag{3.8}$$

Here, a dependence on the energy eigenvalue $\varepsilon_{i\mathbf{k}}$ is found as well. Therefore, rather than this exact expansion of $u_{la}(r_a; \varepsilon)$, a linear combination of $u_{la}(r_a; \varepsilon_{la})$ and $\dot{u}_{la}(r_a; \varepsilon_{la})$ is preferred. This approach is called the linearized APW (LAPW) method and leads to the following basis function in the MT spheres

$$\phi_{\mathbf{G}+\mathbf{k}}(\mathbf{r}) = \sum_{lm} \left[A_{lma}^{\mathbf{G}+\mathbf{k}} u_{la}(r_a; \varepsilon_{la}) + B_{lma}^{\mathbf{G}+\mathbf{k}} \dot{u}_{la}(r_a; \varepsilon_{la}) \right] Y_{lm}(\hat{\mathbf{r}}_a) \quad r_a \leq R_{\mathrm{MT}}. \tag{3.9}$$

Again $A_{lma}^{\mathbf{G}+\mathbf{k}}$ and $B_{lma}^{\mathbf{G}+\mathbf{k}}$ are coefficients of the linear combination determined by the continuity of basis function and its derivative, respectively. In the IT region, the basis functions are identical to the plane waves of the APW method. This linear combination of the radial function and its derivative decreases the error for the wave functions to an order $\mathcal{O}\left((\varepsilon_{la} - \varepsilon_{i\mathbf{k}})^2\right)$ and the error for the total energy to $\mathcal{O}\left((\varepsilon_{la} - \varepsilon_{i\mathbf{k}})^4\right)$.

Unfortunately, this linearization method treats different states with the same l equally, through which it does not distinguish accurately between valence and core electrons. By considering these two groups separately, one can bypass the problem mostly. Only semi-core states, which are not sufficiently localized in the MT and significantly overlap with valence states, remain critical. For this purpose, local orbitals (lo's) have been additionally employed within the APW method. They are localized atomic-like functions, which are non-zero only inside a single MT sphere belonging to the atom a_μ and are constructed for fixed quantum numbers l_μ and m_μ (which can be individually chosen). The lo's include the linearization energy of valence states ε_{la} as well as the energy parameter of the semi-core states $\varepsilon_{la}^{\mathrm{sc}}$ and read

$$\phi_\mu(\mathbf{r}) = \begin{cases} \delta_{aa_\mu}\delta_{ll_\mu}\delta_{mm_\mu} \left[a_\mu u_{la}(r_a; \varepsilon_{la}) + b_\mu u_{la}(r_a; \varepsilon_{la}^{\mathrm{sc}}) \right] Y_{lm}(\hat{\mathbf{r}}_a) & r_a \leq R_{\mathrm{MT}} \\ 0 & \mathbf{r} \in \mathrm{IT}. \end{cases} \tag{3.10}$$

They need to vanish at the MT boundary and fulfil the normalization condition. The combination of the lo's with the APW method leads to the following KS wave functions

$$\psi_{i\mathbf{k}}(\mathbf{r}) = \sum_{\mathbf{G}} C_{i\mathbf{G}}^{\mathbf{k}}\, \phi_{\mathbf{G}+\mathbf{k}}(\mathbf{r}) + \sum_{\mu} C_{i\mu}^{\mathbf{k}} \phi_\mu(\mathbf{r}). \tag{3.11}$$

After inserting the basis functions (3.6) and (3.10) for the MT regions, it is possible to write the equation compactly as [27]

$$\psi_{i\mathbf{k}}(\mathbf{r}) = \sum_{lm} \left[c_{lm}^{i\mathbf{k}} u_{la}(r_a; \varepsilon_{la}) + d_{lm}^{i\mathbf{k}} u_{la}(r_a; \varepsilon_{la}^{\mathrm{sc}}) \right] Y_{lm}(\hat{\mathbf{r}}_a) \quad r_a \leq R_{\mathrm{MT}}. \tag{3.12}$$

The coefficients $c_{lm}^{i\mathbf{k}}$ and $d_{lm}^{i\mathbf{k}}$ are combination of the APW and lo coefficients. As they are linearly independent one of them vanishes when the state, with respective l of the lo, is a valence state or a semi-core state [27]. Hence, the APW+lo basis no longer produces a degeneracy in l.

In the same manner, lo's can be used for the linearization of valence states. For this, instead of the semi-core energy parameter, the derivative of the radial function $\dot{u}_{la}$ is included

$$\phi_\mu(\mathbf{r}) = \delta_{aa_\mu}\delta_{ll_\mu}\delta_{mm_\mu} \left[a_\mu u_{la}(r_a; \varepsilon_{la}) + b_\mu \dot{u}_{la}(r_a; \varepsilon_{la}) \right] Y_{lm}(\hat{\mathbf{r}}_a) \quad r_a \leq R_{\mathrm{MT}}. \tag{3.13}$$

The resulting wave functions

$$\psi_{i\mathbf{k}}(\mathbf{r}) = \sum_{lm} \left[c_{lm}^{i\mathbf{k}} u_{la}(r_a; \varepsilon_{la}) + d_{lm}^{i\mathbf{k}} \dot{u}_{la}(r_a; \varepsilon_{la}) \right] Y_{lm}(\hat{\mathbf{r}}_a) \tag{3.14}$$

are remarkably similar to the LAPW basis (3.9), but different conditions apply for the coefficients. $c_{lm}^{i\mathbf{k}}$ and $d_{lm}^{i\mathbf{k}}$ can be chosen more flexible. Hence, the linearization error is smaller and the results more precise.

With both linearization techniques, the APW method is sufficiently extended to LAPW+lo. To solve the KS accurately, additionally to constructing a suitable basis for the wave functions, also the KS potential needs to be considered adequately. In LAPW+lo, the full potential is taken into account without further approximations. This means, the KS potential is expanded with spherical harmonics in the MT spheres and treated as a Fourier series in the IT regions

$$V_{\mathrm{KS}}(\mathbf{r}) = \begin{cases} \sum_{lm} V_{lm}(\mathbf{r})\, Y_{lm}(\hat{\mathbf{r}}_a) & r_a \leq R_{\mathrm{MT}} \\ \sum_{\mathbf{k}} V_{\mathbf{k}}(\mathbf{r})\, \exp\{i\mathbf{k}\mathbf{r}\} & \mathbf{r} \in \mathrm{IT}\ . \end{cases} \tag{3.15}$$

With that, the LAPW+lo method achieves the most precise results and are widely considered as the gold standard of DFT. Which basis is used for a specific calculation can be chosen individually inside the mentioned species files[viii].

3.1.2 Self-Consistent-Field Cycle

The KS potential V_{KS} (2.16) depends on the electron density itself, as described in Chapter 2.2. Therefore, the KS equation has to be solved in a self-consistent manner, where the newly gained electron density updates the KS potential.

Steps of the self-consistent-field cycle. The process of the self-consistent-field cycle (SCF) is schematically shown in figure 3.2. As an initial guess, the superposition of all single-atom densities is used to construct the KS potential, as long as there is no previous DFT calculation. This ansatz is reasonable as the sum of overlapping atom densities is rather similar to the actual electron density of solids [6]. Based on the initial guess, the KS equation is solved for all states. Here, the core states are computed separately as the associated electrons do not interact with electrons of other atoms and only contribute within the MT spheres. In codes like VASP, which do not treat the full potential, the core electrons are not calculated explicitly but are included in the pseudo-potential.

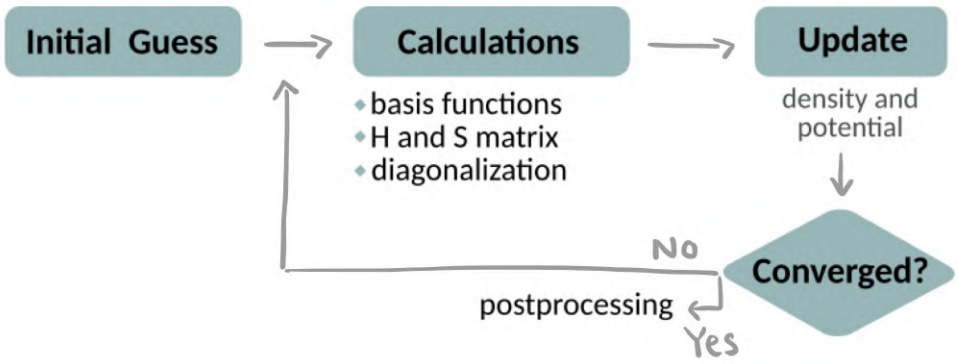

Figure 3.2: SCF in **`exciting`**. Based on an initial guess, the core wave functions and basis functions are constructed. Moreover, the Hamiltonian and the overlap matrix are computed. After their diagonalization, the electron density and the KS potential are updated. If the results have changed significantly, i.e. are not converged, the steps are repeated with a new starting point, which takes the previous results for the electron density into account.

Solving the KS equation starts with the computation of the basis functions. They need to be calculated in every SCF step as the potential changes with every iteration and thus the

[viii] For the example of Ne, two species files are shown in Appendix A.5.

linearization parameter ε_{la} can be updated. Afterwards, the Hamiltonian $H^{\mathbf{k}}$ (eq. 3.3) and the overlap matrices $S^{\mathbf{k}}$ (eq. 3.4) are constructed and diagonalized in order to solve the matrix equation $H^{\mathbf{k}}C^{\mathbf{k}} = \varepsilon^{\mathbf{k}}S^{\mathbf{k}}C^{\mathbf{k}}$ (3.2). In this step, the diagonalization is the most time-consuming part with a complexity of order $\mathcal{O}(N_{\mathrm{b}}^3)$ with N_{b} as the number of basis functions. With the so gained coefficients $C^{\mathbf{k}}_{i\mathbf{G}}$, the single-particle wave functions $\psi_{i\mathbf{k}}(\mathbf{r})$ (eq. 3.1) can be extracted, and the electron density $n(\mathbf{r})$ (eq. 2.7) can be updated.

Based on the electron density, the KS potential $V_{\mathrm{KS}}[n]$ is computed. In particular, the external and the Hartree potential are updated through the Poisson equation as these terms build the electrostatic component of the potential

$$\Delta\left[V_{\mathrm{ext}}(\mathbf{r}) + V_{\mathrm{Hartree}}(\mathbf{r})\right] = 4\pi\left(n(\mathbf{r}) - \sum_a Z_a\delta(r_a)\right). \tag{3.16}$$

Here r_a is the radial component of the difference to the atomic position of the atom a (compare eq. 3.6), and Z_a is the number of protons included in the respective nucleus.

The solution is then compared with the initial potential. More specifically, the results of the m-th step are compared with the results of the $(m-1)$-th step. The calculation succeeded if in two consecutive steps the required convergence criteria are met. **exciting** uses the following criteria as default (given in atomic units):

RMS change in effective potential	$\leq$	$0.10 \cdot 10^{-05}$
Absolute change in total energy	$\leq$	$0.10 \cdot 10^{-05}$
Charge distance	$\leq$	$0.10 \cdot 10^{-04}$.

If one of the criteria is not met (one can also select a specific criterion), the steps of the SCF are repeated with the updated potential until the criteria are reached. To speed up the calculation and ensure the convergence of this iterative calculation, the density used for the following step is computed by employing an appropriate mixing scheme between the m-th and the $(m-1)$-th density. Further details on the mixing are given in reference [27].

SCF for hybrid functionals. For hybrid functionals, also the non-local potential (2.19) needs to be taken into account. Evaluated in reciprocal space, every matrix element of the potential becomes a six-dimensional integral [15]

$$V^{\mathrm{HF}}_{\mathrm{x},ij}(\mathbf{k}) = -\sum_{l}^{\mathrm{occ}}\sum_{\mathbf{q}}^{\mathrm{BZ}}\iint \mathrm{d}^3r\,\mathrm{d}^3r'\,\frac{\psi^*_{i\mathbf{k}}(\mathbf{r})\psi_{l\mathbf{q}}(\mathbf{r})\psi^*_{l\mathbf{q}}(\mathbf{r'})\psi_{j\mathbf{k}}(\mathbf{r'})}{|\mathbf{r}-\mathbf{r'}|}\,. \tag{3.17}$$

To simplify the six-dimensional integral, the so-called mixed product basis $\{M_{I\mathbf{k}}(\mathbf{r})\}$ is used. These functions are constructed from the LAPW basis and are defined to represent wave function products [15], which simplifies the dividend of $V^{\mathrm{HF}}_{\mathrm{x},ij}$. With that, the non-local exchange decomposes into a vector-matrix-vector product [15]

$$V^{\mathrm{HF}}_{\mathrm{x},ij}(\mathbf{k}) = -\sum_{l}^{\mathrm{occ.}}\sum_{\mathbf{q}}^{\mathrm{BZ}}\sum_{IJ}\left\langle\psi_{i\mathbf{k}}\middle|\psi_{l\mathbf{k}-\mathbf{q}}M_{I\mathbf{q}}\right\rangle v_{IJ}(\mathbf{q})\left\langle M_{J\mathbf{q}}\psi_{l\mathbf{k}-\mathbf{q}}\middle|\psi_{j\mathbf{k}}\right\rangle, \tag{3.18}$$

where v_{IJ} is the bare Coulomb potential, which is independent of the wave functions. This separation of the integral into parts that are not wave function dependent makes it more feasible. Moreover, as the exchange energy adds a relatively small contribution (compared with kinetic energy and potential energy), one can describe the non-local exchange in a subspace of wave functions up to a band cutoff $i_{\mathrm{max}} \geq i, j$ [15]. This cutoff defines the dimension of the matrix $V^{\mathrm{HF}}_{\mathrm{x}}$, i.e. the number of matrix elements that have to be computed. In **exciting**, this cutoff is adjustable by means of the parameter `nempty` $= i_{\mathrm{max}} - i_{\mathrm{occ}}$, which is the number of empty

states considered in addition to the number of occupied states. `nempty`, thus, becomes an essential convergence parameter for hybrid calculations.

For the first calculation of the non-local exchange potential V_x^{HF}, the KS orbitals of a PBE calculation are used. Once these non-local calculations are completed, an SCF is executed, analogously to the process discussed above, with a hybrid xc functional E_{xc}^{hyb} (see Chapter 2.5). In the framework of hybrids, this is called inner SCF since the non-local calculations are not included. In the inner SCF, the generalized KS approach is used to calculate the ground state since a hybrid functional is elaborated, i.e. the generalized KS equation (2.20) is solved. Once the inner SCF is completed, the results are compared to the previous step in an outer SCF. This is schematically shown in figure 3.3. In this outer cycle, only the charge distance is used as a convergence criterion. If it is not met, the non-local calculations are repeated with updated electron states $\psi_{i\mathbf{k}}$.

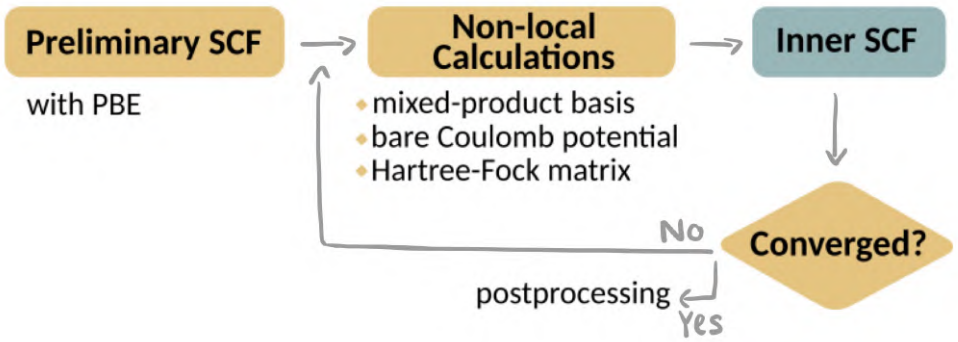

Figure 3.3: SCF for hybrid functionals. Based on a PBE calculation, the non-local exchange potential is calculated in three steps: construction of the mixed-product basis, calculation of the bare Coulomb potential with the help of this basis, and the evaluation on the bare Coulomb potential onto the actual wave functions, creating the HF matrix. With this, an inner SCF (as described in figure 3.2) is evaluated for the hybrid xc functional E_{xc}^{hyb}. In an additional self-consistent manner, the results are compared to the previous electron density, and the calculation is repeated until the convergence criterion for the charge density is met.

3.2 Advanced Methods

Some of the materials employed in this thesis have indirect band gaps or significant spin-orbit coupling effects. For this reason, more advanced methods are necessary to reliably obtain their band gaps.

3.2.1 Wannier Functions

For materials with a direct band gap, the conduction band minimum (CBM) and the valence band maximum (VBM) are found at the same point in the reciprocal space. With an appropriate choice of the reciprocal space grid, the direct band gap is immediately accessible at the end of a DFT ground state calculation. However, for materials with an indirect band gap, the CBM and VBM can lie at different arbitrary points in reciprocal space. In order to get an accurate calculation of their energy values, an interpolation scheme is needed. In **`exciting`**, this is realized through maximally localized Wannier functions (MLWFs). For the derivation of those, we closely follow reference [28].

Wannier functions $\omega_{i\mathbf{R}}$ are an alternative representation to Bloch functions $\psi_{i\mathbf{k}}$. Whereas the latter build eigenfunctions of the KS Hamiltonian for a given band i and a given crystal

momentum $\mathbf{k}$, the first are localized in real space. Therefore, Wannier functions provide a clear chemical interpretation [28]. Both representations are connected through a Fourier transform, where $\mathbf{R}$ is the respective real-space lattice vector [28],

$$\omega_{i\mathbf{R}}(\mathbf{r}) = \frac{1}{N_{\mathbf{k}}} \sum_{\mathbf{k}} e^{-\mathrm{i}\mathbf{k}\mathbf{R}}\, \varphi_{i\mathbf{k}}(\mathbf{r}). \tag{3.19}$$

Here, $N_{\mathbf{k}}$ is the total number of non-reduced $\mathbf{k}$-points, which means the number specified in `ngridk`. For an isolated band, the wave function $\varphi_{i\mathbf{k}}$ can be replaced by the respective Bloch function $\psi_{i\mathbf{k}}$ [28]. This occurs for deep-lying energies, i.e. mostly core or semi-core states. However, for an isolated group of J overlying bands, the wave functions are built as a linear combination of the included single-particle Bloch functions

$$\varphi_{i\mathbf{k}}(\mathbf{r}) = \sum_{j=1}^{J} U^{\mathbf{k}}_{ji} \psi_{j\mathbf{k}}(\mathbf{r}). \tag{3.20}$$

Here, $U^{\mathbf{k}}$ refers to a unitary $J \times J$ matrix, which can be chosen without further constraints [28]. Valence bands often build isolated groups of bands.

For conduction bands or metallic materials, commonly, no isolated groups of bands can be found. Instead, all of the bands are overlying and need to be disentangled in order to find the Wannier functions. For that matter, an (outer) energy window of interest is chosen. Again, one wants to construct a set of J wave functions, which number needs to be less than the number of bands included in the energy window $\mathcal{J}_{\mathbf{k}} \geq J$. The disentanglement [28]

$$\widetilde{\psi}_{j\mathbf{k}}(\mathbf{r}) = \sum_{\mu=1}^{\mathcal{J}_{\mathbf{k}}} \widetilde{U}^{\mathbf{k}}_{\mu j} \psi_{\mu\mathbf{k}}(\mathbf{r}) \tag{3.21}$$

uses the rectangular semi-unitary $\mathcal{J}_{\mathbf{k}} \times J$ matrix $\widetilde{U}^{\mathbf{k}}$. Here, $\psi_{\mu\mathbf{k}}(\mathbf{r})$ are the single-particle wave functions, which energy eigenvalues are within the (outer) energy window. Additionally, an inner window can be chosen, in which the disentangled wave functions $\widetilde{\psi}_{j\mathbf{k}}$ stay unchanged, i.e. $\widetilde{U}^{\mathbf{k}}_{\mu j} = \delta_{\mu j}$. Once the disentangled J-dimensional subspace is found for every $\mathbf{k}$-point, the disentangled wave functions are treated in the way of isolated band groups (e.q. 3.20) [28].

The freedom of the unitary matrix $U^{\mathbf{k}}$ in (3.20) makes it possible to manipulate the localization of the Wannier function in order to find MLWFs. This is done by iterative minimization of the Wannier function spread [28]

$$\Omega = \sum_{i} \left[\langle \omega_{i\mathbf{0}} |\, r^2 \,| \omega_{i\mathbf{0}} \rangle - \langle \omega_{i\mathbf{0}} |\, \mathbf{r} \,| \omega_{i\mathbf{0}} \rangle^2 \right]. \tag{3.22}$$

This minimization, however, highly depends on a good initial guess for the Wannier function as it is a non-linear and high-dimensional optimization problem. In **exciting**, optimized projection functions are used to automatically construct a reliable starting point from a large set of lo's. Further details can be found in reference [28].

Once MLWFs are found, they can be used for an interpolation scheme through the inverse transform of the Wannier function into reciprocal space [28]

$$\varphi_{i\mathbf{q}}(\mathbf{r}) = \sum_{\mathbf{R}} e^{\mathrm{i}\mathbf{q}\mathbf{R}}\, \omega_{i\mathbf{0}}(\mathbf{r} - \mathbf{R}). \tag{3.23}$$

This equation gives the wave function for an arbitrary point $\mathbf{q}$ in reciprocal space for which an interpolation is needed. Based on the diagonalization of $\mathcal{H}^{\mathbf{q}}_{ji} = \langle \varphi_{j\mathbf{q}} |\, \hat{H} \,| \varphi_{i\mathbf{q}} \rangle$, the energy eigenvalues $\varepsilon^{\mathbf{q}}_i$ are easily obtained, as $\mathcal{H}^{\mathbf{q}}$ only has the (comparably small) dimension J, which is the number of considered bands [28]. Hence, it becomes possible to evaluate the band structure on a much denser grid than initially considered by the reciprocal space dissection (`ngridk`). With that, the right VBM and CBM energies can be found and hence, the band gap can be determined precisely.

3.2.2 Spin-Orbit Coupling

The approach of solving the KS equation, as it is described in the previous chapters, does not include the electron spin. However, taken into account, the spin may lead to a relative shift in the energy levels and, hence, influences the magnitude of the calculated band gap. The influence is a result of the interaction between the magnetic moment of the electron spin and the electric field of the nucleus through which the electron moves. This effect is widely known as spin-orbit coupling (SOC). The coupling leads to a reduction of energy level degeneracy and has notable effects mainly in heavy atoms.

The SOC term connects spin-up and spin-down wave functions. Therefore, when SOC is taken into account, the number of basis functions doubles compared to the case without spin, i.e. N_b basis functions lead to $2N_\mathrm{b} \times 2N_\mathrm{b}$ secular equations to solve [29]. To avoid that immense computational effort, in **exciting**, the inclusion of the SOC Hamiltonian is realized by a second variational scheme. As the SOC usually has a small effect, this is well suited for its inclusion. The second variational method is based on a DFT calculation without SOC as the first variation. It uses the obtained KS orbitals $\psi_{i\mathbf{k}}$ to create a spinor basis of size N_s

$$\bar{\phi}_{i\mathbf{k}} = \begin{cases} \begin{pmatrix} \psi_{i\mathbf{k}} \\ 0 \end{pmatrix} & 1 \leq i \leq \frac{N_\mathrm{s}}{2} \\ \begin{pmatrix} 0 \\ \psi_{(i-N_\mathrm{f})\mathbf{k}} \end{pmatrix} & \frac{N_\mathrm{s}}{2} < i \leq N_\mathrm{s} \end{cases} . \tag{3.24}$$

$N_\mathrm{f} = N_\mathrm{s}/2$ is the number of states considered from the first variational calculation, including occupied and empty states. Only the N_f lowest KS orbitals are used, as the SOC effect has a larger effect in the region near the nucleus, and therefore, has a greater impact on core and semi-core states. Consequently, the spinor basis size N_s, typically, can be chosen significantly smaller than the KS basis size. How many empty states are taken into account in the calculation, are again specified by the `nempty` parameter in **exciting**. Hnece, it is an important parameter to converge with respect to the band gap when the second variational scheme is employed.

In this basis, the overlap matrix S becomes diagonal [29], i.e., $S_{ij} = \delta_{ij}$ for low lying bands. Thus, the second variational Hamiltonian consists of the SOC Hamiltonian and the energy eigenvalues found in the first variation added up on the main diagonal [29]

$$H_{ij} = \varepsilon_i \delta_{ij} + H_{ij}^\mathrm{SOC}. \tag{3.25}$$

The form of the SOC Hamiltonian is derived through the zero-order regular approximation (ZORA). Inside the MT regions H resembles [27]

$$H_\mathrm{ZORA}^\mathrm{SOC} = \frac{\alpha_\mathrm{fs}^2}{[2 - \alpha_\mathrm{fs}^2 v_0(r)]^2} \frac{1}{r} \frac{\partial V_0(r)}{\partial r} \tilde{\boldsymbol{\sigma}} \cdot \mathbf{L}. \tag{3.26}$$

Here α_fs is the fine-structure constant, $V_0(r)$ the averaged effective potential (compare eq. 3.5) and $\tilde{\boldsymbol{\sigma}} = (\tilde{\sigma}_x, \tilde{\sigma}_y, \tilde{\sigma}_z)$ are the Pauli matrices. Outside the MT sphere, the SOC can be neglected [29]. This extended Hamiltonian is used to solve the (generalized) KS equation for calculations with SOC.

3.3 Computational Details

All the computational methods introduced so far are included in the calculations to reproduce the band gap and the ground state electron density as accurately as possible. Equipped with a good understanding, how **exciting** solves the KS equation, which numerical parameters are essential, and how special features like indirect band gaps and SOC are treated, in this

chapter, we will focus on the description of the density-based mixing method and how the numerical methods are applied. As explained in Chapter 2.6, the density-based mixing method is a polynomial regression that models the relation between an optimal mixing parameter α_{opt} and the density-based quantity $\bar{g}$. Therefore, we will discuss these parameters in detail and the material set on which the regression is based. Moreover, at the end of the chapter, we will briefly explain which computational approach we used to evaluate the obtained fits.

3.3.1 Material Set

In order to make the method applicable for a huge range of materials, the set of materials used to apply the fit onto needs to be large enough and represent different types of materials. In this thesis, we used the material set from the original paper [1], which contains 21 samples. In addition to them, we included PbI_2 to additionally cover a material with a significant SOC effect. Other than that, we calculated the SOC correction for Kr, Xe and CdS, which will be further discussed in Chapter 4.2.2. The experimental band gaps of the materials cover a wide range, from 0.74 eV to 21.70 eV, with 14 direct band gaps and 7 indirect band gaps. The crystal structures, which are included in the material set, are face-centred cubic (fcc), diamond, rock salt, zincblende and wurtzite structure as well as two other structures. Marques *et al.* provided

Table 3.1: Classification of the material set based on the materials crystal structure, their band gap size (in eV) and type (direct D or indirect I), their group of the element in the periodic table of elements (PTE) and valence electrons as well as their electronic and physical properties. The material classes in the last column are assigned according to reference [3]: noble gases (noble), semiconductors (sc), ionic bound materials (ionic) and transition metal compounds (TmX). The materials labelled with † are the ones for which α_{opt} and $\bar{g}$ were explicitly computed during this work. The results for the other materials were provided by C. Vona. References for each table entry are given in the appendix, in table B.1.

material	structure	exp. E_{gap} in eV	gap type	PTE group	valence electrons	material class
Ne†	fcc	21.70	D	VIII	8	noble
Ar	fcc	14.20	D	VIII	8	noble
Kr†	fcc	11.60	D	VIII	8	noble
Xe†	fcc	9.80	D	VIII	8	noble
C	diamond	5.48	D	IV	4	sc
Si	diamond	1.17	I	IV	4	sc
Ge†	diamond	0.74	I	IV	4	sc
LiF	rock salt	14.20	D	I-VII	8	ionic
LiCl†	rock salt	9.40	D	I-VII	8	ionic
MgO	rock salt	7.83	D	II-VI	8	ionic
SiC†	zincblende	2.40	I	IV-IV	8	sc
BN†	zincblende	6.25	I	III-V	8	sc
GaN†	zincblende	3.20	D	III-V	8	sc
GaAs	zincblende	1.52	D	III-V	8	sc
AlP†	zincblende	2.45	I	III-V	8	sc
ZnS†	zincblende	3.91	D	Tm-VI	18	TmX
CdS†	zincblende	2.42	D	Tm-VI	18	TmX
AlN†	wurtzite	6.28	D	III-V	8	sc
SiO_2†	α-quarz	10.30	I	IV-VI	16	—
MoS_2†	MoS_2	1.29	I	Tm-VI	18	TmX
ZnO	wurtzite	3.44	D	Tm-V	18	TmX
PbI_2	—	2.55	D	IV-V	14	ionic

us with the experimental crystal structures and lattice parameters to have a better analogue to the experiment. Furthermore, the materials could be classified according to their physical properties. Our analysis was oriented on the suggested division by Koller et al. [3]. Based on their characterization, we can see that most of the materials are semiconductors. The rest are noble gases, have ionic bonds, or include transition metals.

All this information about the materials is summarized in table 3.1, in which also the experimental gaps are given. Among the materials in table 3.1, the samples labelled with † are the ones for which α_{opt} and $\bar{g}$ were explicitly computed during this work. The additional calculations were provided by C. Vona, who also implemented $\bar{g}$ in **`exciting`**. Her data is considered in this thesis to design the density-based mixing method with the whole material set that was used in the original publication [1].

3.3.2 Optimal Mixing Parameter α_{opt}

In hybrid functionals, by changing the mixing parameter α from 0 to 1, one has a continuous transition between the (semi-)local KS approach and the HF theory (compare Chapter 2.5). For multiple materials this transition is observed to be linear (see for example reference [4]). In other words, the size of the band gaps computed with the hybrid functionals PBE0 and HSE06 can be directly adjusted by the mixing parameter α. Also, both functional reproduce PBE for $\alpha = 0$. This observation can be used to evaluate the optimal mixing parameter α_{opt}, which is the fraction of HF exchange for which the experimental gap is obtained.

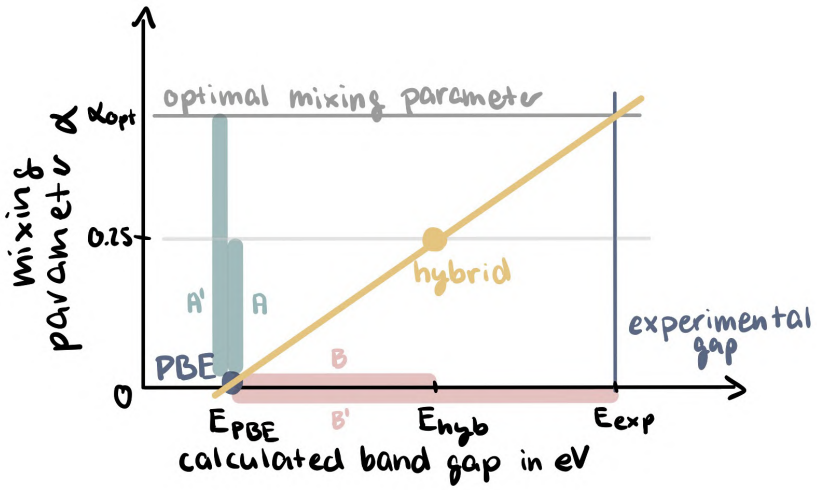

Figure 3.4: Schema for the computation of the optimal mixing parameter. Because of the linear dependence between the calculated energy gap and the mixing parameter, the ratios between two mixing parameters and two band gaps need to be equal. Therefore, one can estimate the optimal mixing parameter based on the value of the experimental energy gap (eq. 3.27).

As shown in figure 3.4, the linear dependence between the mixing parameter and the calculated band gap has the consequence that the ratio between two mixing parameter differences is equal to the ratio between two energy gap differences

$$\frac{\alpha_i - \alpha_j}{\alpha_k - \alpha_j} = \frac{E^i_{\text{gap}} - E^j_{\text{gap}}}{E^k_{\text{gap}} - E^j_{\text{gap}}} \quad \Longrightarrow \quad \alpha_{\text{opt}} = \frac{E^{\text{exp}}_{\text{gap}} - E^{\text{PBE}}_{\text{gap}}}{E^{\text{hyb}}_{\text{gap}} - E^{\text{PBE}}_{\text{gap}}} \cdot 0.25 \,. \tag{3.27}$$

Here α_i is the mixing parameter used for the functional i, with which the band gap E^i_{gap} is calculated. This can be simplified as for both hybrid functionals, α_{hyb} equals 0.25, and for the

PBE calculation, $\alpha_{\text{PBE}} = 0$ (compare definitions of PBE0 and HSE06). Hence, the optimal mixing parameter can directly be computed with the use of the experimental gap $E_{\text{gap}}^{\text{exp}}$. Consequently, for every material, the band gaps had to be determined with PBE, PBE0 and HSE06 to gain the optimal mixing parameters α_{opt} for both hybrid functionals. The experimental gaps were taken from reference [1] (given in table 3.1).

Each calculation had to be converged with respect to the main numerical parameter to gain reliable results for the band gap. Several examples of the convergence are given in the Appendix A. As introduced in detail in the previous chapters, two numerical parameters influence the ground state calculation with semi-local functionals the most: the size of the basis set `rgkmax` and the number of **k**-points `ngridk`. The first one is defined through the product of the MT radius and the plane wave cutoff `rgkmax` $= R_{\text{MT}} \cdot \mathbf{G}_{\text{max}}$, and the latter specifies the density of the grid with which the BZ is sampled in reciprocal space. The basis functions and R_{MT} were specified in the species files. To calculate the properties as accurately as possible, we used species files determined by S. Lubeck, who tested the right amount of lo's to be included and the best value for the MT radius. In hybrid calculations, in addition, also the number of empty states `nempty`, which are considered additionally to the occupied states, is fundamental for the computation of the non-local exchange.

For the materials with SOC or an indirect band gap, the advanced methods, which were discussed in chapter 3.2, had to be included, leading to an advanced convergence testing. For SOC, this means a convergence of `nempty` for semi-local calculations. For the Wannier functions, also the parameters specifying the construction of the MLFW needed to be established. The most difficult part was to determine the inner and outer energy windows. These values define which conduction bands are considered in the disentanglement. Enough bands have to be included in the inner window to give a good interpolation of the lowest conduction band. Moreover, for the disentanglement, the outer energy window should be close to the boundaries of the inner window. However, to make the minimization of the spread Ω possible, enough variational freedom in the disentanglement need to be included. Hence, the outer energy window needs to be sufficiently larger than the inner, and a balance between these effects had to be found [28]. To be able to define a good outer window, enough empty states (`nempty`) have to be included in the calculation. Thus, `nempty` is a crucial convergence parameter for the MLWFs. Furthermore, for the valence bands, in each calculation it needed to be specified individually which bands were included in the isolated group and which were not taken into account. In particular, very deep-lying bands can be left out of consideration to save computation time. Which ones need to be considered was investigated for each material individually. Once the right parameters are found, in **`exciting`**, the property `wanniergap` can be added to the input file. This leads to an automized search for the VBM and CBM using the calculated Wannier functions. The required interpolation grid is determined automatically by the code or can be chosen manually.

Once the change in its numerical parameter does not lead to sufficient change in the ground state properties, the calculations are considered as converged. Due to the definition of the convergence criterion, one can vary the desired precision. For the energy gap, a convergence criterion of 0.02 eV was used, i.e. if for all higher values of the numerical parameter the difference between the band gap results is smaller than 0.02 eV, the calculation has converged. The smallest values for `rgkmax`, `ngridk` and `nempty` for all band gap calculation are given in the appendix (table A.1). As we have a precision of two digits in the energy gaps, we rounded the values for α_{opt} to the second digit as well.

3.3.3 Density-Based Quantity $\bar{g}$

For $\bar{g}$, we had no clear physical intuition. Marques *et al.* derived it with the argument of averaging an estimator of the local band gap [1], but clearly (the unit of $\bar{g}$ is $\sqrt{a_0}$), it is not an

energy value. Moreover, the square root inside the quantity

$$\bar{g} = \frac{1}{V_{\text{cell}}} \int_{\text{cell}} \mathrm{d}^3 r \sqrt{\frac{|\nabla n(\mathbf{r})|}{n(\mathbf{r})}} \tag{2.29}$$

was chosen empirically to make $\bar{g}$ more stable.

Still, we can see that it depends on the same numerical parameters as the energy gap. Since $\bar{g}$ is computed with the all-electron electron density n, which is as well as the energy eigenvalues estimated by solving the KS equations (2.14), $\bar{g}$ is influenced by the basis size `rgkmax` and the **k**-point grid `ngridk`. For hybrid functionals, SOC corrections or Wannier interpolation, the number of empty states `nempty` also had to be considered.

For the energy gap, it is very well tested to which extend we can trust the code and which discrepancies have numerical reasons (the standard convergence criterion is 0.02 eV as mentioned before). This was different for the $\bar{g}$ quantity, due to the complex relation between $\bar{g}$ and n and the fact that the electron density is a local quantity. So we had to define a convergence criterion with respect to those parameters ourselves. Therefore, we did a detailed analysis of $\bar{g}$ with respect to the basis size `rgkmax` and the **k**-point grid `ngridk`. Specifically, we evaluated which influence the variation of $\bar{g}$ has on the mixing parameter α_{mix} (eq. 2.31) from Marques *et al.* (see Appendix A). Based on a desired precision of two digits for α_{mix}, we suggest

$$\pm 0.005 \sqrt{a_0} \tag{3.28}$$

as the convergence criterion for $\bar{g}$.

A comparison of the numerical parameters for which $\bar{g}$ is converged with this criterion and the numerical parameter which are needed for a converged energy gap reveals that they are quite similar (see table A.1). So the criterion does not lead to unreasonable high numerical parameters, i.e. high computational expense.

3.3.4 Evaluating the Fit

In order to evaluate the density-based mixing method and to compare different fits, we needed an indicator that directly determines how good the reproduction of the experimental gaps is. Our preferred choice for that is the root-mean-squared error (RMSE) between the experimental gap and the calculated energies using the improved mixing parameter.

Since we will evaluate the performance of many fits, to repeat the hybrid calculations for every new fit with all 21 materials would be computationally too demanding. Instead, in order to compare the band gap results obtained from the mixing method with the experimental ones, we decided to estimate the band gap with the strategy we used to estimate α_{opt}. In equation (3.27), the optimal mixing parameter and the experimental band gap can be substituted with the mixing parameter α_{mix} and the band gap E_{mix} associated with the density-based mixing method. Rearranging the equation leads to the following expression

$$E_{\text{mix}} = \frac{\alpha_{\text{mix}}}{0.25} \cdot E_{\text{gap}}^{\text{hyb}} + \left(1 - \frac{\alpha_{\text{mix}}}{0.25}\right) \cdot E_{\text{gap}}^{\text{PBE}} \,. \tag{3.29}$$

Then, we inserted $\alpha_{\text{mix}} = \mathrm{a} \cdot \bar{g}^n + \mathrm{b}$ for every fit and the individual $\bar{g}$ for each material.

The linearity we are using here is not perfectly satisfied by all materials (detailed discussion in Appendix C.2). However, this also affects the calculation of α_{opt}, for which this is the usual method. Moreover, we expect that the effects should cancel each other.

All fits for the density-based mixing method were done with the Python package SciPy, which applies least-squares minimization to curve-fitting problems [30].

4. Discussion of the Results

For the discussion of the results, we will first compare our results, which were generated with **exciting**, with the ones calculated with VASP (Chapter 4.1). Then, we will investigate the xc functional dependency of $\bar{g}$ and the effect of SOC on the density-based mixing method (Chapter 4.2). In the end, we will try to modify the method by changing the fit function and adjusting the materials set to improve it for all-electron calculations (Chapter 4.3).

4.1 Comparison to VASP

It is interesting to see where the differences between the codes occur. Instead of just comparing the fit for **exciting** with the one for VASP, we will also compare the band gaps E_{gap}, the optimal mixing parameters α_{opt} and the density-based quantities $\bar{g}$. For the comparison, we use the results Marques *et al.* state in their publication [1] and the values of α_{opt} and $\bar{g}$ they provided us. The **exciting** results are considered here without SOC since, in the paper, SOC was not included. Moreover, PbI_2 is not considered in Chapter 4.1 as it was not part of the original material set. All **exciting** calculations are accessible at [2]. For the comparison, we use absolute and relative differences as well as the RMSE as an average. A detailed discussion of the error estimation is given in appendix C.1.

4.1.1 Band Gaps

The band gap results computed by using **exciting** and VASP are given in table 4.1 and are shown in figure 4.1. Already at first sights, one can see that there are rather few differences between the codes. First, this is represented in the RMSE between the **exciting** and VASP results. With values of $\approx 4\%$ for PBE, $\approx 3\%$ for PBE0 and $\approx 2\%$ for HSE06 (see table 4.1) they are all modest. Moreover, the average errors for the three functionals are pretty similar, which means that all three of them are equally well captured by **exciting** and VASP. Second, figure 4.1 shows that the largest discrepancies occur for SiO_2 and LiF with -0.25 eV and -0.13 eV, respectively, which for both is just an insignificant percentage of the experimental value (2.5% and 0.9%). Most importantly, though, the figure shows no material-dependence of the differences. The indirect band gaps coincide similarly well as the direct band gaps, and no material class produces better agreement of the codes than another. Further research of the similarities of multiple DFT codes can be found in reference [31]. The good correspondence between **exciting** and VASP is consistent with the findings of Lejaeghere *et al.*

Comparing the results of the two codes with the experimental band gaps shows much larger differences. On average, the PBE functional is able to reproduce the band gap just with an accuracy of $\approx 50\%$. PBE0 and HSE06, after all, achieve RMSEs of $\approx 30\%$ and $\approx 17\%$, respectively (see last line of table 4.1)[ix]. Here, one can see the clear advance of the hybrid functionals, which

[ix] Also concerning the experimental values, one can see the **exciting** and VASP achieve comparable accuracy as

Table 4.1: Band gaps computed by using **exciting** and VASP in eV (the latter are taken from reference [1]). All results for **exciting** , given here, were calculated without SOC. The penultimate line gives the deviation between the codes in terms of the RMSE (**exciting** − VASP). The last line states the RMSE comparing the results with experimental band gaps taken from reference [1] (theory − experiment).

element	exp. E_{gap} in eV	E_{gap} in eV (PBE)		E_{gap} in eV (PBE0)		E_{gap} in eV (HSE06)	
		VASP	**exciting**	VASP	**exciting**	VASP	**exciting**
Ne	21.70	11.57	11.60	15.14	15.14	14.39	14.34
Ar	14.20	8.65	8.72	11.06	11.14	10.31	10.38
Kr	11.6	7.27	7.29	9.41	9.49	8.67	8.70
Xe	9.8	6.25	6.25	8.1	8.14	7.39	7.38
C	5.48	4.17	4.15	6.06	6.05	5.33	5.29
Si	1.17	0.59	0.57	1.78	1.78	1.16	1.13
Ge	0.74	0.00	0.00	1.31	1.45	0.77	0.79
LiF	14.20	9.24	9.11	12.26	12.17	11.53	11.43
LiCl	9.40	6.41	6.40	8.50	8.55	7.80	7.80
MgO	7.83	4.77	4.75	7.27	7.23	6.53	6.51
SiC	2.40	1.34	1.35	2.95	2.98	2.24	2.22
BN	6.25	4.41	4.47	6.50	6.59	5.75	5.79
GaN	3.20	1.72	1.63	3.64	3.58	2.96	2.92
GaAs	1.52	0.63	0.53	2.09	2.00	1.47	1.42
AlP	2.45	1.58	1.58	2.93	2.96	2.27	2.26
ZnS	3.91	2.11	2.08	4.00	4.01	3.34	3.32
CdS	2.42	1.17	1.14	2.87	2.84	2.23	2.19
AlN	6.28	4.16	4.14	6.25	6.25	5.53	5.49
SiO_2	10.3	6.02	5.81	8.63	8.41	7.89	7.64
MoS_2	1.29	0.87	0.83	2.09	2.03	1.42	1.33
ZnO	3.44	0.90	0.83	3.26	3.27	2.57	2.58
RMSE (**exc.** − VASP)		4.36%		2.58%		2.10%	
RMSE (theory − exp.)		47.31 %	48.37%	29.41%	31.26%	16.91%	17.18%

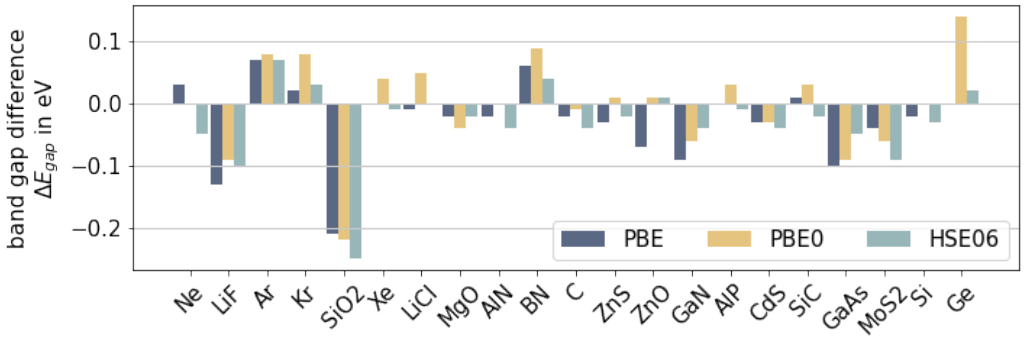

Figure 4.1: Differences between the results calculated with **exciting** and VASP in the band gaps with $\Delta E = E_{\textbf{exciting}} - E_{\text{VASP}}$ in eV. The materials are ordered according to their band gap size (largest to smallest).

achieve results much closer to the experiment. However, taking only the RMSE into account does not determine how differently the functionals behave for the single materials. Therefore, we show the relative difference between the calculation results and the experimental gaps in

they result in similar RMSE values between theory and experiment.

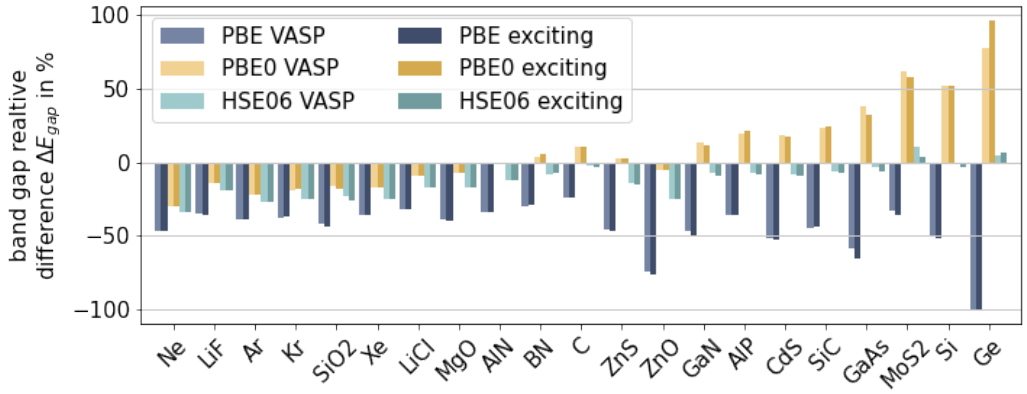

Figure 4.2: Relative differences between the experimental and the calculated band gaps. The dark bars show the results for **exciting**, the light colours resemble the VASP calculations. The materials are sorted according to their band gap size, starting with the largest gaps.

figure 4.2. One can see that PBE systematically underestimates all band gaps, with the highest discrepancy for Ge. For Ge, the PBE calculation is not able to identify the band gap due to its small size and finds this material to be metallic rather than a semiconductor. PBE0, on the other hand, overestimates the band gaps of semiconductors and underestimates the gaps for all the other materials. Therefore, its performance is best for medium-sized band gaps and lacks accuracy for very small and very large band gaps, with a variation of the relative band gap difference between a few up to nearly hundred percent. HSE06, on the contrary, performs best for small band gaps and just slightly worse than PBE0 for large band gaps. This leads, on average, to the best performance. In other words, figure 4.2 makes evident that the hybrid functional achievement is indeed material-dependent.

4.1.2 Optimal Mixing Parameter α_{opt}

The optimal mixing parameters, obtained from the energy gaps with equation (3.27), are listed in table 4.2a and illustrated in figure 4.3. First of all, for both codes, one can notice that the optimal mixing parameter is quite different from the standard value of $\alpha = 0.25$ for most materials. Here, the largest band gaps require the biggest optimal mixing parameters. In particular, for the noble gases, for which the hybrid functionals hugely underestimate the gap, α_{opt} is much larger. According to that it seems reasonable to use a parametrized mixing parameter, which adjusts for each material.

For the two functionals, the comparison of **exciting** and VASP shows marginally differences between the calculated α_{opt}. Especially in figure 4.3, it is evident that the differences between the codes are rather negligible[x], which is confirmed by the average errors of $\approx 4\%$ for PBE0 and $\approx 5\%$ for HSE06 (see table 4.2a last line). The small differences are a consequence of the equally marginal discrepancies between the band gaps described above in Chapter 4.1.1. Therefore, as expected, the RMSEs have a similar magnitude as the average differences between the codes for the energy gaps (see table 4.1 penultimate line).

In figure 4.3, one also notices that HSE06 always demands a larger fraction of non-local exact exchange to reproduce the experimental band gaps. This can be explained through the screening, which is not considered in PBE0. Hence, a smaller fraction of the HF exchange is needed, as also long-range exchange is included in the calculations. This supports the argument by Marques *et al.* [1] that the two functionals require fundamentally different parametrizations.

[x]To make it even clearer, the relative differences between the optimal mixing parameter are also shown in figure C.2.

Table 4.2: Comparison of the quantities α_{opt} and $\bar{g}$ for the two codes. In the last line of each table, the RMSE (**exciting** − VASP) values for the comparison of the codes are given.

(a) Comparison of α_{opt}.

Material element	α_{opt} for PBE0		α_{opt} for HSE06	
	VASP	**exciting**	VASP	**exciting**
Ne	0.71	0.71	0.90	0.92
Ar	0.58	0.57	0.84	0.83
Kr	0.51	0.49	0.77	0.76
Xe	0.48	0.47	0.78	0.79
C	0.17	0.18	0.28	0.29
Si	0.12	0.12	0.25	0.27
Ge	0.14	0.13	0.24	0.23
LiF	0.41	0.42	0.54	0.55
LiCl	0.36	0.35	0.54	0.54
MgO	0.31	0.31	0.43	0.44
SiC	0.16	0.16	0.29	0.30
BN	0.22	0.21	0.34	0.34
GaN	0.19	0.20	0.30	0.30
GaAs	0.15	0.17	0.26	0.28
AlP	0.16	0.16	0.32	0.32
ZnS	0.24	0.24	0.37	0.37
CdS	0.18	0.19	0.29	0.30
AlN	0.25	0.25	0.39	0.40
SiO2	0.41	0.43	0.57	0.61
MoS_2	0.09	0.10	0.19	0.23
ZnO	0.27	0.27	0.38	0.37
RMSE	4.70 %		5.05 %	

(b) Comparison of $\bar{g}$.

Material	$\bar{g}$ in $\sqrt{a_0}$	
	VASP	**exciting**
Ne	1.554	1.474
Ar	1.316	1.312
Kr	1.249	1.268
Xe	1.182	1.214
C	1.117	1.190
Si	0.999	1.048
Ge	1.013	1.147
LiF	1.333	1.366
LiCl	1.157	1.199
MgO	1.169	1.270
SiC	1.051	1.117
BN	1.146	1.211
GaN	1.121	1.245
GaAs	1.060	1.156
AlP	1.022	1.080
ZnS	1.158	1.200
CdS	1.164	1.210
AlN	1.141	1.183
SiO_2	1.299	1.315
MoS_2	1.055	1.133
ZnO	1.273	1.295
RMSE	5.64 %	

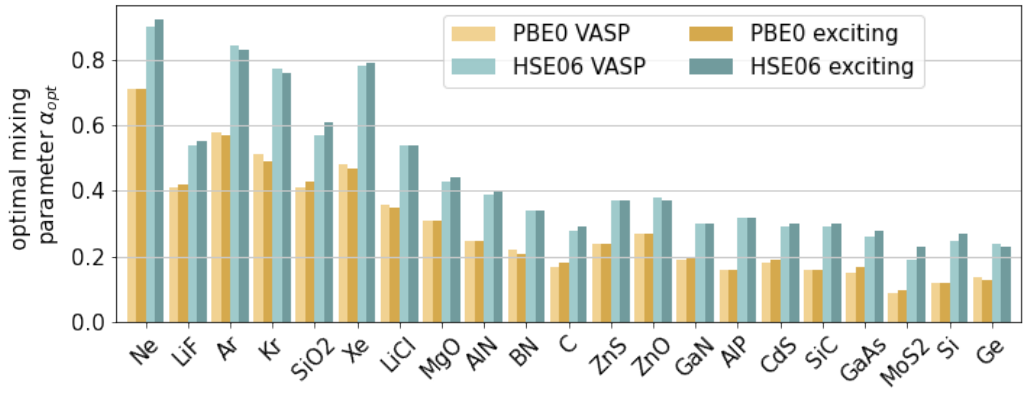

Figure 4.3: α_{opt} calculated with **exciting** (light colours) and VASP (dark colours). The materials are ordered according to their band gap size (from large to small).

4.1.3 Density-Based Quantity $\bar{g}$

The $\bar{g}$ for **exciting** and VASP can be found in table 4.2b and figure 4.4. The average error between the two codes has a value of $\approx 6\%$ (last line of table 4.2b). This is similar to the RMSE of α_{opt}. However, if one compares the differences between the codes with the range the quantity covers, the discrepancies appear larger. Moreover, the discrepancy between the codes

is systematic in $\bar{g}$ and not randomly distributed like it seems to be the case for α_{opt}. We observe that $\bar{g}$ is slightly larger when calculated with **exciting** than when obtained with VASP for nearly all materials (the difference is visible in figure 4.6, and additionally shown in C.3). Ne and Ar are the only exception. These differences between **exciting** and VASP can most likely be attributed to the conceptually different approaches of the codes (refer to Chapter 3)[xi]. In particular, the computation of $\bar{g}$ **exciting** considers the full electron density, whereas VASP includes only the distribution of the valence electrons.

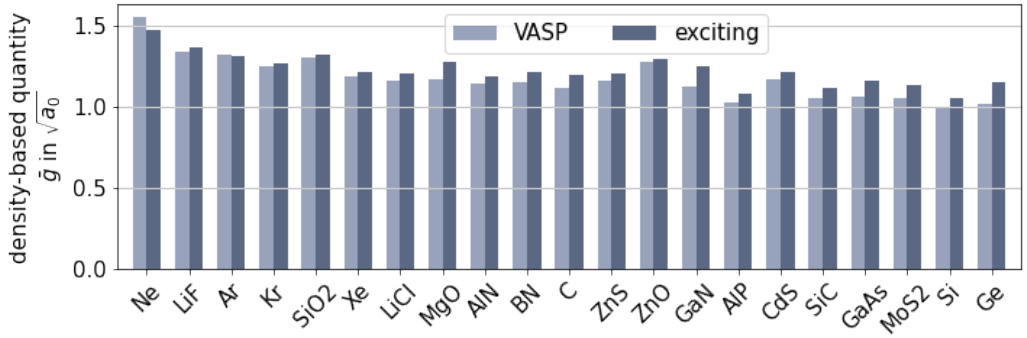

Figure 4.4: $\bar{g}$ calculated with **exciting** and VASP. The materials are ordered according to their band gap size (from large to small).

4.1.4 Density-Based Mixing Method

With the quantities discussed in the previous chapters, we first apply the regression exactly as suggested in reference [1]. This means a linear fit for PBE0 and a single polynomial function with a power $n = 4$ for HSE06. With the same material set as Marques *et al.*, we construct the fits shown in figure 4.5 with the parameters

$$\begin{aligned} \alpha_{\text{PBE0}} &= 1.41\ a_0^{-1/2} \cdot \bar{g} - 1.4 \quad \text{and} \\ \alpha_{\text{HSE06}} &= 0.20\ a_0^{-2} \cdot \bar{g}^4 - 0.01\ . \end{aligned} \tag{4.1}$$

In this figure, also the VASP results are shown. One can see the systematic difference between the $\bar{g}$ values discussed above. Nearly all blue points (**exciting**) are distributed further to the right than the yellow ones (VASP). This changes only for Ne, leading to a crossing of the two fits. Although the relative shift in $\bar{g}$ is in average rather moderate, it leads to quite different results for the fit parameters (compare eq. 4.1 for **exciting** with eq. 2.31 for VASP). For both functionals, the slope a is larger and the absolute shift b is smaller than for VASP. This sensitivity of the parameters to the changes in $\bar{g}$ between the two codes indicates that the method is rather fragile.

Additionally to the fit parameters, also their uncertainties (one standard deviation error) are given in figure 4.5. One can see that they are quite high, allowing only a precision of one or two digits. This underlines what already can be seen in the figure. The data does not perfectly agree with the functions but instead is rather spread around the fits.

Evaluating the fits in figure 4.5 according to the RMSE values, we get $\approx 20\%$ for PBE0_{mix} and $\approx 16\%$ for $\text{HSE06}_{\text{mix}}$. These indicators of how well the functionals can reproduce the experimental energies are smaller than the ones for PBE0 and HSE06 without the mixing method (see last line table 4.1). So, even though the fits do not match the data perfectly and

[xi] As a consequence of these different $\bar{g}$ results, we expect $\bar{g}$ to be also sensitive to change in the basis functions and potentials when just calculated with **exciting**. However, using different species files, i.e. a different number of lo's, for Ne, did not show any influence on $\bar{g}$ (see appendix A.5). It would be interesting to see if this is similar for other materials. Since Ne has only two core electrons in addition to the eight valence electrons, this could be very specific and vary for heavier atomic species.

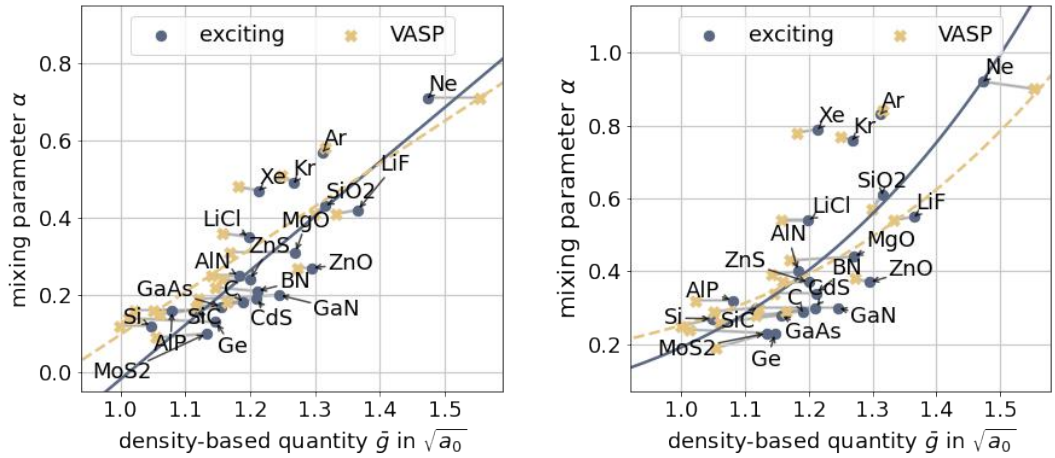

(a) α_{opt} versus $\bar{g}$ for PBE0. The lines show a linear fit function $\alpha_{\text{mix}} = \text{a} \cdot \bar{g} + \text{b}$ with fit parameter for **exciting**: $\text{a} = (1.41 \pm 0.21)\ a_0^{-1/2}$ and $\text{b} = (-1.4 \pm 0.3)$, resulting in an RMSE $= 19.56\%$ compared to experimental results.
The parameters for the VASP fit, $\text{a} = 1.10507\ a_0^{-1/2}$ and $\text{b} = -1.00778$, are taken from reference [1]. The respective mixing achieves an RMSE of 13.86% compared to experimental results.

(b) α_{opt} versus $\bar{g}$ for HSE06. The lines show a single polynomial fit function $\alpha_{\text{HSE06}} = \text{a} \cdot \bar{g}^4 + \text{b}$ with fit parameters for **exciting**: $\text{a} = (0.20 \pm 0.04)\ a_0^{-2}$ and $\text{b} = (-0.01 \pm 0.10)$, resulting in an RMSE $= 16.48\%$ compared to experimental results.
The parameters for the VASP fit, $\text{a} = 0.130711\ a_0^{-2}$ and $\text{b} = 0.121983$, are taken from reference [1]. The respective mixing achieves an RMSE of 9.41% compared to experimental results.

Figure 4.5: Comparison of the density-based mixing method for VASP and **exciting**. As suggested in reference [1], we used a linear fit for PBE0 and a single polynomial function with a power $n = 4$ for HSE06. The difference between the codes is highlighted by a grey line for each material.

produce rather large uncertainties, the band gap results could be improved. For PBE0, the density-dependent mixing makes the functional $\approx 10\%$ better. However, the improvement for HSE06 is just $\approx 1\%$. With such a small improvement it is uncertain whether the band gaps for other materials, which were not included in the material set, and hence, for which the method has not been optimised, are also calculated more accurate.

The density-based mixing methods found with VASP give RMSEs of $\approx 14\%$ for PBE0_{mix} and $\approx 10\%$ for $\text{HSE06}_{\text{mix}}$ (see figure 4.5), which are even better results. In the following analysis, we want to see if one can achieve comparable average errors within the all-electron framework or if this improvement is restricted to pseudo-potential codes. Therefore, in Chapter 4.3, we will try to make the modelling of the optimal mixing parameter better by applying the fit to subsets of the materials and by using different fit functions. Before that, however, some additional investigations are necessary.

4.2 Additional Investigations

In their work [1], Marques *et al.* stated that $\bar{g}$ is functional independent. So before the adaption of the method to **exciting**, we want to verify that $\bar{g}$ does not depend on the xc functional in an all-electron framework as well. Moreover, Marques *et al.* did not include SOC in their calculations, which is why it is interesting to see how SOC influences the regression and the applicability of the method.

4.2.1 Dependence on the Exchange-Correlation Functional

If $\bar{g}$ does not depend on the xc functional, the quantity could be computed from calculations carried out with the computationally cheap PBE functional. Moreover, it would not require to be updated self-consistently in the hybrid SCF (compare Chapter 3.1.2). The functional independence, however, is not trivial since the density itself depends on the used xc functional. Therefore, in this work, we want to verify specifically that also for **`exciting`**, $\bar{g}$ does not strongly depend on the functional used to determine the density, in other words, leads to the same results when calculated with PBE or a hybrid functional.

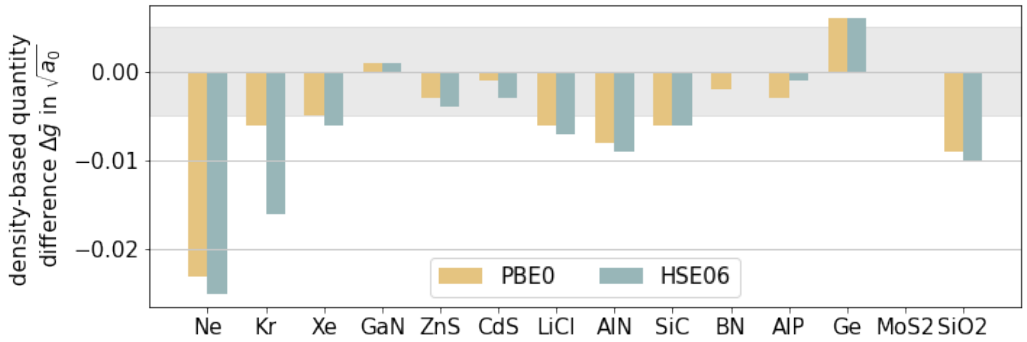

Figure 4.6: Exchange-correlation functional dependence of $\bar{g}$. For the materials explicitly calculated in this thesis (compare table 3.1), we compute $\bar{g}$ also with PBE0 and HSE06. Here the differences between the PBE results and the hybrid functional results $\Delta\bar{g} = \bar{g}_{\text{PBE}} - \bar{g}_{\text{hyb}}$ are shown. In grey, the convergence criterion of the numerical calculations ($\pm 0.005\ \sqrt{a_0}$) is highlighted (see Chapter 3.3.3).

The differences between the PBE0 and HSE06 results and the $\bar{g}$ values computed by PBE are shown in figure 4.6 (additionally, the exact values are given in table C.2). Here, we investigate only the materials that were explicitly computed in this thesis. From these results, we observe that, for some materials, there is a significant difference, but for the majority of materials, $\bar{g}$ is resembled with an error comparable to the convergence criterion of $(\pm 0.005\ \sqrt{a_0})$, that we defined in Chapter 3.3.3. In other words, the error has the same magnitude as the precision we obtain numerically, and therefore, is negligible.

Only for Ne and Kr (with HSE06), the difference $\Delta\bar{g}$ is visibly larger than for the other materials. These two noble gases have very localized electrons, and their atoms are connected through long-range van der Waals interaction, which is a correlation effect. Since HF theory neglects correlation, using the hybrid functionals instead of PBE has a major effect on the electron density. For Xe, however, this effect is not visible, which could be explained by Xe having the smallest gap of the noble gases, and therefore, the smallest correction between PBE and the hybrid functionals.

Nearly for all materials, $\bar{g}_{\text{hyb}}$ is larger than $\bar{g}_{\text{PBE}}$, making the difference negative. However, it is complicated to find a clear reson for that. Due to the integral over the unit cell and the quotient of the gradient and the density, the relation between n and $\bar{g}$ is rather complex. Hence, it is difficult to estimate how the use of hybrid functionals, and therefore, the inclusion of non-local effects, for the calculation of n leads to a larger $\bar{g}$. Ge, with a smaller $\bar{g}_{\text{hyb}}$, is the only exception. As mentioned before, Ge is evaluated as a metal by the PBE functional due to its very small band gap (see table 4.1). Consequently, the electron density is qualitatively different, which could be the reason for the positive $\Delta\bar{g}$.

Both hybrid functionals produce rather similar differences to the PBE results. The discrepancy between them is mostly much smaller than the convergence criterion of $\pm 0.005\sqrt{a_0}$. Again, there is one exception. For Kr, $\bar{g}_{\text{PBE}}$ and $\bar{g}_{\text{PBE0}}$ coincide well, whereas the difference to $\bar{g}_{\text{HSE06}}$ is approximately three times larger than the convergence criterion. Overall, we can see the tendency that the difference $\Delta\bar{g}$ is larger for HSE06 than for PBE0, which at first thought seems

counter-intuitive as the HSE06 excludes long-range interaction , and therefore, should be nearer to the semi-local PBE functional. It is not clear why this is otherwise.

The $\bar{g}$ values for the different functionals coincide well, with an average difference between the hybrid $\bar{g}$ and the PBE $\bar{g}$ of around $-0.005\sqrt{a_0}$ for both hybrid functionals ($-0.005\sqrt{a_0}$ for PBE0 and $-0.006\sqrt{a_0}$ for HSE06, see table C.2). So, in general, $\bar{g}$ does not depend strongly on the xc functional. Consequently, in the following calculations, we will continue to use $\bar{g}$ computed by PBE.

4.2.2 Effects of Spin-Orbit Coupling

SOC changes the value of the energy gap and causes degenerate states to emerge. Since the optimal mixing parameter directly depends on the band gap results, including SOC in the calculations also corrects the value of α_{opt}. Only for heavy elements, i.e. elements with many electrons, SOC has a comprehensive effect. Hence, for our material set, we investigate SOC only for Kr, Xe, GaN, ZnS, CdS and MoS_2. For GaN, ZnS and MoS_2[xii], no difference above 0.02 eV (which is the convergence criterion of the gap, see chapter 3.3.2) in the band gap due to SOC is found. Also, for CdS, the effect is rather small. Since SOC has a tangible effect only upon a few materials, we additionally investigate PbI_2, which is known to have a significant SOC correction due to its heavy components. The band gaps for those materials are shown in table 4.3. One can identify that SOC reduces the gap for all of them (an example of the band gap reduction is shown in figure A.5). As expected, the energy gap correction for PbI_2 is the largest with $\Delta E_{\text{gap}}^{\text{SOC}} \approx 0.6$eV, followed by Xe with $\Delta E_{\text{gap}}^{\text{SOC}} \approx 0.4$eV.

Table 4.3: Influence of SOC on band gaps and the optimal mixing parameter. For the four materials, the band gaps for PBE, PBE0 and HSE06 are given without and with SOC correction in eV as well as the respective optimal mixing parameters. The last row states $\bar{g}$ computed by PBE.

material	exp.	PBE	PBE0		HSE06		PBE
	E_{gap} in eV	E_{gap} in eV	E_{gap} in eV	α_{opt}	E_{gap} in eV	α_{opt}	$\bar{g}$ in $\sqrt{a_0}$
Kr	11.6	7.29	9.49	0.49	8.70	0.76	1.268
SOC		7.07	9.27	0.51	8.48	0.80	1.271
Xe	9.80	6.25	8.14	0.47	7.38	0.79	1.214
SOC		5.82	7.73	0.52	6.97	0.87	1.212
CdS	2.42	1.14	2.84	0.19	2.19	0.30	1.210
SOC		1.12	2.82	0.19	2.18	0.31	
PbI_2	2.55	2.20	3.54	0.07	2.89	0.13	1.165
SOC		1.51	2.92	0.18	2.25	0.35	—

Due to the decrease of the calculated band gap, a larger amount of HF exchange is needed to reproduce the experimental gap. Hence, the optimal mixing parameter α_{opt} increases when SOC is included in the calculation. Those values are given in table 4.3 as well. With that, we can compare the influence of SOC on the band gap with its impact on α_{opt}. For all four materials, the relative difference caused by SOC is larger for the mixing parameter than for the band gap. For example, the gap correction for Xe is around $5-7\%$ for all three functionals, whereas the adjusting of α_{opt} is $\approx 10\%$. This effect is even more significant for PbI_2. Here, the band gap correction produces a relative shift of $\approx 20\%$, whereas the caused relative shift in α_{opt} is above 150% (157% for PBE0 and 169% for HSE06). So the SOC correction is even more relevant for α_{opt} than for the band gaps. Hence, in the regression, which defines the density-based mixing method, the results with SOC should be used.

Furthermore, we calculate $\bar{g}$ with and without SOC. The respective values are also given in

[xii] For MoS_2 we can not find an influence of SOC on the band gap. This, however, could be a result of the computational method. For further explanations, see the comment in table B.1.

table 4.3. Although the electron density is affected by the SOC correction, our results show that $\bar{g}$ does not vary under SOC.

The comparison of the $(\bar{g}, \alpha_{\text{opt}})$ points with and without SOC can be seen in figure 4.7. The horizontal shift for the four materials is rather small for Kr and CdS but significant for Xe and PbI_2. For Xe and Kr, the increase of α_{opt} leads to a worse agreement with the fits. For PbI_2, which has strong SOC, we see that, by including SOC, the point gets closer to the cluster of the other materials. Without SOC, PbI_2 is a separated point with an unreasonable small α_{opt}. This material leads us to conclude that α_{mix} gives the mixing parameter for the energy gap with SOC included, as the point with SOC is so much closer to the fit. Hence, α_{mix} should be used with SOC. However, to verify this properly more materials with a large SOC correction need to be studied.

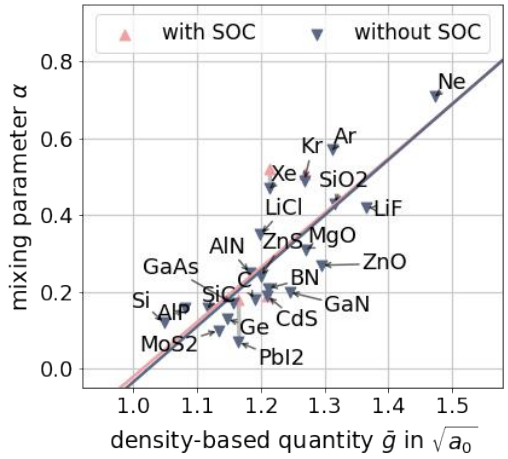

(a) α_{opt} versus $\bar{g}$. Fit with a linear fit function $\alpha_{\text{mix}} = \text{a} \cdot \bar{g} + \text{b}$. The fit parameters with SOC are $\text{a} = (1.42 \pm 0.22)\ a_0^{-1/2}$ and $\text{b} = (-1.4 \pm 0.3)$, resulting in RMSE $= 19.55\%$ compared to experimental results. The fit parameters without SOC are $\text{a} = (1.44 \pm 0.22)\ a_0^{-1/2}$ and $\text{b} = (-1.5 \pm 0.3)$, resulting in RMSE $= 19.32\%$ compared to experimental results.

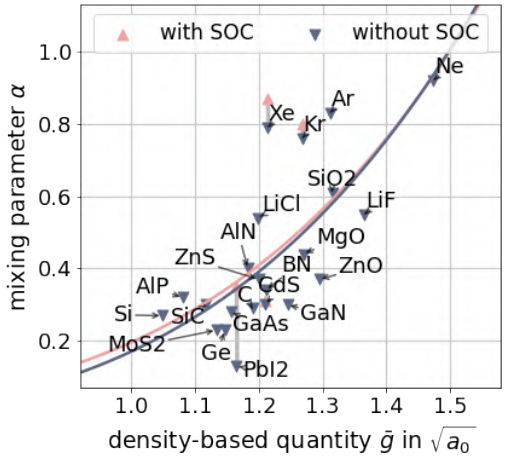

(b) α_{opt} versus $\bar{g}$. Fit with a single polynomial function $\alpha_{\text{HSE06}} = \text{a} \cdot \bar{g}^4 + \text{b}$. The fit parameters with SOC are $\text{a} = (0.20 \pm 0.04)\ a_0^{-2}$ and $\text{b} = (-0.00 \pm 0.11)$, resulting in RMSE $= 16.96\%$ compared to experimental results. The fit parameters without SOC are $\text{a} = (0.21 \pm 0.04)\ a_0^{-2}$ and $\text{b} = (-0.03 \pm 0.19)$, resulting in RMSE $= 15.74\%$ compared to experimental results.

Figure 4.7: Comparison of the density-based mixing method without the SOC correction and with SOC included. To better show the influence of SOC, horizontal lines between the results of SOC (rose) and no SOC (blue) are shown for each material.

Additionally, one notices that the influence of SOC on the fit is rather small – much smaller than the uncertainties of the fit parameters. For our specific material set, including SOC does not lead to a notable change of the fit. This is caused by the simple fact that only a few materials were significantly influenced by SOC. Also, the RMSE values for the two fits are very much alike (see figure 4.7). Nevertheless, for all following calculations, we use the SOC corrected data because it better reflects the physics.

4.3 Improvement of the Method

To make the density-based mixing method better applicable to all-electron calculations, it can be further improved. First, we change the material set on which the fit is evaluated, and secondly, try other fit functions.

4.3.1 Reduced Material Sets

As discussed in Chapter 3.3.1, the material set can be divided into several groups. For doing so, we use the material classification introduced by Koller *et al.* [3], and therefore, divide the materials into semiconductors, transition metals and ionic compounds. This division is shown in figure 4.8 and also in the appendix (figure B.1 displays only the materials without additional fit lines).

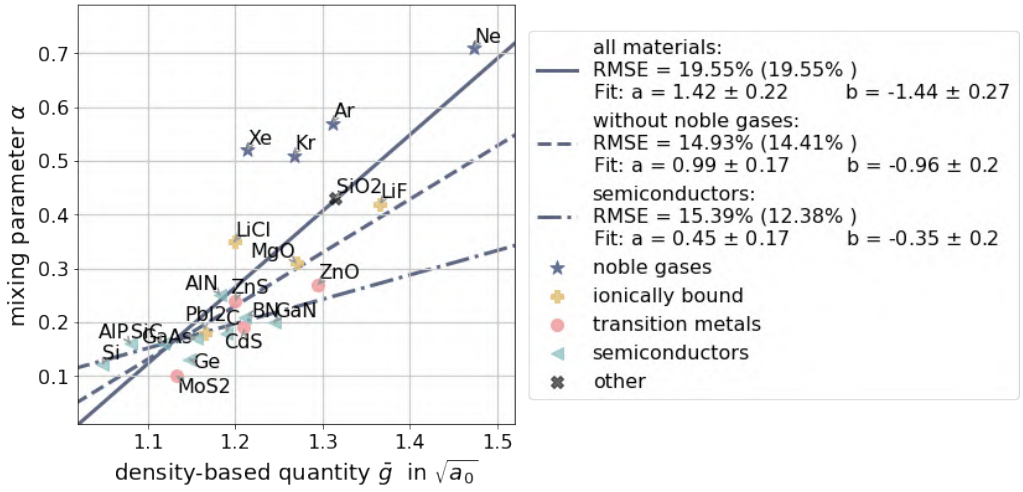

(a) Optimal mixing parameter α_{opt} for PBE0 and a linear fit function $\alpha_{\text{mix}} = \text{a} \cdot \bar{g} + \text{b}$.

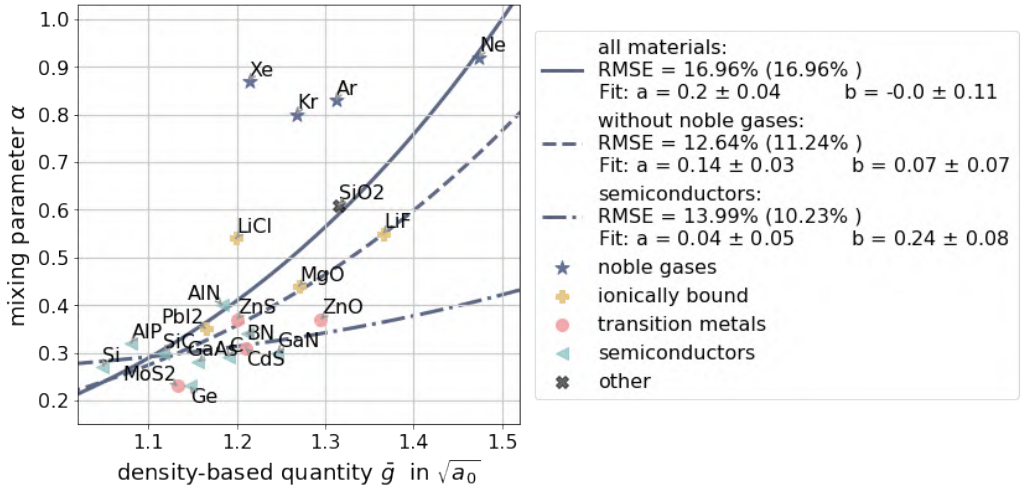

(b) Optimal mixing parameter α_{opt} for HSE06 and a single polynomial fit function $\alpha_{\text{HSE06}} = \text{a} \cdot \bar{g}^4 + \text{b}$.

Figure 4.8: Optimal mixing parameter α_{opt} for (a) PBE0 and (b) HSE06. The complete material set can be divided into noble gases (plus), transition metal compounds (filled cycle), semiconductors (triangle), ionically bound compounds (star), and other samples (cross) based on the classification by Koller *et al.* [3]. Additionally, the results of the regression for the density-based mixing method is shown for different material sets: for all materials (solid line), subsets with noble gases excluded (dashed line) and only semiconductors (dash-dotted line). Here the linear fit is used for PBE0_{mix} (a) and the power of 4 for $\text{HSE06}_{\text{mix}}$ (b) as suggested by Marques *et al.*. In the legends, the RMSE between the calculated and experimental band gaps for all materials are given. Also, the RMSE concerning only the materials included in the fit is stated in parenthesis, and the fit parameters with their uncertainties (of one standard derivation error) are given.

The separation makes it easy to notice that the noble gases seem not very suitable for the density-based mixing method. Their points disagree with the relation between α_{opt} and $\bar{g}$ the other materials predict. The linear and polynomial fits for PBE0 and HSE06, respectively, do not model those materials very well. Especially for HSE06 with SOC, the noble gases lie outside an acceptable range around the fit. Additional to the group of noble gases, also the ionically bound materials seem to build their own group. Nevertheless, they lie closer to the cluster of other materials than the noble gases. Contrarily, the transition metals and semiconductors are not separable as they are spread in a similar region [xiii]. For this reason, and because some of the material classes consist only of a few samples, we do not compute a fit for every single material class.

Instead, in figure 4.8, we compare the fits for the whole material set with a subset, in which the noble gases are excluded as they have the largest discrepancies. We also provide a fit for the semiconductors purely, as they built the majority of materials in the set and the majority of materials for which hybrid functionals are applied. For these subsets, the parametrization functions as suggested by Marques *et al.* are used, i.e. a linear function for PBE0 and a single polynomial function with the power of 4 for HSE06. There is an evident difference between the three fits for the two hybrid functionals in figure 4.8. The fits for all materials lie naturally higher than the other two as they include the noble gases. Contrarily, the slopes of the semiconductor fits are much smaller than the other slopes. The fits for the subset without noble gases lie in the middle between the other two fits, leading to good description of most materials. These differences imply that the density-based mixing method depends strongly on the material set.

There are two possibilities to evaluate fits, which are based on a reduced material set. We can use the fit to predict either the gaps of the materials included in the subset or the band gaps of all materials. In both cases, the predicted energies are compared with the experimental ones. The first approach emphasizes how good the fit is optimized for the subset. Whereas the second approach also considers how suitable the fit is for materials that were not included. As the density-based mixing method should be usable for a large range of materials, we will focus here on the latter value. However, both estimations are given in figure 4.8. Notably, we see that, for the two functionals, excluding the noble gases leads to a clear improvement of the method. For PBE0_{mix}, the RMSE (with respect to all materials) decreases from $\approx 20\%$ to $\approx 15\%$ and for $\text{HSE06}_{\text{mix}}$, from $\approx 17\%$ to $\approx 13\%$.

The fits for semiconductor materials, have a larger RMSE for the two functionals if we compare the methods with respect to all materials. This could be expected as the fits are evaluated for a lot of materials that were not included in the regression. However, if we compare the predicted results only with the experimental band gaps of semiconductors, the reproduction is significantly better. For PBE0_{mix}, one gets an RMSE of $\approx 12\%$, and for $\text{HSE06}_{\text{mix}}$, an RMSE of $\approx 10\%$. So applied to semiconductors only, the method works remarkably well[xiv]. Nonetheless, we want to find a density-based mixing method that is applicable for all kinds of materials.

4.3.2 Other Fit Functions

Excluding the noble gases from the material set improves the density-based mixing method. However, figure 4.8 suggests that an advance in the description of all data points is still needed. In the following, we want to test whether another fit function can improve the parametrization

[xiii] This is comparable to the results of Koller *et al.* reference [3, fig. 4], where the TmX overlap with the semiconductors and ionically bound materials are separated, although they are using a different $\bar{g}$ (see Chapter 2.6).

[xiv] The initial RMSEs for pure PBE, PBE0 and HSE06 evaluated only for semiconductors are 52.72%, 39.75% and 7.59% (with **`exciting`**). The result for PBE is comparable with the one of the whole set, given in table 4.1. However, for PBE0, the RMSE for the semiconductor subset is significantly higher. This agrees with the fact that PBE0 overestimates small gaps by far. Thus, the improvement through the density-based mixing method is even more remarkable (from $\approx 40\%$ to $\approx 12\%$). For HSE06, on the contrary, the reproduction of the experimental values is better with a constant $\alpha = 0.25$ (since 7.59% is smaller than 10.23%).

even further. Therefore, we use a generalized formulation of the method

$$\alpha_{\text{mix}} = \mathrm{a} \cdot \bar{g}^n + \mathrm{b}, \tag{2.30}$$

with n as a free fit parameter. Figure 4.9 shows the results for the whole material set, the subset without noble gases and purely semiconductors. We can see that the values of the power n are quite different for the different material sets. For the all-material fit, the least-square optimization of the fitting finds $n \approx 3$ to be the best fit parameter for both functionals (fig. 4.9a and 4.9d). Contrarily, for the fit without noble gases, the power for the two functionals is

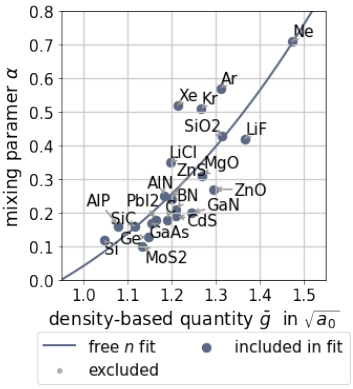

(a) Fit for PBE0 and all materials. Fit parameters: $\mathrm{a} = (0.3 \pm 0.4)\ a_0^{-3/2}$, $\mathrm{b} = (-0.2 \pm 0.5)$ and $n = (3 \pm 3)$ leading to an RMSE of 18.09%.

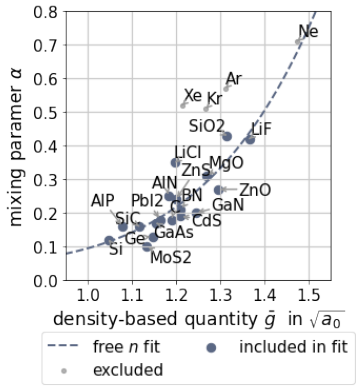

(b) Fit for PBE0 and all materials except noble gases. Fit parameters: $\mathrm{a} = (0.06 \pm 0.09)\ a_0^{-3}$, $\mathrm{b} = (0.04 \pm 0.14)$ and $n = (6 \pm 4)$ leading to an RMSE of 13.32% (12.64%).

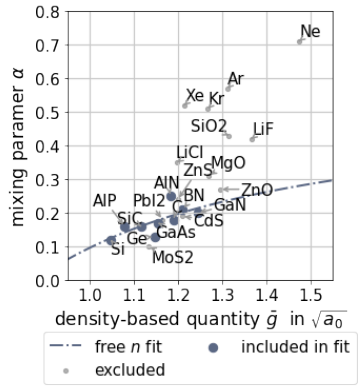

(c) Fit for PBE0 and only semiconductors. Fit parameters: $\mathrm{a} = (0 \pm 3)\ a_0$, $\mathrm{b} = (0 \pm 3)$ and $n = (-2 \pm 20)$ leading to an RMSE of 16.09% (12.84%).

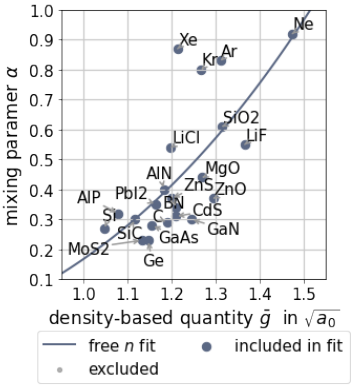

(d) Fit for HSE06 based on all materials. Fit parameters: $\mathrm{a} = (0.3 \pm 0.8)\ a_0^{-3/2}$, $\mathrm{b} = (-0.2 \pm 1.0)$ and $n = (3 \pm 4)$ leading to an RMSE of 17.18%.

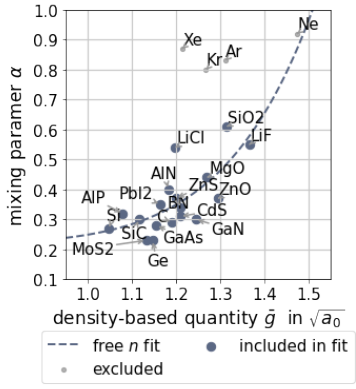

(e) Fit for HSE06 and all materials except noble gases. Fit parameters: $\mathrm{a} = (0.03 \pm 0.07)\ a_0^{-4}$, $\mathrm{b} = (0.22 \pm 0.14)$ and $n = (8 \pm 7)$ leading to an RMSE of 12.22% (10.83%).

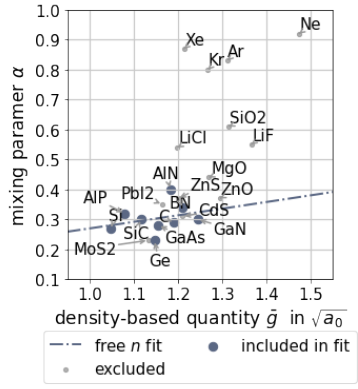

(f) Fit for HSE06 and only semiconductors. Fit parameters: $\mathrm{a} = (0 \pm 10)\ a_0^{-1/2}$, $\mathrm{b} = (0 \pm 10)$ and $n = (1 \pm 50)$ leading to an RMSE of 14.32% (10.36%).

Figure 4.9: Density-based mixing method with variable power n in the fit. For the complete material set (left), the subset without noble gases (middle) and semiconductors only (right), a single polynomial fit $\alpha_{\text{mix}} = \mathrm{a} \cdot \bar{g}^n + \mathrm{b}$ was done with n as a free fit parameter. The fit parameters and RMSE values of the method are given in the caption of each figure. Here the first RMSE value is calculated in respect to the complete material set and the one in parenthesis in respect to the subset. The excluded materials are shown in each figure as well, but with smaller and grey symbols.

higher ($n \approx 6$ for PBE0 and $n \approx 8$ for HSE06). It is interesting to see that the fits without noble gases have a stronger curvature, and thus, can align better with the cluster of materials (fig. 4.9b and 4.9e). For the semiconductors, the found n is smaller than for the other fits. For the semiconductors the parametrization of $PBE0_{mix}$ has a negative power, leading to a convex curve (fig. 4.9c), whereas, for $HSE06_{mix}$, a linear dependence is determined (fig. 4.9f). In contrast to what was suggested by Marques *et al.*, for our data, there is no significant difference in n between the fits for $PBE0_{mix}$ and $HSE06_{mix}$. This, however, indicates that the physics is not represented accurately by the method as the screening is included fundamentally different in the two functionals.

The uncertainties of the fit parameters a and b are similar to the previous fits (with a fixed n) for the all-material fits and the subset without noble gases. However, for the semiconductor fits, a and b are too close to zero and the uncertainties too large to trust the results. Moreover, for all material sets the uncertainties of n are too large compared to their values. Especially for the semiconductor fits, the results become untrustworthy. Therefore, we use another approach to investigate which power gives the best representation of the experimental gaps. For fixed integer n between 1 and 20[xv], we perform a fit for each material set and functional. To determine the value of n that best represents our data, we search for the power n that gives the smallest RMSE (with respect to the material subset). We choose to use the RMSE of the subset to make it comparable to the first approach, where the fit was adjusted for the $(\alpha_{\mathrm{opt}}, \bar{g})$ data of the subset only. These RMSE values (with respect to the subset) for all fits are shown in figure 4.10. In general, we can see, that the RMSE values for the all-material fits are significantly higher for all powers n. Also, the fits for the subset without noble gases produce larger RMSE values (with respect to the subset) than the semiconductor fits. The difference, however, is not as large. Moreover, for all three material sets, $PBE0_{mix}$ produces higher RMSE than $HSE06_{mix}$, which is plausible as the standard HSE06 is already significantly better than the standard PBE0.

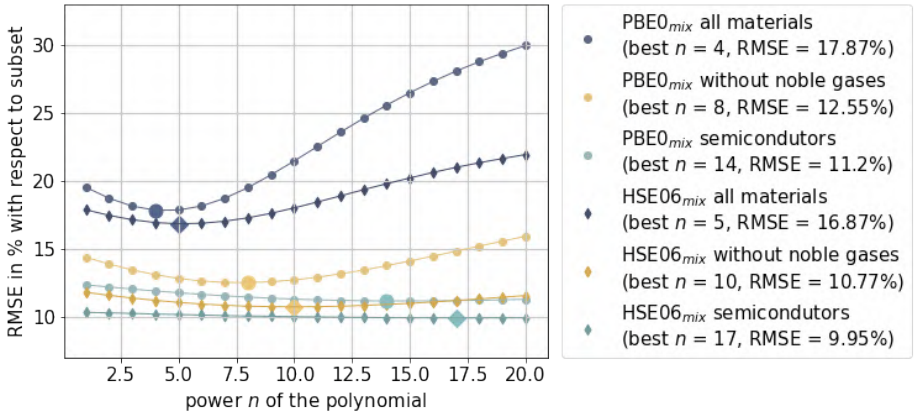

Figure 4.10: RMSE values of the density-based mixing methods with respect to the power n. The RMSE were calculated for the three material sets: all samples (blue), noble gases excluded (yellow) and semiconductors only (green). The circle show the results for $PBE0_{mix}$ and the rhombuses for $HSE06_{mix}$. The computation was only done for integer values of n. The lines between them are meant as a guide to the eye. The larger symbols denote the minimal RMSE values for each line.

In figure 4.10, the smallest RMSE values are highlighted with larger symbols, and the respective results are given in the legend (their corresponding fits are shown in figure C.4). The minimal RMSE approach finds the powers $n = 4$ and $n = 5$ to work best for the set of all materials, whereas $n = 8$ and $n = 10$ are appropriate for the subset without noble gases (for PBE0 and HSE06, respectively). Again, we find that the set without noble gases requires a higher power

[xv] Such a high power was investigated to make sure we have found a clear minimum for the RMSE. As shown in figure 4.10, the minimal RMSE value occurs for a relatively large n.

n than the all-material fit. For semiconductors, this analysis finds $n = 14$ and $n = 17$ to reproduce the band gaps best, which is very different from the powers obtained with the free n fits (compare $n = -2$ in fig. 4.9c and $n = 1$ in fig. 4.9f). Also, for the other two material sets, the best n are different to the obtained n values above with the free n fit but not as significant as for the semiconductor fits. Although we can clearly identify the n that characterises the best fit here, it should be noted that the other RMSE values for the powers around the minimum points are not significantly larger. Especially for the semiconductor subset, the curve in figure 4.10 is rather horizontal. So, also this method produces an uncertainty in n.

Comparing the RMSE values of these fits with the best n shows that the fits for semiconductors achieve the best results. However, the RMSE taken into account considers only the experimental gaps of the subset. To evaluate the full performance of the fits found, one can analyse the band gap results for each material. In figure 4.11, the calculated energy gaps of all three fits and both functionals are compared to the standard hybrid functionals. The bars represent the magnitude of the relative differences between the experimental and theoretical gaps. In general, one realises that the accuracy of the band gap results is still material dependent.

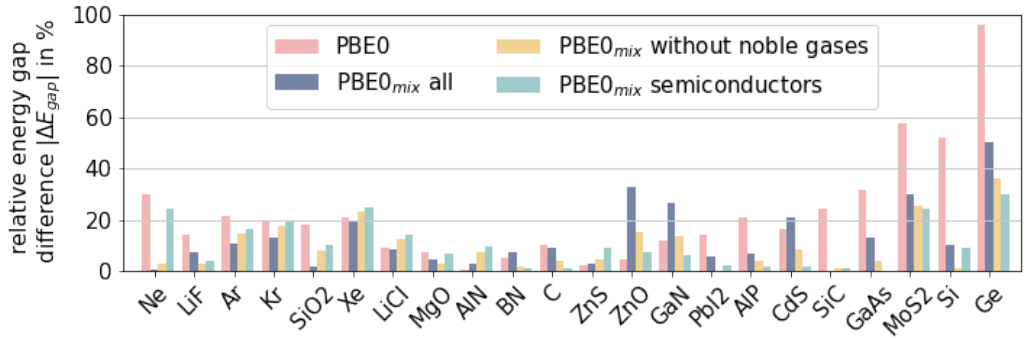

(a) Relative band gap differences between the calculated and experimental results for PBE0 and $PBE0_{mix}$.

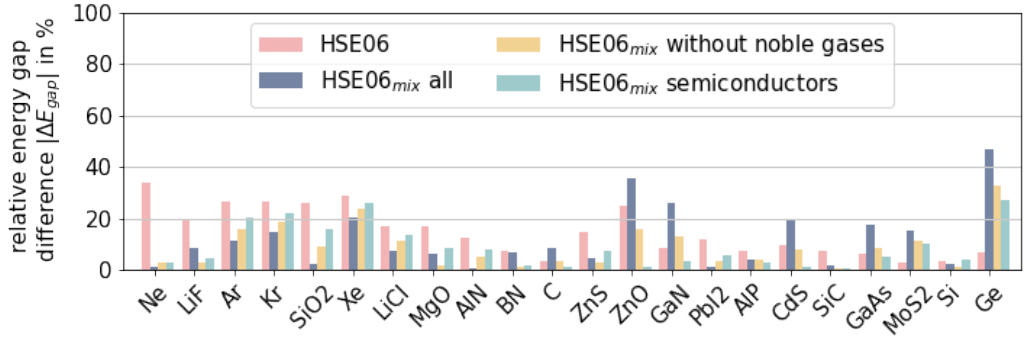

(b) Relative band gap differences between the calculated and experimental results for HSE06 and $HSE06_{mix}$.

Figure 4.11: Band gap differences between experimental values and those obtained by hybrid functional calculations as well as the mixing method E_{mix}. Compared are the fit for the complete material set (yellow), the fit for the subset without noble gases (green) and the semiconductor fit (rose), as well as the pure hybrid functional (blue).

For PBE0, we first of all notice that all three mixing methods can improve the band gap results for the smallest and largest band gaps. For most of the small band gaps (right side of figure 4.11a), the semiconductor fit works best, whereas large band gaps are best represented by the fit for all materials. The latter, however, is noticeably less accurate for medium-sized and small gaps in comparison to the other two mixing parametrizations. The fit without noble gases

builds a compromise between the other two PBE0_{mix} fits. As the final method should work equally well for large and small band gaps, the fit based on the subset without noble gases is considered the best fit. The respective density-based mixing method can be written as

$$\alpha_{\text{PBE0}} = 0.03\ a_0^{-4} \cdot \bar{g}^8 + 0.08\ . \tag{4.2}$$

For HSE06, all density-based parametrizations can improve the band gap results for large band gaps (left side figure 4.11b). For the smallest band gaps, however, the standard HSE06 works best. Especially the fit for all materials leads to significantly worse results for smaller band gaps. Nevertheless, it also creates the smallest discrepancies for large band gaps. Contrarily, the mixing method based on the semiconductors is the best fit for small band gaps and the worst for large. Again, the fit for the subset without noble gases is a compromise. Hence, also here, our fit of choice is based on the subset without noble gases, which results in

$$\alpha_{\text{HSE06}} = 0.015\ a_0^{-5} \cdot \bar{g}^{10} + 0.25\ . \tag{4.3}$$

To sum up, the fits without noble gases give the most balanced improvement for both functionals. As we want the density-based method to be applicable to a majority of materials that are not included in the fit, these are the best options. The respective fits are shown in figure 4.12.

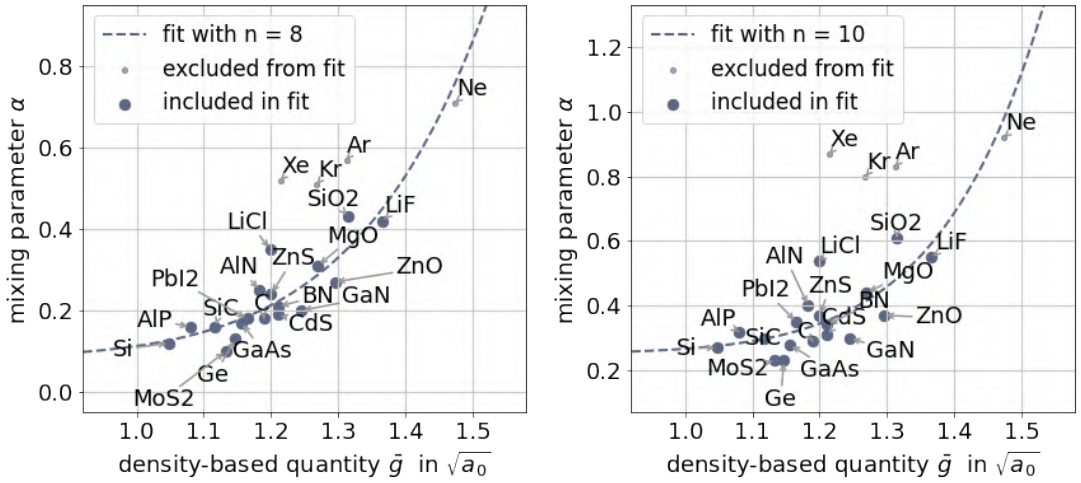

(a) Fit for PBE0 based on the material set without noble gases with a power $n = 8$. The fit parameters are $\text{a} = (0.030 \pm 0.005)\ a_0^{-4}$ and $\text{b} = (0.08 \pm 0.03)$. This PBE0_{mix} achieves an RMSE of 13.30% (12.55%).

(b) Fit for HSE06 based on the material set without noble gases with a power $n = 10$. The fit parameters are $\text{a} = (0.015 \pm 0.004)\ a_0^{-5}$ and $\text{b} = (0.25 \pm 0.03)$. This $\text{HSE06}_{\text{mix}}$ achieves an RMSE of 12.23% (10.77%).

Figure 4.12: Best density-based mixing method found for **`exciting`**. use the same range as before

Furthermore, we tested other elemental functions for the parametrization. Those, however, do not lead to an improvement of the RMSE values, which are compared in the appendix in figure C.5. Nevertheless, also for these parametrizations, excluding the noble gases from the material set leads to better results.

4.4 Evaluation

All fits found in the steps of the previous chapters are summarised in table 4.4 for an overview. Starting from the constant mixing parameter $\alpha = 0.25$, the density-based mixing method, as suggested in [1], is able to improve the reproduction of experimental band gaps. The reduction of the RMSE for PBE0 is significant, whereas, for HSE06, only a slight improvement can be

achieved. A further advance is possible by reducing the material set used for the fit and by changing the fit function. For **exciting**, the fits without noble gases as well as $n = 8$ and $n = 10$ for PBE0 and HSE06, respectively, were the best choices. The final parametrizations for **exciting**, equations (4.2) and (4.3), reproduce the experimental band gaps of the complete material set with an RMSE of $\approx 13\%$ and $\approx 12\%$ for PBE0_{mix} and $\text{HSE06}_{\text{mix}}$, respectively, i.e., these best parametrizations are able to outperform the standard functionals.

In general, the improvement through the best fit is not as significant for $\text{HSE06}_{\text{mix}}$ as for PBE0_{mix}. This could be due to the fact that the screening in HSE06 is not only determined by the mixing parameter α but also by the screening parameter ω (compare chapter 2.5). Hence, to parametrize α for HSE06 might not be as impactful as it is for PBE0. Moreover, HSE06 achieves good results already without the parametrization especially for small gap materials. Although the accuracy of the band gaps is considerably improved with the best fit for $\text{HSE06}_{\text{mix}}$, it is still questionable if the advance is likewise noticeable for other materials.

In table 4.4, also the RMSE values found by Marques *et al.* are given (last two lines). As already discussed in Chapter 4.1.1, the hybrid functionals with constant mixing parameter α perform similarly for the two codes. For PBE0_{mix}, we find comparable improvement of the band gaps through the best density-based mixing methods for **exciting**. Hence, we conclude that the advance is not exclusively achievable with pseudo-potential codes. For $\text{HSE06}_{\text{mix}}$, however, the improvement gained with VASP is significantly better. This means the lack of progress we find is not necessarily occurring. It is more likely that our approach to optimize the fit (by minimizing the RMSE value) fails to find the best parametrization for HSE06. This was already indicated by the fact that we find similar powers n for the regression, which does not resemble the fundamental different concepts of the functionals. Hence, we can conclude that the parametrization should not be entirely deterministic. Instead, the choice of parametrization function should take first principles argumentation into account.

Additionally, one can notice that the final RMSE values in table 4.4 are close to a limit of accuracy, Marques *et al.* identified. They expect the RMSE values not to be smaller than $5 - 10\%$ due to several effects included in the experimental values. For one, zero-point vibration is not included in the DFT calculations. It is usually a relatively small correction up to a few tenths of an eV [1]. However, for some materials like MoS_2, large band gap correction can occur [4]. Moreover, often, reported experimental values are optical gaps, and therefore, include excitonic binding energies. These range from a few meV up to 0.5 eV for certain materials [1]. Additionally, strong polaronic effects can be expected for some ionic materials like LiF, for which this effect is as large as 2 eV [1]. To include all of these effects, a separate treatment of every material could be employed by defining uncertainties of the experimental data. This would lead to a different weighting of α_{opt} in the fit. Alternatively, these effects could be subtracted from the experimental gaps (like Pela *et al.* subtracted the zero-point vibration in reference [32]).

Table 4.4: Comparison of the best fits. For each step of improvement, the fit function and the underlying material set are given. Moreover, the RMSE values with respect to all materials are stated. The first four rows show our results, the last two the results calculated with VASP by Marques *et al.* [1].

(a) For PBE0.

function	materials	RMSE
$\alpha = 0.25$	all	31.26%
$\alpha_{\text{mix}} = \text{a} \cdot \bar{g} + \text{b}$	all	19.56%
$\alpha_{\text{mix}} = \text{a} \cdot \bar{g} + \text{b}$	without noble gases	14.93%
$\alpha_{\text{mix}} = \text{a} \cdot \bar{g}^8 + \text{b}$	without noble gases	13.30%
$\alpha = 0.25$	all	29.41%
$\alpha_{\text{mix}} = \text{a} \cdot \bar{g} + \text{b}$	all	13.86%

(b) HSE06

function	materials	RMSE
$\alpha = 0.25$	all	17.18%
$\alpha_{\text{mix}} = \text{a} \cdot \bar{g}^4 + \text{b}$	all	16.48%
$\alpha_{\text{mix}} = \text{a} \cdot \bar{g}^4 + \text{b}$	without noble gases	12.64%
$\alpha_{\text{mix}} = \text{a} \cdot \bar{g}^{10} + \text{b}$	without noble gases	12.23%
$\alpha = 0.25$	all	16.91%
$\alpha_{\text{mix}} = \text{a} \cdot \bar{g}^4 + \text{b}$	all	9.41%

5. Summary and Outlook

The standard hybrid functionals, PBE0 and HSE06, are able to reproduce experimental energy gaps better than local and semi-local DFT approaches. Their performance, however, is material dependent. To reduce the material reliance, an appropriate parametrization of the mixing between non-local exact exchange and semi-local xc is required. Marques *et al.* suggest the density-based mixing method for hybrid functionals [1], which achieves an overall improvement of band gap estimations for their calculations with the code VASP.

In this thesis, we adapted the density-based mixing method to the all-electron code **exciting**. We showed that the density-based quantity $\bar{g}$, on which the parametrization is based, has only slightly different values for **exciting** and VASP with the characteristic that $\bar{g}$ calculated by **exciting** is larger for most materials. The optimal mixing parameters α_{opt} are also much alike since the band gap results (with PBE, PBE0 and HSE06) are very similar for the two codes. Even though $\bar{g}$ and α_{opt} show only small discrepancies between **exciting** and VASP, the regression between the two parameters is clearly different for the two code.

Based on the statement by Marques *et al.* that $\bar{g}$ can be calculated with PBE instead of the corresponding hybrid functional, we verified that $\bar{g}$ is functional independent for **exciting** as well. Moreover, our results indicate that the mixing parameter α_{mix}, obtained from the density-based mixing method, should be applied in combination with SOC. However, to confirm our findings, more materials with SOC effects should be investigated.

To optimize the method for the all-electron framework of **exciting**, we suggest excluding the noble gases from the material set on which the fit is based, mostly because they show quite different characteristics in the relation between $\bar{g}$ and α_{opt} than the other materials. Moreover, we find that all fits, evaluated in this thesis, accomplish on average more accurate results when the noble gases are excluded. Other than that, we suggest using other powers for the single polynomial fit function than Marques *et al.* derived. For **exciting**, we find $n = 8$ and $n = 10$ to work best for PBE0_{mix} and $\text{HSE06}_{\text{mix}}$, respectively. With that, we achieve band gap results with an RMSE value with respect to the experimental gaps of 13% (for PBE0_{mix}) and 12% (for $\text{HSE06}_{\text{mix}}$) for the whole material set. These averaged errors between experiment and theory show that an improvement of the standard hybrid functional calculations could be accomplished. Especially the parametrization of PBE0 makes the functional more universal applicable and can cure extensive discrepancies in the band gap calculation for large and small band gap materials. However, both functionals, PBE0_{mix} and $\text{HSE06}_{\text{mix}}$, still show a material dependent performance. As the intention of the density-based mixing method is to remove the material dependency from the performance of hybrid functionals, i.e. to make them universally applicable for all band gaps sizes, this could not be accomplished entirely. Moreover, our results demonstrate that the density-based mixing method itself strongly depends on the choice of the used material set.

In addition to these outcomes that the method is highly sensible towards small changes in $\bar{g}$ and α_{opt}, and depends significantly on the material set, one must also critically question the values of n, we determined to be the best. As they are so similar for PBE0_{mix} and $\text{HSE06}_{\text{mix}}$ and the

minimal RMSE values do not build a sharp optimum, we tend to conclude that these results are pure fit optimization and do not represent the physical relation properly. Instead, we tend to believe that the relation between α and the material properties is more complex. However, the averaged improvement still seems to confirm that there is material dependency of the mixing parameter. Hence, the results of α_{mix} can be used a guideline for further calculations.

As a next step, we would need to test the method for materials not included in the material set. For that, it would be interesting to investigate other representatives of the included material classes as well as entirely different materials. Only if this leads to similarly good improvement for other band gap calculations the success of the method is confirmed. For the mixing method by Marques et al. this was done for a large material set of nearly 500 materials. An statistical analysis of the results is given in reference [33]. Their finding show that PBE0_{mix} outperforms PBE0 in means of the mean absolut error (MAE), the mean absolute error (MAE) and the mean absolute percentage error (MAPE). For HSE06, however, all three errors indicate a worse performance when the α is parametrized, which might demonstrate that the density-based mixing method is not suitable for HSE06.

To estimate the material set dependence of the fit parameters, one should repeat the formulation of the density-based mixing method for more subsets. Whereas we divided the material set based on the physical properties, one could also choose multiple random subsets for the fit and compare the results to reduce the biases included in the parameters (similar to a cross-validation scheme).

Moreover, it would be interesting to see whether a variation of $\bar{g}$ can improve the modelling or if an entirely different quantity needs to be found for a appropriate parametrization. To investigate where the systematic difference in the $\bar{g}$ for the codes comes from, a detailed study of the influence of different basis functions, i.e. a change in the species files, could be done for several materials. As mentioned in the previous chapter, an additional improvement of the comparability of theoretical and experimental band gaps could come from considering zero-point vibration, excitonic binding energies and polaronic effects.

Appendix

A. Convergence

For the most precise calculation of the density-based mixing method we have to converge its components with respect to the numerical parameters `rgkmax`, `ngridk` and `nempty` (compare chapter 3). The latter is not needed for pure PBE calculations. For the computation of the optimal mixing parameter α_{opt} (3.27), the PBE, PBE0 and HSE06 band gaps E_{gap} has to be calculated. For them, a convergence criterion of 0.02 eV is used. The density-based quantity $\bar{g}$ can directly be converged, with a criterion of $0.005\ \sqrt{a_0}$ (see chapter 3.3.3). The symmetry points for all band structure plots are found with the means of reference [34]. All calculations, performed for this thesis, are published at [2].

A.1 Numerical Parameters

The convergence with respect to `rgkmax` and `ngridk` can be done separately as both, the number of basis functions and the **k**-point grid density required for an precise calculation, have no influence on each other. The number of empty states `nempty`, however, has to be converged in consideration of the `rgkmax` value, as `nempty` needs to be smaller than the total number of basis functions and consequently needs to be larger for more basis functions considered. If more than one element is involved, the smaller R_{MT} is used to define `rgkmax`. For this thesis, we use predefined R_{MT} values in the species files optimized by S. Lubeck. To demonstrate the convergence, GaN was chosen as an example since it is a semiconductor, has a direct band gap and no large SOC correction.

A.1.1 Band Gaps

In figure A.1, the band gap of GaN calculated with PBE0 is illustrated. The material shows a smooth convergence for `rgkmax`, `ngridk` and `nempty`, i.e. in all three plots it is visible that the difference in the results get smaller for larger parameters. Once the difference to all the following results is smaller than ± 0.02 eV (blue area in figure A.1), we consider the parameters as converged. For `rgkmax`, this is the case in the middle of the test series. For `ngridk`, we havr to increase the number of considered **k**-points to $8 \times 8 \times 8$. This is higher than for most of the other materials tested in this thesis (compare table A.1, in which all converged results and their numerical parameters are given). For `nempty`, to consider 100 empty states from a total of 230 states computed with the Hamiltonian is enough. In figure A.1, these converged results are highlighted with larger crosses. The convergence plots look similar for the other functionals, PBE and HSE06 (with the exception that the PBE band gap has no `nempty` dependence).

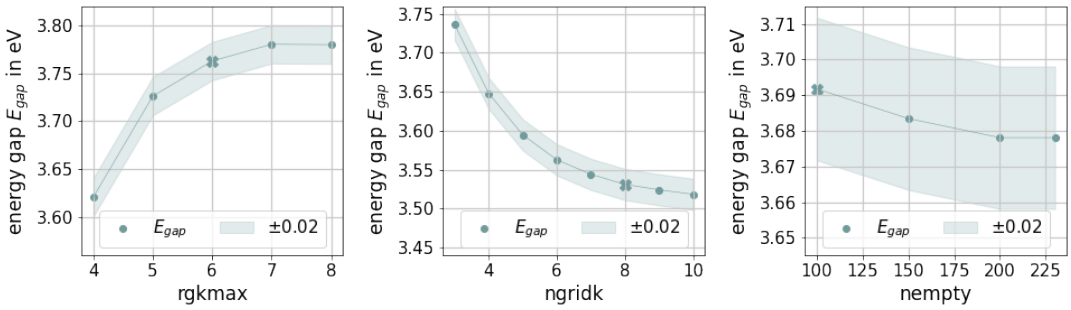

(a) `rgkmax` convergence with `ngridk` = 3 and variable `nempty`

(b) `ngridk` convergence with `rgkmax` = 5 and `nempty` = 100

(c) `nempty` convergence with `rgkmax` = 6 and `ngridk` = 4

Figure A.1: Band gap of GaN calculated with PBE0. The values are shown with respect to (a) `rgkmax`, (b) `ngridk` and (c) `nempty`. The blue area represents the convergence criterion of ± 0.02 eV and the crosses symbolize where the energy gap converged.

A.1.2 Density-Based Quantity $\bar{g}$

For the convergence of $\bar{g}$, we will analyse the results calculated with PBE since we showed in chapter 4.2.1, that $\bar{g}$ does not need to be calculated with the hybrid functional. Hence, only `rgkmax` and `ngridk` need to be included. In figure A.2, we see again a clear convergence with respect to `ngridk` with low number of **k**-points as a result. Contrarily, with respect to `rgkmax`, first an oscillation is visible. Therefore, we choose `rgkmax` = 6 as converged parameter instead of 4, which would lead to the same value.

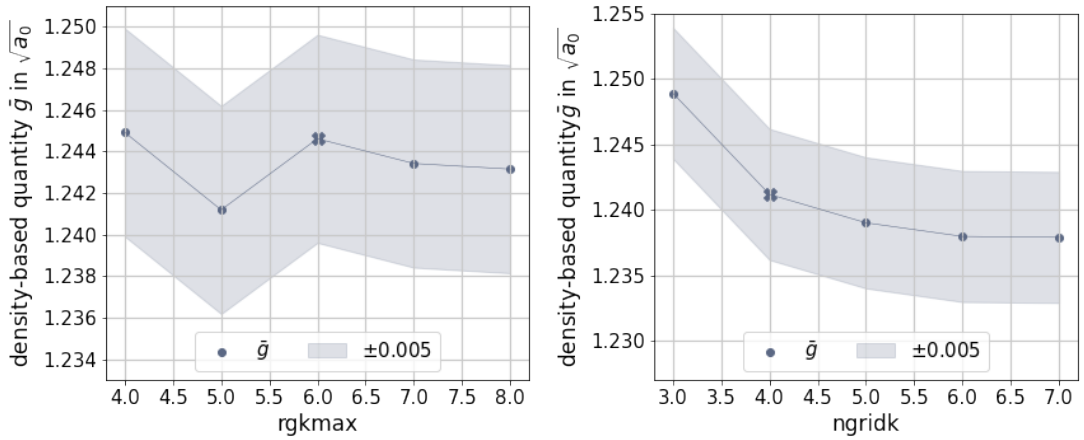

(a) `rgkmax` convergence with `ngridk` = 4

(b) `ngridk` convergence with `rgkmax` = 5

Figure A.2: Density-based quantity $\bar{g}$ for GaN calculated with PBE. The values are shown with respect to (a) `rgkmax` and (b) `ngridk`. The green area represents the convergence criterion of $\pm 0.005\ \sqrt{a_0}$ and the crosses symbolize where $\bar{g}$ converged.

To decide which convergence criterion to use for $\bar{g}$, we investigate which influence the variation of $\bar{g}$ has on α_{mix}. Therefore, in the beginning of the studies, we used equation (2.31) and our $\bar{g}$ results to compute α_{mix}. We can show here that the same conclusions can be found when our fits (4.2 and 4.3) are used for the calculation of α_{mix}. In figure A.3, the differences between α_{PBE0} (rose) and α_{HSE06} (yellow) and the converged α_{mix} are shown for each numerical parameter. One can see that the shapes of the curves are all very similar to the ones of $\bar{g}$. Moreover, all of the differences are very similar despite the fact that the fit functions are significantly different.

While after the convergence $\bar{g}$ differs in a range of $0.0015\ \sqrt{a_0}$ with respect to `rgkmax` and in a range of $0.003\ \sqrt{a_0}$ with respect to `ngridk`, all α_{mix} variate in a range of ≈ 0.0016 with respect to `rgkmax` and ≈ 0.004 with respect to `ngridk`. So they have a similar magnitude and for α_{mix} this difference is as small as we want it to be.

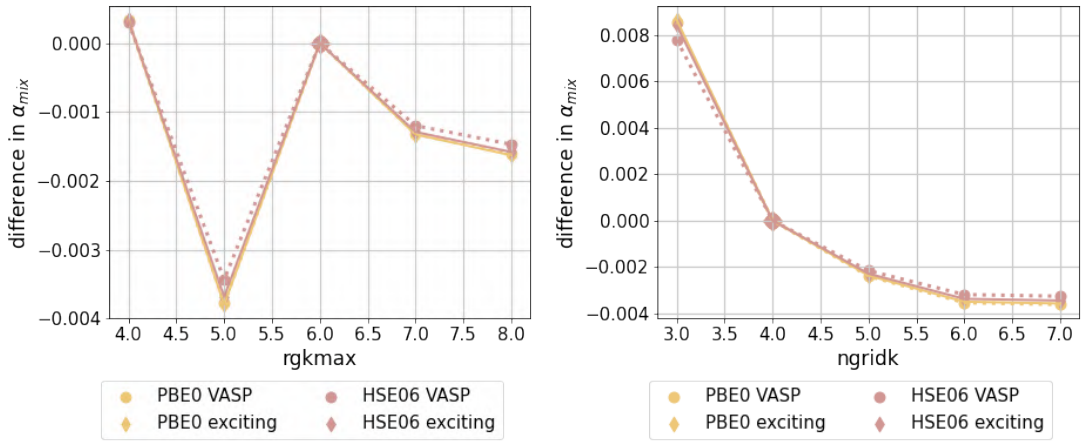

(a) `rgkmax` convergence with `ngridk` $= 4$ **(b)** `ngridk` convergence with `rgkmax` $= 5$

Figure A.3: α_{mix} calculated with the VASP fit (2.31) and the best **`exciting`** fit (4.3 and 4.2) using the convergence of $\bar{g}$ with respect to `rgkmax` and `ngridk`.

A.2 Indirect Band Gaps

The indirect gap of MoS_2 has to be computed with the Wannier interpolation scheme. The first step is to converge an energy difference at a symmetry point that is included in the **k**-point grid (e.g. the $\Gamma - \Gamma$ transition) with respect to `rgkmax`, `ngridk` and `nempty`. For MoS_2, `rgkmax` $= 5$ and `ngridk` $= 4 \times 4 \times 4$ are suitable. These parameters are used a as starting point for the Wannier function optimization. Moreover, $\bar{g}$ is extracted from them as the quantity is not influenced by the Wannier interpolation.

To define the Wannier functions, the outer and inner energy window have to be converged, i.e. the windows in which the disentanglement of the conduction bands is executed (compare ch. 3.2.1). All the states included in these windows need to be taken into account in the calculation, which is why, for Wannier interpolation, empty states need to be considered. Moreover, for most of the materials, it is necessary to increase `ngridk` to create more **k**-points that can be used for the entanglement of the bands. This is also the case for MoS_2, for which `ngridk` needs to be increased to $= 6 \times 6 \times 6$ for precise results of the Wannier functions.

In figure A.4, we show the band structure of MoS_2 created with the standard interpolation scheme (blue) and the Wannier interpolation (red) calculated for the PBE functional. The standard interpolation scheme, which is based on the KS orbitals, works perfectly well for PBE bands but does not have the option of finding the indirect gap. To define if the Wannier functions were well constructed, we use this comparison between the standard interpolation scheme and the Wannier scheme. If the highest valence band and the lowest conduction band are coinciding, we are proceeding to the energy gap calculation[xvi].

Figure A.4a shows the starting point, i.e. the numerical parameters found with the initial

[xvi] In **`exciting`**, this visual evaluation is just possible for PBE as the hybrid functionals have no standard interpolation scheme that is not based on Wannier functions. However, since the parameters for PBE, PBE0 and HSE06 are rather similar, the PBE comparison was also helpful for the hybrid functionals. Moreover, the convergence of the Wannier spread minimization is a good indicator of how well defined the Wannier functions are.

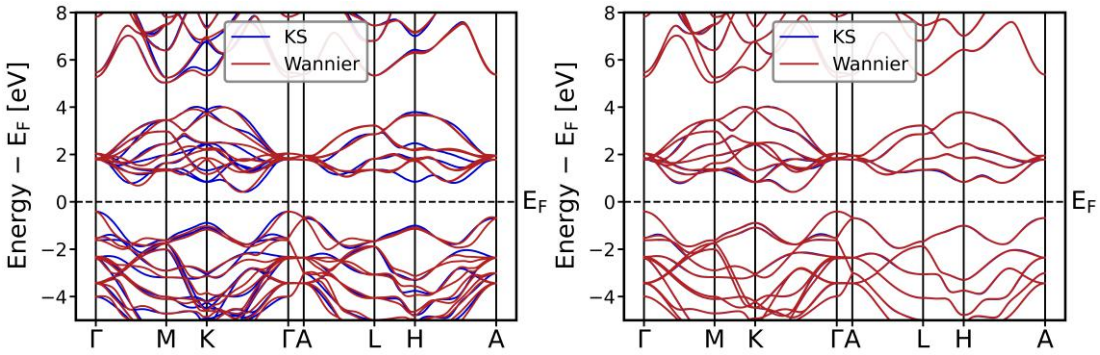

(a) Initial choice of parameters: `rgkmax` $= 5$, `ngridk` $= 4 \times 4 \times 4$ and `nempty` $= 100$ as well as energy windows $0 - 1$ Ha (inner) and $0 - 1.5$ Ha (outer).

(b) Converged choice of parameters: increased number of points for the entanglement `ngridk` $= 6 \times 6 \times 6$ and more empty states `nempty` $= 300$ as well as larger inner $(0 - 2$ Ha) and outer $(0 - 3$ Ha) energy windows.

Figure A.4: Band structure of MoS_2 for different parameters, `ngridk` and `nempty`, as well as different energy windows. The definition of the isolated valence bands is the same for both (highest 18 out of 42 bands). The Wannier functions are compared to Kohn-Sham orbitals. Both are calculated with PBE.

convergence of the $\Gamma - \Gamma$ transition. Due to an increase of `ngridk` and `nempty` as well as the doubling of the inner and outer energy windows, this could be improved. The final choice of the Wannier parameters is shown in figure A.4b, which displays a good agreement of both schemes. The band gap of MoS_2 is then eventually found on a $12 \times 12 \times 3$ interpolation grid.

A.3 Spin-Orbit Coupling

For Xe, SOC has a significant effect on the energy gap. In figure A.5, the band structures without and with the SOC corrections are shown. There, we can see how the band gap gets smaller when including SOC. Also the splitting of some bands is visible: at Γ, the calculation without SOC reveals a triple degenerate state that splits into a double and a non-degenerate state once SOC is included.

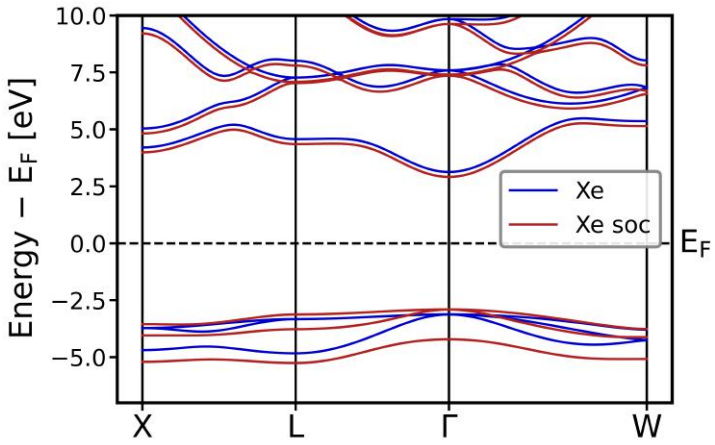

Figure A.5: Band structure for Xe with and without SOC.

In figure A.6, we can also see how the smaller band gaps obtained with SOC lead to larger α_{opt}. The band gaps are decreased by a nearly constant amount for all three functionals, and therefore, the lines of PBE0 and HSE06 are uplifted nearly in parallel .

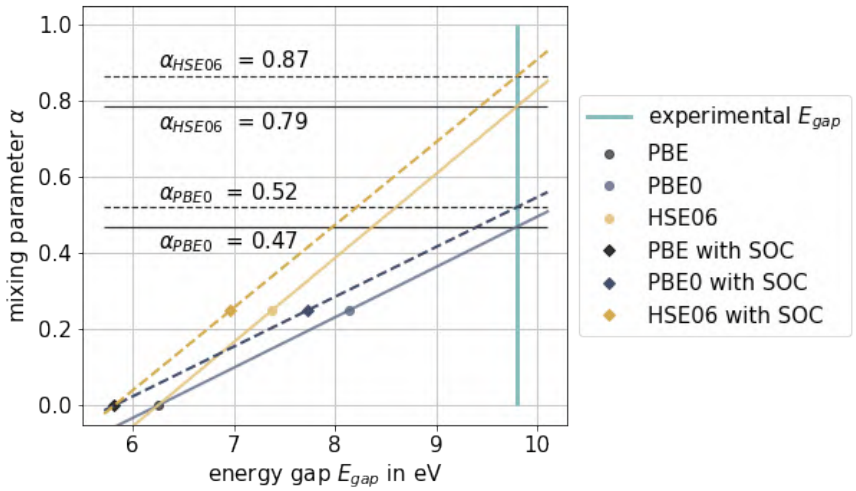

Figure A.6: Influence of SOC on the results of the optimal mixing parameter. The band gaps without SOC (filled circles and straight lines) and with SOC (rhombi and dashed lines) are shown as well as the resulting optimal mixing parameters.

A.4 Final Parameters for all Materials

For the materials that were explicitly calculated for this thesis, the converged results and their respective parameters `rgkmax`, `ngridk` and `nempty` are shown in table A.1. For pure PBE results, the number of empty states has no influence and therefore, in the the first column this number is often missing.

Table A.1: Converged band gaps E_{gap} and density-based quantities $\bar{g}$ as well as their respective numerical parameters (in grey): `rgkmax`, `ngridk`, `nempty`. All listed results are published in ref. [2].

element	exp. gap in eV	PBE		PBE0		HSE06	
		E_{gap} in eV	$\bar{g}$ in $\sqrt{a_0}$	E_{gap} in eV	$\bar{g}$ in $\sqrt{a_0}$	E_{gap} in eV	$\bar{g}$ in $\sqrt{a_0}$
Ne	21.7	11.60	1.474	15.14	1.497	14.34	1.499
		6.5 3 -	7 3 -	8 4 200	7 3 200	7.5 5 200	7 3 200
Kr	11.6	7.29	1.268	9.49	1.274	8.70	1.284
		5 3 -	8 4 -	6 3 100	6.5 3 100	7 4 100	7 3 150
Kr SOC	11.6	7.07	1.271	9.27	1.276	8.48	1.281
		5 3 100	7 3 100	6 3 100	7 3 100	7 4 100	7 4 100
Xe	9.80	6.25	1.214	8.14	1.219	7.38	1.220
		7 3 -	6 3 -	7 4 150	6 3 200	7 3 100	6 3 200
Xe SOC	9.80	5.82	1.212	7.73	1.218	6.97	1.219
		7 3 100	6 3 100	7 4 100	6 3 200	7 3 100	6 3 200
CdS	2.42	1.14	1.210	2.84	1.211	2.19	1.213
		6 4 -	5 4 -	6 7 300	5 4 100	6 3 300	5 4 100
CdS SOC	2.42	1.12	1.210	2.82	1.211	2.18	1.213
		6 4 100	5 4 100	6 7 300	5 4 100	6 3 300	5 4 100
GaN	3.20	1.63	1.245	3.58	1.244	2.92	1.244
		6 4 -	6 4 -	6 8 100	6 4 100	7 3 100	5 4 50
GaN SOC	3.20	1.63	1.241	— [a]	—	—	—
		6 4 100	5 4 100	- - -	- - -	- - -	- - -
ZnS	3.91	2.08	1.200	4.01	1.203	3.32	1.204
		6 4 -	5 4 -	6 6 250	5 4 100	6 4 300	5 4 100
ZnS SOC	3.91	2.07	1.199	— [a]	—	—	—
		8 4 100	8 4 100	- - -	- - -	- - -	- - -
LiCl	9.40	6.40	1.199	8.55	1.205	7.80	1.206
		6 3 -	6 4 -	6 4 100	6 4 100	6 4 100	6 4 100
AlN	6.28	4.14	1.183	6.25	1.191	5.49	1.192
		6 3 -	6 3 -	6 3 100	6 3 100	6 4 100	6 3 100
SiC	2.40	1.35	1.117	2.98	1.123	2.22	1.123
		6 6 140	5 5 20	6 6 50	5 4 50	6 6 100	5 4 50
Ge	0.74	0.00	1.147	1.45	1.141	0.79	1.141
		- - - [b]	6 5 100	6 6 100	6 5 100	6 5 100	6 5 100
MoS_2	1.29	0.83	1.133	2.03	1.133	1.33	1.133
		5 6 300	4 3 100	4 7 200	4 3 200	4 6 400	4 3 200
MoS_2 SOC	1.29	0.83 [c]	—	—	—	—	—
		5 6 300	- - -	- - -	- - -	- - -	- - -
SiO_2	10.30	5.81	1.315	8.41	1.324	7.64	1.325
		6 3 200	6 3 200	6 3 500	6 3 200	6 3 500	6 3 200
BN	6.25	4.47	1.211	6.59	1.213	5.79	1.211
		7 6 50	6 4 50	6 6 100	6 4 50	6 6 50	6 4 50
AlP	2.45	1.58	1.080	2.96	1.083	2.26	1.081
		6 6 150	5 4 75	6 6 100	5 4 50	6 6 100	5 4 75

[a] As GaN and ZnS did not show a correction due to SOC for PBE, we did not continue the calculations for hybrid functionals. Kr, Xe and GaN show that the SOC correction is approximately the same for all three functionals.

[b] PBE finds Ge to be a metal. Therefore, there was no band gap to converge.

[c] In **`exciting`**, Wannier interpolation can not be applied when SOC is included. So for the SOC correction we had to extract the indirect band gap roughly from the band structure by hand. With that, we found that SOC does not have an effect on the indirect band gap. However, it is likely that this is caused by the extracting method we used, since, for instance, in reference [35] a SOC correction of 16 meV was measured. Nevertheless, in chapter 4.2.2, we could show that the SOC correction of a few materials has not a significant effect on the fit function itself, therefore this error is tolerable.

A.5 Species Files

For a detailed study of basis influence, we calculate the energy gap as well as the density-based quantity $\bar{g}$ of Ne with two different species files. The first one is the default definition of the basis set included in **exciting**.

Default species file in exciting for Ne

```
1  <?xml version="1.0" encoding="UTF-8"?>
2  <spdb xsi:noNamespaceSchemaLocation="../../xml/species.xsd" xmlns:xsi="http://www.w3.
       org/2001/XMLSchema-instance">
3    <sp chemicalSymbol="Ne" name="neon" z="-10.0000" mass="36785.34276">
4      <muffinTin rmin="0.100000E-04" radius="1.2000" rinf="14.5741" radialmeshPoints="
       250"/>
5      <atomicState n="1" l="0" kappa="1" occ="2.00000" core="true"/>
6      <atomicState n="2" l="0" kappa="1" occ="2.00000" core="false"/>
7      <atomicState n="2" l="1" kappa="1" occ="2.00000" core="false"/>
8      <atomicState n="2" l="1" kappa="2" occ="4.00000" core="false"/>
9      <basis>
10       <default type="lapw" trialEnergy="0.1500" searchE="false"/>
11       <custom l="0" type="apw+lo" trialEnergy="0.1500" searchE="true"/>
12       <custom l="1" type="apw+lo" trialEnergy="0.1500" searchE="true"/>
13       <lo l="0">
14         <wf matchingOrder="0" trialEnergy="0.1500" searchE="true"/>
15         <wf matchingOrder="1" trialEnergy="0.1500" searchE="true"/>
16         <wf matchingOrder="0" trialEnergy="-1.3272" searchE="true"/>
17       </lo>
18     </basis>
19   </sp>
20 </spdb>
```

In the file, first of all, the chemical element, its nuclear charge Z and the atomic mass (line 3) are specified. Moreover, the muffin-tin radius (radius in line 4) and the radial computation resolution (radialmeshPoints) are given. We can see which quantum mechanical states are included in the calculations (lines 5 to 8), and in line 10, it is defined that LAPW is used as the standard basis function. Furthermore, for $l = 0$, local orbitals are additionally included (lines 11 to 17).

The extended species file for Ne (given below), which was provided by S. Lubeck, includes the same initial definitions. Additionally, further local orbitals are defined. Here, lo's with l's from $l = 0$ to $l = 3$ were specified. Moreover, the automatic adaption of the energy parameter ε_{la} in every SCF step (compare ch. 3.1.1 and 3.1.2) were disabled (searchE="false") for all of the lo's. This could be done as the customized values (trialEnergy) were individually converged per hand by Lubeck.

Extended species file for Ne

```
1  <?xml version="1.0" encoding="UTF-8"?>
2  <spdb xsi:noNamespaceSchemaLocation="../../xml/species.xsd" xmlns:xsi="http://www.w3.
       org/2001/XMLSchema-instance">
3    <sp chemicalSymbol="Ne" name="neon" z="-10.0000" mass="36785.34276">
4      <muffinTin rmin="0.100000E-05" radius="1.2000" rinf="14.5741" radialmeshPoints="
       600"/>
5      <atomicState n="1" l="0" kappa="1" occ="2.00000" core="true"/>
6      <atomicState n="2" l="0" kappa="1" occ="2.00000" core="false"/>
7      <atomicState n="2" l="1" kappa="1" occ="2.00000" core="false"/>
8      <atomicState n="2" l="1" kappa="2" occ="4.00000" core="false"/>
9      <basis>
10       <default type="lapw" trialEnergy="0.1500" searchE="false"/>
11       <custom l="0" type="apw+lo" trialEnergy="-1.25" searchE="false"/>
12       <lo l="0">
13         <wf matchingOrder="0" trialEnergy="-1.25" searchE="false"/>
14         <wf matchingOrder="2" trialEnergy="-1.25" searchE="false"/>
15       </lo>
```

```
16        <lo l="0">
17          <wf matchingOrder="0" trialEnergy="-1.25" searchE="false"/>
18          <wf matchingOrder="3" trialEnergy="-1.25" searchE="false"/>
19        </lo>
20        <custom l="1" type="apw+lo" trialEnergy="-0.40" searchE="false"/>
21        <lo l="1">
22          <wf matchingOrder="0" trialEnergy="-0.40" searchE="false"/>
23          <wf matchingOrder="2" trialEnergy="-0.40" searchE="false"/>
24        </lo>
25        <lo l="1">
26          <wf matchingOrder="0" trialEnergy="-0.40" searchE="false"/>
27          <wf matchingOrder="3" trialEnergy="-0.40" searchE="false"/>
28        </lo>
29        <custom l="2" type="apw+lo" trialEnergy="0.15" searchE="false"/>
30        <lo l="2">
31          <wf matchingOrder="0" trialEnergy="0.15" searchE="false"/>
32          <wf matchingOrder="2" trialEnergy="0.15" searchE="false"/>
33        </lo>
34        <custom l="3" type="apw+lo" trialEnergy="0.15" searchE="false"/>
35        <lo l="3">
36          <wf matchingOrder="0" trialEnergy="0.15" searchE="false"/>
37          <wf matchingOrder="2" trialEnergy="0.15" searchE="false"/>
38        </lo>
39      </basis>
40    </sp>
41  </spdb>
```

This leads to a more stable and reliable convergence of the SCF (for the default species, the calculations with small `rgkmax` values did not converge). Moreover, for the energy gap (in fig. A.7), we indeed see a difference in the results that is larger than the convergence criterion of 0.02 eV. Interestingly the difference is constant for all values of `rgkmax` and `ngridk`, therefore, convergence is reached at the same numerical parameters. By having a look at the total energy, we could identify that the extended species file leads to more precise results (the smallest ground state total energy is the most accurate). For the density-based quantity $\bar{g}$ (in fig. A.8), however, the difference is negligible as it is much smaller than the convergence criterion. This is in contrast to the intuition that a different basis should have a direct influence on the electron density, and hence, directly influence $\bar{g}$ as well.

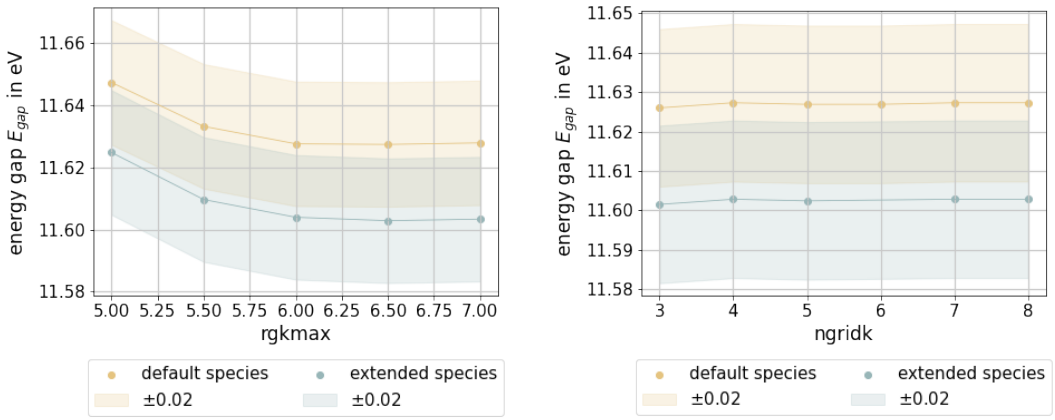

(a) `rgkmax` convergence with `ngridk` $= 4$ **(b)** `ngridk` convergence with `rgkmax` $= 6.5$

Figure A.7: Comparison of E_{gap} for the standard species files and an extended version. Convergence with respect to `rgkmax` and `ngridk`.

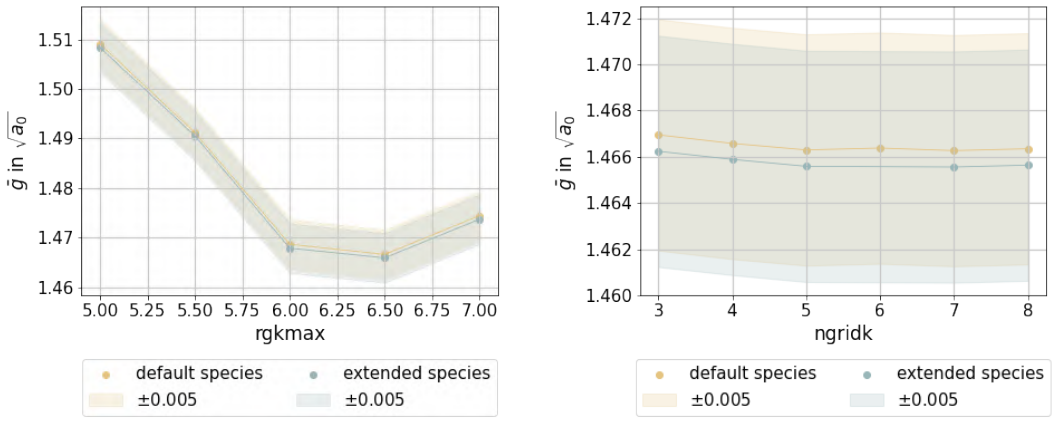

(a) `rgkmax` convergence with `ngridk` $= 4$ **(b)** `ngridk` convergence with `rgkmax` $= 6.5$

Figure A.8: Comparison of $\bar{g}$ for the standard species files and an extended version. Convergence with respect to `rgkmax` and `ngridk`.

B. Detailed Material Analysis

B.1 Material Classification

The materials can be classified according to their physical properties. If the optimal mixing parameters α_{opt} are illustrated in relation to $\bar{g}$, like in figure B.1, one can identify that the classes are located in certain region.

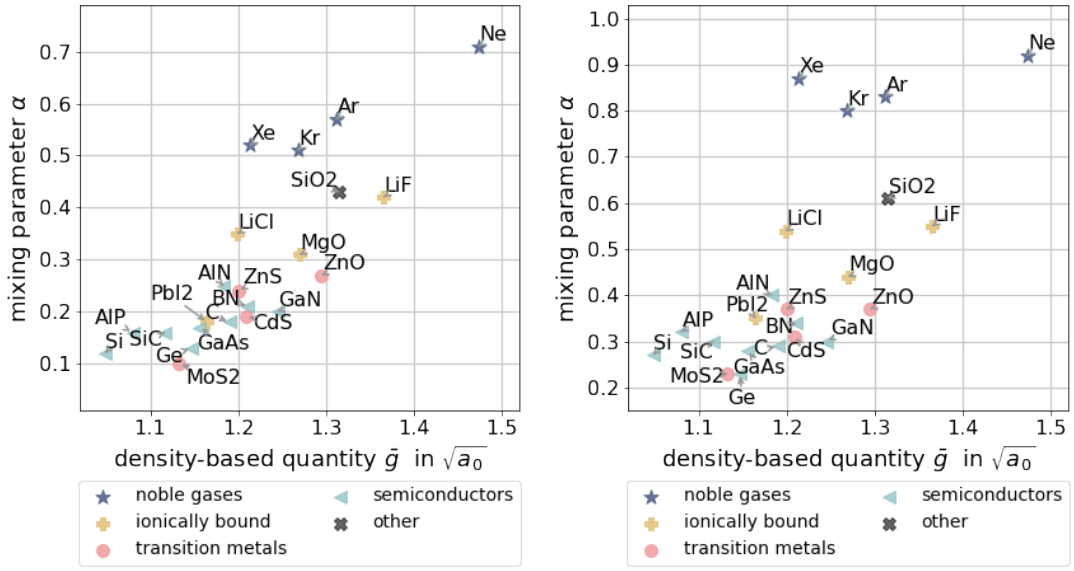

(a) Optimal mixing parameter for PBE0.

(b) Optimal mixing parameter for HSE06.

Figure B.1: Division of the samples into different material sets.muss eigentlich alpha opt sein

B.2 Reference Details

Table 3.1 lists the crystal lattices, experimental gap values and their types, the PTE main group, the numbers of valence electrons, and the classifications of all materials. Here, in table B.1, the respective references are collected. All the experimental gaps are taken from reference [1], where it was not further stated which experiments where associated with them. The master thesis by Aull, however, lists the references for the experimental band gaps explicitly [4, table 5.7].

Table B.1: Classification of the material set by means of their crystal structure, band gap, electronic and physical properties. The crystal structure is taken from the structure files provided by Marques *et al.* (if not stated otherwise) and its classification (in terms of the Strukturbericht designation) is identified with the help of reference [36]. In table 3.1, the common names (like fcc and diamond structure) for the structure classification are used instead. The experimental gaps are taken from reference [1] if not stated otherwise. For the identification of the gap type (D for direct an I for indirect), different references have been used, which are explicitly given. Lastly, the material class according to Koller *et al.* [3] is given. As not all materials were investigated by them, some additional references are given. The abbreviations stand for semiconductors (sc), ionically bound materials (ionic) and molecules including transition metals (TmX).

material	Strukturbericht designation	exp. gap E_{gap} in eV	gap type	PTE group	valence electrons	material class
Ne†	A1	21.70	D	VIII	8	—
Ar	A1	14.20	D	VIII	8	—
Kr†	A1	11.60	D	VIII	8	—
Xe†	A1	9.80	D	VIII	8	—
C	A4	5.48	D	IV	4	sc
Si	A4	1.17	I [37]	IV	4	sc
Ge†	A4	0.74	I [37]	IV	4	sc
LiF	B1	14.20	D [38]	I-VII	8	ionic
LiCl†	B1	9.40	D [39]	I-VII	8	ionic
MgO	B1	7.83	D [39]	II-VI	8	ionic
SiC†	B3	2.40	I [37]	IV-IV	8	sc
BN†	B3	6.25	I [39]	III-V	8	sc
GaN†	B3	3.20	D [37]	III-V	8	sc
GaAs	B3	1.52	D [37]	III-V	8	sc [40]
AlP†	B3	2.45	I [39]	III-V	8	sc
ZnS†	B3	3.91	D [37]	Tm-VI	18	TmX
CdS†	B3	2.42	D [37]	Tm-VI	18	TmX
AlN†	B4	6.28	D [37]	III-V	8	sc [41]
$SiO_2^\dagger$	C30	10.30	I [42]	IV-VI	16	—
$MoS_2^\dagger$	C7	1.29	I [43]	Tm-VI	18	TmX
ZnO	B4	3.44	D [39]	Tm-V	18	TmX
PbI_2	[44]	2.55 [45]	D [45]	IV-V	14	ionic [46]

C. Additional Computation Details and Further Results

C.1 Error Estimation

To compare every pair of values, we have a look at the absolute difference, as well as at the relative difference, which is defined as

$$(\Delta\%)Y_m \equiv \frac{Y_m - Y_{\text{ref},m}}{Y_{\text{ref},m}} \equiv y_m - 1. \tag{C.1}$$

Y hereby can be the band gap E_{gap}, the optimal mixing parameter α_{opt} or the density-based parameter $\bar{g}$. As reference values we either take the results with VASP or the experimental values. With this relative difference, it is possible to identify for which materials the quantities match the reference values better or worse.

To compare the performance of the functionals between each other, an average over the whole material set is needed. For that, we calculate the root-mean-squared-error (RMSE) of the relative difference

$$\text{RMSE }\% = \sqrt{\frac{\sum_{m=1}^{M}(y_m - 1)^2}{M}}. \tag{C.2}$$

C.2 Approximation of the Band Gap

In theory, for the evaluation of every fit, each band gap, with its separately estimated mixing parameter α_{mix}, would have had to be computed with **`exciting`**. As this would cost too much computational time, we needed an approximation of the band gap directly based on α_{mix}, which we therefore call E_{mix}. This can be done by inverting the linear dependence of the mixing parameter α and the calculated energy gaps E_{hyb} and E_{PBE}

$$E_{\text{mix}} = \frac{\alpha_{\text{mix}}}{0.25} E_{\text{hyb}} + \left(1 - \frac{\alpha_{\text{mix}}}{0.25}\right) E_{\text{PBE}} \,. \tag{3.29}$$

Using this approach also for the results of Marques *et al.*, we realized that this inversion is just to a certain amount accurate. In table C.1, the band gaps that Marques *et al.* calculated with PBE0_{mix} and $\text{HSE06}_{\text{mix}}$ are listed. In comparison, the E_{mix} is given, which we estimate with their mixing method, α_{mix} (2.31), and the $\bar{g}$, they provided us. We can see that for some materials, indeed the same energy is found but for some others, the discrepancy is rather large. Especially

Ne and Ge do not agree well. For Ge, the gap is so small that PBE finds no gap, which causes discrepancies to the linear relation between the mixing parameter and the band gap results. Ne has the largest band gap, which requires a mixing parameter of 0.7, which appears to be too large. The RMSE for all materials between both ways to extract the band gap is $\approx 4\%$ for PBE0 and $\approx 2\%$ for HSE06. So the energy values, we get from equation (3.29), are less accurate than the actual calculations with the code packages. Nevertheless, the similarity between the results is good enough to use this in order to compare different fits with each other. Moreover, we expect the same factors to influence the optimal mixing parameter and a cancellation of the error to some extent.

Table C.1: Comparison of the energies extracted directly from the linear dependence between E_{gap} and α and the results that were actually achieved by the mixing method with VASP (from [1]).

element	exp.	E_{gap} in eV (PBE0$_{\text{mix}}$)		E_{gap} in eV (HSE06$_{\text{mix}}$)	
	E_{gap} in eV	VASP	E_{mix}	VASP	E_{mix}
Ne	21.70	21.88	21.70	22.29	21.54
Ar	14.20	12.98	12.95	12.11	12.06
Kr	11.60	10.48	10.45	9.78	9.73
Xe	9.80	8.48	8.46	7.99	7.97
C	5.48	5.92	5.89	5.71	5.68
Si	1.17	1.07	1.05	1.21	1.16
Ge	0.74	0.68	0.59	0.82	0.80
LiF	14.20	14.99	14.87	14.28	14.14
LiCl	9.40	8.69	8.67	8.41	8.39
MgO	7.83	7.67	7.61	7.41	7.35
SiC	2.40	2.33	2.33	2.36	2.35
BN	6.25	6.60	6.58	6.29	6.27
GaN	3.20	3.52	3.49	3.39	3.35
GaAs	1.52	1.56	1.59	1.61	1.59
AlP	2.45	2.23	2.24	2.32	2.31
ZnS	3.91	4.25	4.17	3.92	3.87
CdS	2.42	3.15	3.06	2.76	2.70
AlN	6.28	6.29	6.28	6.08	6.04
SiO2	10.30	10.53	10.48	9.79	9.71
MoS2	1.29	1.63	1.64	1.50	1.49
ZnO	3.44	4.90	4.67	4.26	4.01
RMSE (theory – exp.)		14.41 %	13.82 %	10.38 %	9.41%
RMSE (E_{mix} – VASP)		3.77 %		2.02 %	

C.3 Comparison of the two Codes

For the energy gaps, the optimal mixing parameter α_{opt} and the density-based quantity $\bar{g}$, the differences between the codes **exciting** and VASP are shown. In all plots, the materials are ordered according to their band gap size (largest to smallest).

C.3.1 Band Gaps

As the energy gaps differ over a large range, figure C.1 does not show the energy gaps for all functionals but rather the difference between the calculated gap and the experimental gap.

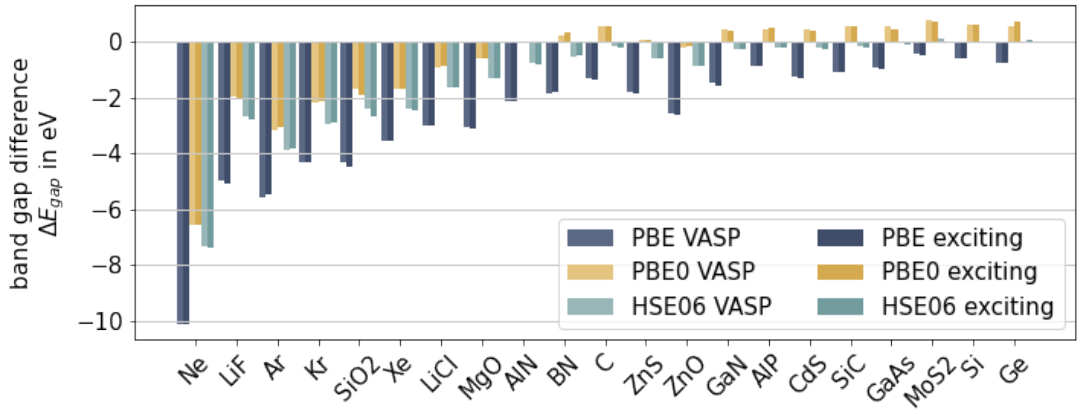

Figure C.1: Band gaps calculated with **exciting** and VASP taking the experimental values as a reference, i.e. $\Delta E = E_{\text{cal}} - E_{\text{exp}}$ in eV.

C.3.2 Optimal Mixing Parameter α_{opt}

In figure C.2, the relative differences of α_{opt} between the two codes is shown, which are overall rather small. Moreover, the distribution over the materials is not very similar to the differences figure 4.1 (energy gap differences between the codes).

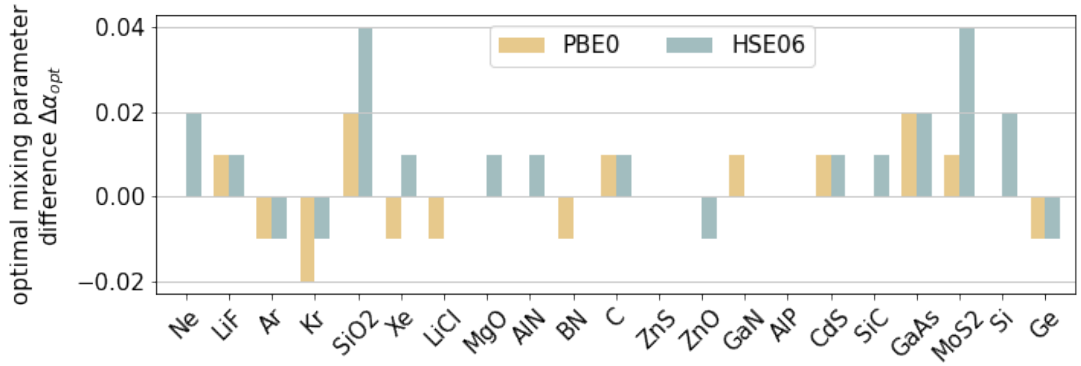

Figure C.2: Absolute differences between **exciting** and VASP in the optimal mixing parameter α_{opt}: $(\Delta\alpha_{\text{opt}}) = \alpha_{\text{exc.}} - \alpha_{\text{VASP}}$.

C.3.3 Density-Based Quantity $\bar{g}$

The differences between the codes are shown explicitly in figure C.3. Here it becomes very obvious that the difference is systematical and $\bar{g}$ is most of the times larger for **exciting**.

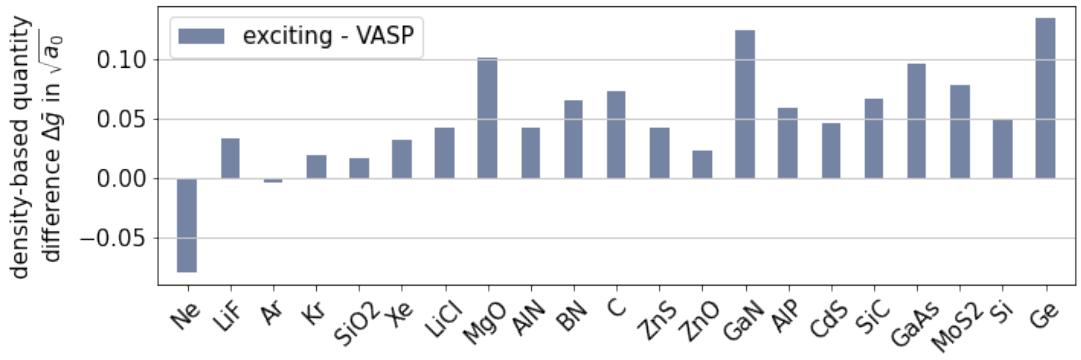

Figure C.3: Absolute differences between **exciting** and VASP in the density-based quantity $\bar{g}$: $\Delta\bar{g} = \bar{g}_{\text{exc.}} - \bar{g}_{\text{VASP}}$.

C.4 Dependence on the Exchange-Correlation Functional

Marques *et al.* state that the density-based quantity $\bar{g}$ can be computed with the semi-local functional PBE instead of the hybrid functionals [1]. For **exciting**, we tested this for the 14 materials, which were calculated in this thesis. The results are given in table C.2. We identify some differences but they, overall, are rather small.

Table C.2: Functional dependence of the density-based quantity $\bar{g}$. The results for $\bar{g}$ calculated with PBE, PBE0 and HSE06 are given in $\sqrt{a_0}$. Moreover, the difference between PBE and the hybrid functional $\Delta\bar{g} = \bar{g}_{\text{PBE}} - \bar{g}_{\text{hyb}}$ is listed.

material	PBE	PBE0		HSE06	
	$\bar{g}$ in $\sqrt{a_0}$	$\bar{g}$ in $\sqrt{a_0}$	$\Delta\bar{g}$ in $\sqrt{a_0}$	$\bar{g}$ in $\sqrt{a_0}$	$\Delta\bar{g}$ in $\sqrt{a_0}$
Ne	1.474	1.497	-0.023	1.499	-0.025
Kr	1.268	1.274	-0.006	1.284	-0.016
Xe	1.214	1.219	-0.005	1.220	-0.006
Ge	1.147	1.141	0.006	1.141	0.006
LiCl	1.199	1.205	-0.006	1.206	-0.007
SiC	1.117	1.123	-0.006	1.123	-0.006
BN	1.211	1.213	-0.002	1.211	0.000
GaN	1.245	1.244	0.001	1.244	0.001
AlP	1.080	1.083	-0.003	1.081	-0.001
ZnS	1.200	1.203	-0.003	1.204	-0.004
CdS	1.210	1.211	-0.001	1.213	-0.003
AlN	1.183	1.191	-0.008	1.192	-0.009
SiO_2	1.315	1.324	-0.009	1.325	-0.010
MoS_2	1.133	1.133	0.000	1.133	0.000
average			-0.005		-0.006

C.5 Fits for the Smallest RMSE Values

For different powers n, fits were calculated based on all materials, the subset without noble gases and semiconductors. For all of them, the RMSE values with respect to the material subset was calculated and the minimum identified. In figure C.4, the respective fits for the minimal RMSE are shown and their parameters are given.

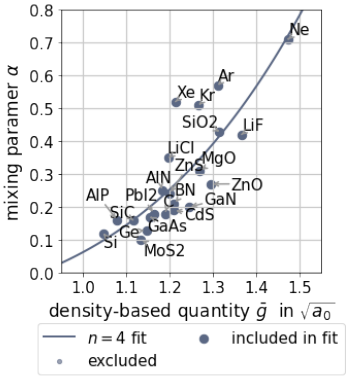

(a) Fit for PBE0, based on all materials and power $n = 4$. Fit parameters: a $= (0.18 \pm 0.03)\ a_0^{-2}$ and b $= (-0.12 \pm 0.07)$, leading to an RMSE of 17.87%.

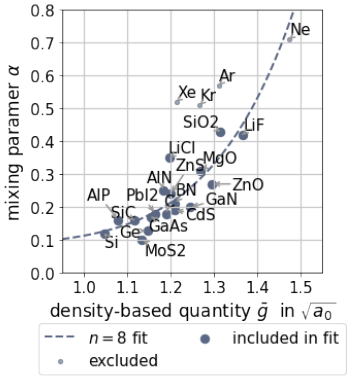

(b) Fit for PBE0, based on the subset without noble gases and $n = 8$. Fit parameters: a $= (0.030 \pm 0.005)\ a_0^{-4}$ and b $= (0.08 \pm 0.03)$, leading to an RMSE of 13.30% (12.55%).

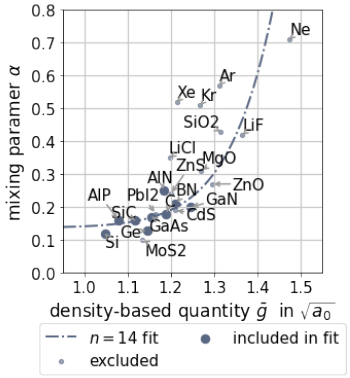

(c) Fit for PBE0, based only on semiconductors and $n = 14$. Fit parameters: a $= (0.004 \pm 0.002)\ a_0^{-7}$ and b $= (0.14 \pm 0.02)$, leading to an RMSE of 13.73% (11.29%).

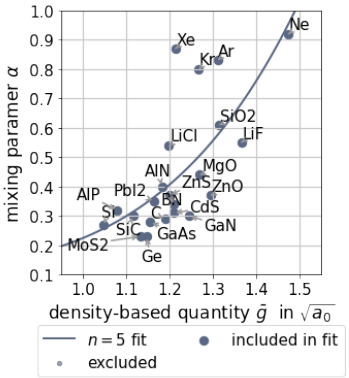

(d) Fit for HSE06, based on all materials with $n = 5$. Fit parameters: a $= (0.12 \pm 0.03)\ a_0^{-5/2}$ and b $= (0.10 \pm 0.09)$, leading to an RMSE of 16.87%.

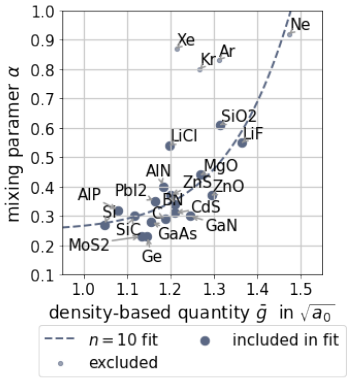

(e) Fit for HSE06, based on the material set without noble gases eith $n = 10$. Fit parameters: a $= (0.015 \pm 0.004)\ a_0^{-5}$ and b $= (0.25 \pm 0.03)$, leading to an RMSE of 12.23% (10.77%).

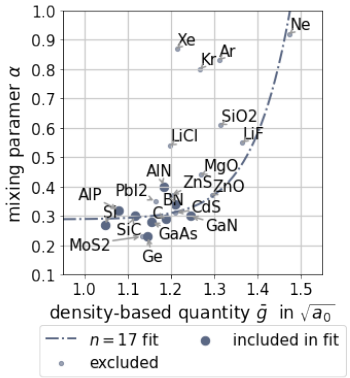

(f) Fit for HSE06, based only on semiconductors with $n = 17$. Fit parameters: a $= (0.0009 \pm 0.0014)\ a_0^{-17/2}$ and b $= (0.29 \pm 0.03)$, leading to an RMSE of 12.11% (9.95%).

Figure C.4: Density-based mixing methods for the parameters n that produce the smallest RMSE values. (a) – (c) show the results for PBE0 and (d) – (f) for HSE06. The materials included in the fits are given with large points, the rest with small dots.

C.6 Other Functions

Other functions than the single polynomial function, did not lead to a better reproduction of the experimental band gaps. In figure C.5, the RMSE values with respect to all materials are given for each function, material set and functional. None of the resulst is smaller than $\approx 13\%$ for $PBE0_{mix}$ and $\approx 12\%$ for $HSE06_{mix}$. Nevertheless, we can see that reducing the material set by excluding the noble gases leads for all of them to better results.

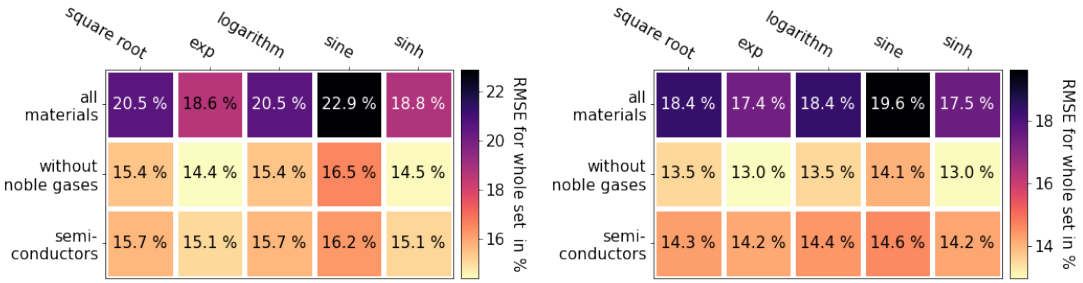

(a) $PBE0_{mix}$ **(b)** $HSE06_{mix}$

Figure C.5: RMSE values of density-based mixing method with other elemental parametrization functions in relation to the main material sets.

Bibliography

Paper

1. Marques, M. A. L., Vidal, J., Oliveira, M. J. T., Reining, L. & Botti, S. Density-Based Mixing Parameter for Hybrid Functionals. Phys. Rev. B **83,** 035119. https://doi.org/10.1103/PhysRevB.83.035119 (Jan. 2011).

3. Koller, D., Blaha, P. & Tran, F. Hybrid Functionals for Solids with an Optimized Hartree–Fock Mixing Parameter. J. Phys.: Condens. Matter **25,** 435503. https://doi.org/10.1088/0953-8984/25/43/435503 (Oct. 2013).

8. Görling, A. Density-Functional Theory for Excited States. Phys. Rev. A **54,** 3912–3915. https://doi.org/10.1103/PhysRevA.54.3912 (Nov. 1996).

9. Becke, A. D. Perspective: Fifty Years of Density-Functional Theory in Chemical Physics. J. Chem. Phys. **140,** 18A301. https://doi.org/10.1063/1.4869598 (Apr. 2014).

11. Kohn, W. & Sham, L. J. Self-Consistent Equations Including Exchange and Correlation Effects. Phys. Rev. **140,** A1133–A1138. https://doi.org/10.1103/PhysRev.140.A1133 (Nov. 1965).

12. Hohenberg, P. & Kohn, W. Inhomogeneous Electron Gas. Phys. Rev. **136,** B864–B871. https://doi.org/10.1103/PhysRev.136.B864 (Nov. 1964).

13. Mermin, N. D. Thermal Properties of the Inhomogeneous Electron Gas. Phys. Rev. **137,** A1441–A1443. https://doi.org/10.1103/PhysRev.137.A1441 (Mar. 1965).

14. Runge, E. & Gross, E. K. U. Density-Functional Theory for Time-Dependent Systems. Phys. Rev. Lett. **52,** 997–1000. https://doi.org/10.1103/PhysRevLett.52.997 (Mar. 1984).

15. Betzinger, M., Friedrich, C. & Blügel, S. Hybrid Functionals Within the All-Electron FLAPW Method: Implementation and Applications of PBE0. Phys. Rev. B **81,** 195117. https://doi.org/10.1103/PhysRevB.81.195117 (May 2010).

16. Perdew, J. P. & Schmidt, K. Jacob's Ladder of Density Functional Approximations for the Exchange-Correlation Energy. AIP Conf. Proc. **577,** 1–20. https://doi.org/10.1063/1.1390175 (Aug. 2001).

17. Becke, A. D. Density-Functional Exchange-Energy Approximation with Correct Asymptotic Behavior. Phys. Rev. A **38,** 3098–3100. https://doi.org/10.1103/PhysRevA.38.3098 (Sept. 1988).

18. Perdew, J. P. & Wang, Y. Accurate and Simple Analytic Representation of the Electron-Gas Correlation Energy. Phys. Rev. B **45,** 13244–13249. https://doi.org/10.1103/PhysRevB.45.13244 (June 1992).

19. Perdew, J. P., Burke, K. & Ernzerhof, M. Generalized Gradient Approximation Made Simple. Phys. Rev. Lett. **77,** 3865–3868. https://doi.org/10.1103/PhysRevLett.77.3865 (Oct. 1996).

20. Tao, J., Perdew, J. P., Staroverov, V. N. & Scuseria, G. E. Climbing the Density Functional Ladder: Nonempirical Meta–Generalized Gradient Approximation Designed for Molecules and Solids. Phys. Rev. Lett. **91,** 146401. https://doi.org/10.1103/PhysRevLett.91.146401 (Sept. 2003).

21. Perdew, J. P., Ernzerhof, M. & Burke, K. Rationale for Mixing Exact Exchange with Density Functional Approximations. J. Chem. Phys. **105,** 9982–9985. https://doi.org/10.1063/1.472933 (Dec. 1996).

22. Adamo, C. & Barone, V. Toward Reliable Density Functional Methods Without Adjustable Parameters: The PBE0 Model. J. Chem. Phys. **110,** 6158–6170. https://doi.org/10.1063/1.478522 (Mar. 1999).

23. Heyd, J., Scuseria, G. E. & Ernzerhof, M. Hybrid Functionals Based on a Screened Coulomb Potential. J. Chem. Phys. **118,** 8207–8215. https://doi.org/10.1063/1.1564060 (Apr. 2003).

24. Heyd, J., Scuseria, G. E. & Ernzerhof, M. Erratum: Hybrid Functionals Based on a Screened Coulomb Potential [J. Chem. Phys. 118, 8207 (2003)]. J. Chem. Phys. **124,** 219906. https://doi.org/10.1063/1.2204597 (June 2006).

25. Borlido, P., Marques, M. A. L. & Botti, S. Local Hybrid Density Functional for Interfaces. J. Chem. Theory Comput. **14,** 939–947. https://doi.org/10.1021/acs.jctc.7b00853 (Dec. 2018).

27. Gulans, A. et al. **exciting**: A Full-Potential All-Electron Package Implementing Density-Functional Theory and Many-Body Perturbation Theory. J. Phys.: Condens. Matter **26,** 363202. https://doi.org/10.1088/0953-8984/26/36/363202 (Aug. 2014).

28. Tillack, S., Gulans, A. & Draxl, C. Maximally Localized Wannier Functions within the (L)APW + LO Method. Phys. Rev. B **101,** 235102. https://doi.org/10.1103/PhysRevB.101.235102 (June 2020).

31. Lejaeghere, K. et al. Reproducibility in Density Functional Theory Calculations of Solids. Science **351.** https://doi.org/10.1126/science.aad3000 (Mar. 2016).

32. Rodrigues Pela, R., Werner, U., Nabok, D. & Draxl, C. Probing the LDA-1/2 Method as a Starting Point for G_0W_0 Calculations. Phys. Rev. B **94,** 235141. https://doi.org/10.1103/PhysRevB.94.235141 (Dec. 2016).

33. Borlido, P. et al. Exchange-correlation functionals for band gaps of solids: benchmark, reparametrization and machine learning. npj Comp. Mat. **6.** https://doi.org/10.1038/s41524-020-00360-0 (July 2020).

35. Zhao, Y.-H., Yang, F., Wang, J., Guo, H. & Ji, W. Continuously Tunable Electronic Structure of Transition Metal Dichalcogenides Superlattices. Sci. Rep. **5,** 8356. https://doi.org/10.1038/srep08356 (Feb. 2015).

38. Sajiid, A., Murtaza, G. & Reshak, A. H. Shift of Band Gap from Direct to Indirect and Optical Response of LiF Under Pressure. Mod. Phys. Lett. B **27,** 1350061. https://doi.org/10.1142/S0217984913500619 (Mar. 2013).

39. Lee, J., Seko, A., Shitara, K., Nakayama, K. & Tanaka, I. Prediction Model of Band Gap for Inorganic Compounds by Combination of Density Functional Theory Calculations and Machine Learning Techniques. Phys. Rev. B **93,** 115104. https://doi.org/10.1103/PhysRevB.93.115104 (Mar. 2016).

42. Nekrashevich, S. S. & Gritsenko, V. A. Electronic Structure of Silicon Dioxide (a Review). Phys. Solid State **56,** 207–222. https://doi.org/10.1134/S106378341402022X (Feb. 2014).

43. Han, B. & Hu, Y. MoS_2 as a Co-Catalyst for Photocatalytic Hydrogen Production from Water. Energy Sci. Eng. **4,** 285–304. https://doi.org/10.1002/ese3.128 (Oct. 2016).

44. Palosz, B. The Structure of PbI2polytypes 2H and 4H: a Study of the 2H-4H transition. J. Phys.: Condens. Matter **2,** 5285–5295. https://doi.org/10.1088/0953-8984/2/24/001 (June 1990).

45. Gähwiller, C. & Harbeke, G. Excitonic Effects in the Electroreflectance of Lead Iodide. Phys. Rev. **185,** 1141–1149. https://doi.org/10.1103/PhysRev.185.1141 (Sept. 1969).

Textbooks and Thesis's

4. Aull, T. Hybrid Functional with Self-Consistent Density-Dependent Mixing master's thesis (Martin-Luther University of Halle-Wittenberg, Nov. 2018).

6. Martin, R. M. Electronic Structure: Basic Theory and Practical Methods 1st ed. ISBN: 978-0-51-180576-9 (Cambridge University Press, 2004).

7. Sholl, D. & Steckel, J. A. Density Functional Theory: A Practical Introduction 1st ed. ISBN: 978-0-47-037317-0 (Wiley-Interscience, Hoboken, 2009).

10. Sukumar, N. & Sukumar, S. in A Matter of Density Chapter 3 - The Electron Density, 41–66 (John Wiley Sons, Ltd, Sept. 2012). ISBN: 978-1-11-843174-0.

29. Singh, D. J. & Nordström, L. Planewaves, Pseudopotentials, and the LAPW Method 2nd ed. ISBN: 978-0-387-28780-5 (Springer, Boston, MA, Boston, 2006).

37. Ohring, M. in Materials Science of Thin Films 2nd ed. Chapter 8 - Epitaxy, 417–494 (Academic Press, San Diego, 2002). ISBN: 978-0-12-524975-1.

41. Hua, Q., Ma, B. & Hu, W. in Encyclopedia of Materials: Technical Ceramics and Glasses Aluminum, Gallium, and Indium Nitrides, 74–83 (Elsevier, Oxford, 2021). ISBN: 978-0-12-822233-1.

Webpages

2. Richter, J., Vona, C. & Draxl, C. NOMAD Dataset: BandGapBenchmark [Online; accessed 22-August-2021]. 2021. https://dx.doi.org/10.17172/NOMAD/2021.08.22-1.

5. VASP contibuters. The Vienna Ab initio Simulation Package [Online; accessed 13-July-2021]. 2021. https://www.vasp.at/.

26. **exciting** developers. The exciting Code [Online; accessed 9-June-2021]. 2021. http://exciting-code.org/.

30. The SciPy community. SciPy API [Online; accessed 25-June-2021]. 2021. https://docs.scipy.org/doc/scipy/reference/.

34. Aroyo, M. I. et al. Bilbao Crystallographic Server [Online; accessed 9-June-2021]. 2021. https://www.cryst.ehu.es/.

36. Wikipedia contributors. Strukturbericht designation — Wikipedia, The Free Encyclopedia [Online; accessed 11-July-2021]. 2021. https://en.wikipedia.org/w/index.php?title=Strukturbericht_designation&oldid=1029020893.

40. Wikipedia contributors. Gallium arsenide — Wikipedia, The Free Encyclopedia [Online; accessed 11-July-2021]. 2021. https://en.wikipedia.org/w/index.php?title=Gallium_arsenide&oldid=1030916221.

46. Wikipedia contributors. Lead(II) iodide — Wikipedia, The Free Encyclopedia [Online; accessed 11-July-2021]. 2021. https://en.wikipedia.org/w/index.php?title=Lead(II)_iodide&oldid=1024693356.

Selbstständigkeitserklärung

Ich erkläre hiermit, dass ich die vorliegende Arbeit selbstständig verfasst und noch nicht für andere Prüfungen eingereicht habe. Sämtliche Quellen einschließlich Internetquellen, die unverändert oder abgewandelt wiedergegeben werden, insbesondere Quellen für Texte, Grafiken, Tabellen und Bilder, sind als solche kenntlich gemacht. Mir ist bekannt, dass bei Verstößen gegen diese Grundsätze ein Verfahren wegen Täuschungsversuchs bzw. Täuschung eingeleitet wird.

Berlin, den September 1, 2021 .....J. Richter.....

Declaration

I hereby declare that I have written this thesis independently and have not yet submitted it for other examinations. All sources, including internet sources, which are reproduced unchanged or modified, in particular sources for texts, graphics, tables and images, are marked as such. I am aware that violations of these principles will result in proceedings for attempted cheating or deception.

Berlin, September 1, 2021 .....J. Richter.....